NASA/TP–20230012805

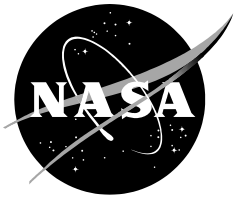

Propellant Mass Gauging in Microgravity with Electrical Capacitance Tomography

Jedediah M. Storey
Kennedy Space Center, Florida

Brandon S. Marsell
Kennedy Space Center, Florida

Michael T. Elmore
a. i. solutions, Kennedy Space Center, Florida

Scott Clark
a. i. solutions, Kennedy Space Center, Florida

September 2023

NASA STI Program Report Series

The NASA STI Program collects, organizes, provides for archiving, and disseminates NASA's STI. The NASA STI program provides access to the NTRS Registered and its public interface, the NASA Technical Reports Server, thus providing one of the largest collections of aeronautical and space science STI in the world. Results are published in both non-NASA channels and by NASA in the NASA STI Report Series, which includes the following report types:

- TECHNICAL PUBLICATION. Reports of completed research or a major significant phase of research that present the results of NASA Programs and include extensive data or theoretical analysis. Includes compilations of significant scientific and technical data and information deemed to be of continuing reference value. NASA counter-part of peer-reviewed formal professional papers but has less stringent limitations on manuscript length and extent of graphic presentations.

- TECHNICAL MEMORANDUM. Scientific and technical findings that are preliminary or of specialized interest, e.g., quick release reports, working papers, and bibliographies that contain minimal annotation. Does not contain extensive analysis.

- CONTRACTOR REPORT. Scientific and technical findings by NASA-sponsored contractors and grantees.

- CONFERENCE PUBLICATION. Collected papers from scientific and technical conferences, symposia, seminars, or other meetings sponsored or co-sponsored by NASA.

- SPECIAL PUBLICATION. Scientific, technical, or historical information from NASA programs, projects, and missions, often concerned with subjects having substantial public interest.

- TECHNICAL TRANSLATION. English-language translations of foreign scientific and technical material pertinent to NASA's mission.

Specialized services also include organizing and publishing research results, distributing specialized research announcements and feeds, providing information desk and personal search support, and enabling data exchange services.

For more information about the NASA STI program, see the following:

- Access the NASA STI program home page at http://www.sti.nasa.gov

- Help desk contact information:

https://www.sti.nasa.gov/sti-contact-form/
and select the "General" help request type.

NASA/TP–20230012805

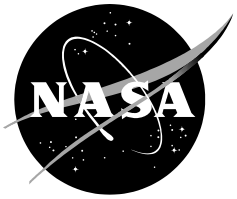

Propellant Mass Gauging in Microgravity with Electrical Capacitance Tomography

Jedediah M. Storey
Kennedy Space Center, Florida

Brandon S. Marsell
Kennedy Space Center, Florida

Michael T. Elmore
a. i. solutions, Kennedy Space Center, Florida

Scott Clark
a. i. solutions, Kennedy Space Center, Florida

National Aeronautics and
Space Administration

Kennedy Space Center, FL 32899-0001

September 2023

Abstract

Advancements in microgravity propellant mass gauging will result in improvements to many areas of propellant management, which influences space vehicle performance and mission assurance. Propellant mass gauging technologies designed to work in an accelerated environment, where the propellant remains settled at one end of the propellant tank, do not always work well in a microgravity environment because the propellant is not necessarily settled. While some microgravity mass gauging technologies exist at various stages of development, most of them have major disadvantages. Electrical Capacitance Tomography (ECT) is a sensing technology that is able to reconstruct the liquid distribution inside of a tank, which can then be integrated to obtain mass. While ECT mass gauging will theoretically work during all phases of flight, it had not yet been tested in microgravity. The NASA Kennedy Space Center Launch Services Program, with support from the Flight Opportunities Program, successfully tested an ECT liquid mass gauging system experiment on a parabolic flight aircraft in May 2022. Basics of ECT measurement theory, details of the experiment setup, data processing, ground test results, and the flight test result will be discussed. The results suggest that ECT sensor systems will be useful as a propellant mass gauging technology in both accelerated and microgravity environments.

Contents

Figures

Tables

Acronyms and Abbreviations

AC	=	Alternating Current
APL	=	Applied Physics Laboratory
CI	=	Confidence Interval
CTE	=	Coefficient of Thermal Expansion
DC	=	Direct Current
DoF	=	Degrees of Freedom
ECT	=	Electrical Capacitance Tomography
FIR	=	Finite Impulse Response
FOP	=	Flight Opportunities Program
GSE	=	Ground Support Equipment
GUI	=	Graphical User Interface
ICDF	=	Inverse Cumulative Distribution Function
IMU	=	Inertial Measurement Unit
KSC	=	Kennedy Space Center
LW	=	Landweber
LBP	=	Linear Back Projection
LH2	=	Liquid Hydrogen
LN2	=	Liquid Nitrogen
LO2	=	Liquid Oxygen
LSP	=	Launch Services Program
MA	=	Moving Average
MF	=	Mass Fraction
MPG	=	Modal Propellant Gauging
NVF	=	Notional Volume Fraction
PMD	=	Propellant Management Device
RFMG	=	Radio Frequency Mass Gauging
SNR	=	Signal to Noise Ratio
SSD	=	Solid State Drive
UI	=	Uncertainty Interval
VF	=	Volume Fraction

Symbols

A = acceleration [m/s^2]
C = capacitance [F]
CM = center of mass [m]
C^* = normalized capacitance, nondimensional
D = tank diameter [m]
e = error
g = unit grams, not to be confused with G
G = Earth gravity, acceleration [9.81 m/s^2]
m = mass
Q = charge [C]
S = sensitivity matrix [F/F/m]
V = voltage [V]
ϵ = permittivity distribution [F/m]
ϵ^* = normalized permittivity distribution, nondimensional
ε_0 = vacuum permittivity [F/m]
ε_R = relative permittivity, = $\varepsilon/\varepsilon_0$
ν = volume [m^3]
ϕ = electric field potential [V]
ω = rotation rate [rad/s]

Acknowledgments

Within LSP, the authors would like to thank the Studies Board, upper management, and Flight Analysis IT for their support. Within KSC, the authors would like to thank the UB directorate, in particular Robert Youngquist, Mark Nurge, Chris Biagi, and Austin Atkins for their invaluable guidance and support, the SI directorate, in particular Flight Operations, and Safety and Mission Assurance. The authors would like to thank the Flight Opportunities Program, in particular Earl Adams and Alexander Van Dijk, and Zero-G corporation for their guidance and support flying us and the experiment. The authors would like to acknowledge Paul Tol for his work on the colorblind-friendly color schemes that were used in the plots in this paper.

Funding for this study was provided by the NASA KSC LSP Studies Board. The NASA Flight Opportunities Program funded the parabolic flights.

I. Introduction

The ability to accurately gauge liquid propellant mass in rocket and spacecraft tanks is important for space mission planning, design, and operations. Improving the accuracy of propellant mass gauging over all phases of flight, including those generating unsettled configurations, will increase mission assurance and lower propellant mass dispersions, margins, and residuals. Enabling accurate mass gauging when the propellant is unsettled may remove the need to expend propellant for settling burns during long coasts. Improvements in microgravity mass gauging may also help with orbital debris issues, since the primary criteria for second stage deorbit burns is remaining propellant and its associated uncertainty.

Currently operational propellant mass gauging technologies have major drawbacks. Differential pressure transducers and point probes require the propellant to be settled, which requires settling burns. Tracking propellant consumption rates and integrating over time suffers from error accumulation and results in large error when the remaining propellant is low [1]. Modal Propellant Gauging (MPG) has a claimed resolution of 3-4% at fill fractions between 10 and 50% in low gravity, but the propellant must be in contact with the tank walls and settled in a calibrated configuration for MPG to be accurate [2]. Radio Frequency Mass Gauging can work with unsettled propellant and has a reported uncertainty of ±1% full scale in 1 G and ±6% full scale in low gravity [3]. RFMG accuracy is dependent on how close the simulated fluid configurations are to the actual configuration, meaning it is dependent on the size of the database of pre-computed high-fidelity simulations.

Electrical Capacitance Tomography (ECT) is a sensing technology that works by measuring the capacitance between many pairs of electrodes mounted to the wall of a vessel. If the walls of the vessel are electrically conductive, these electrodes must be mounted to the inner surface of the wall. The electrodes should cover most of the wall surface area for the ECT system to be accurate throughout the volume of the vessel. Since capacitance is related to permittivity, which in turn is approximately related to the gas and liquid densities via the Claussius-Mossotti relation [4], it is possible, via tomographic mathematical techniques, to reconstruct the density distribution of the material contained in the vessel. Volumetric integration of the density distribution yields the mass of the material in the vessel.

Historically, ECT has been used in various industries, such as the petrochemical industry, to measure two-phase flow in pipes. NASA ran a feasibility study and partially developed a whole-tank capacitive gauging system for Apollo program in the 1960's [5]. In 2007, Ref. [6] demonstrated an ECT system with a new image reconstruction algorithm for 3D high contrast dielectric distributions. NASA did some preliminary research into ECT in 2013 [7], but the work was not completed, and no publications on the results of that work exist. Ref. [8] used an ECT-instrumented cylindrical tank with kerosene to demonstrate measuring liquid mass to within 1% of full tank mass, reconstructing the liquid distribution for imaging, and tracking of liquid center of mass (CM), which enabled estimation of slosh forces. Depending on the details of the ECT system and process, multi-kHz sample rates are achievable, allowing for real-time gauging measurements. Ref. [9] discusses fabrication of flexible electrodes for ECT and presents some test data from subscale propellant tanks instrumented with these electrodes. Ref. [10] slosh-tested an ECT-instrumented carbon fiber tank with silicone oil and an engineered fluid. Some slosh tests induced wave breaking, and some tests were run with a bubbler (to modify density). The liquid fill level measurements for these tests were repeatable to within 0.1% of full tank volume, and accurate to within 1-2%, though the authors stated they believed most of that error to be systematic and correctable, and thus claimed 0.1% accuracy. ECT systems have also

been tested with cryogens. Ref. [10] mentions testing an ECT system with LN_2, though no details are provided. Ref. [11] shows successful test results from an ECT system in an LH_2 Dewar. The ECT system was used to measure LH_2 relative permittivity, and its fill level resolution was within 0.5 mm, though details of the electrode fabrication method were not published. The authors are aware of a research group at Kennedy Space Center (KSC) [12] that has successfully tested ECT systems in LN_2 tanks, and the electrodes have survived many thermal cycles. ECT technology needed to be demonstrated in microgravity to verify that it can work accurately for space-like fluid configurations. While the definition of accuracy and accuracy targets varies in the liquid mass gauging literature, the accuracy goal for this study is defined to be lower than 1% total ECT system liquid mass error.

The NASA KSC Launch Services Program (LSP), with support from the Flight Opportunities Program (FOP), successfully tested an ECT liquid mass gauging experiment on a parabolic flight aircraft in May 2022. The basics of ECT measurement theory, practical considerations for implementing an ECT system for a real tank, details of the experiment setup, electrostatic simulations, data processing, uncertainty analysis, ground test results, and results from the microgravity parabolic flights will be presented. Herein, “ECT system” refers to all hardware and software, including ECT reconstruction algorithms, required to obtain a liquid mass measurement.

II. ECT Theory

ECT systems rapidly measure capacitance between all pairs of electrodes. These capacitances are used in one of many different methods for solving the “inverse problem” to obtain a permittivity distribution in the domain (tank). The distribution is often presented as an image, so this process is often referred to as “reconstruction” [13]. In this paper, “reconstruction” refers to the permittivity (fluid) distribution calculated by an ECT algorithm. The “forward problem” uses a known permittivity distribution to solve the electrostatic partial differential equations for the capacitances, typically obtained via simulation (see Section VII).

If electrode *k* is raised to a voltage V_k with respect to electrode *j*, and all other electrodes are at the same voltage as electrode *j*, then the capacitance of the *j,k* electrode pair is calculated as the integral over the surface of electrode *j* of the permittivity distribution times the gradient of the electric potential:

$$C_{j,k} = \frac{Q_j}{V_k} = -\frac{1}{V_k} \iint_{A_j} \epsilon \nabla \phi_k \, dA \tag{1}$$

If *n* is the number of electrodes, there will be $N = \frac{n(n-1)}{2}$ unique *j,k* electrode pairs. Note in Eq. 1 that the capacitance is proportional to the permittivity on the surface of the electrode, and the potential function depends on permittivity. Discretizing and linearizing yields:

$$\Delta C = S \cdot \Delta \epsilon \tag{2}$$

The sensitivity matrix, *S*, maps changes in permittivity to changes in capacitance. Typically, the capacitances and permittivity distribution are normalized to be between 0 and 1. Normalized capacitance is calculated as:

$$C^* = \frac{C_{j,k} - C_e}{C_f - C_e} \tag{3}$$

where C_e and C_f are measured capacitances of the *j,k* electrode pair when the tank is empty and full of liquid, respectively. If *S* now maps between normalized capacitance and normalized permittivity, then the forward problem becomes:

$$C^* = S \cdot \epsilon^* \tag{4}$$

C^* is a N x 1 vector, and if ϵ^* is a M x 1 vector, then *S* is a N x M matrix. M is the number of mesh "cells", or "voxels", in the electrostatic simulation, so M>>N. Most ECT methods calculate *S* using empty tank simulations and assume *S* is constant, i.e. not affected by permittivity distribution. While this assumption is physically inaccurate and results in error, it facilitates a solution with low computational cost that does not require a priori knowledge of the permittivity distribution [14]. Each element of *S* is calculated as follows:

$$S_{l,i} = \frac{\varepsilon_0 \nu_i \nabla\phi_j \cdot \nabla\phi_k}{V_j V_k}, l = 1 \dots N, i = 1 \dots M \tag{5}$$

If Eq. 4 is the forward problem, then it follows that the inverse problem is:

$$\epsilon^* = S^{-1} \cdot C^* \tag{6}$$

Unfortunately, the inverse problem is under-determined and ill-posed [13], meaning S^{-1} does not exist. There are many methods for solving ill-posed problems like the ECT inverse problem, and Ref. [13] presents six of the simplest ones, of which Linear Back Projection (LBP) is used to produce the results shown in Section IX. LBP assumes that $S^{-1} = S^T$.

$$\epsilon^* = S^T \cdot C^* \tag{7}$$

S^T can be thought of as a linear mapping from the capacitance vector space to the permittivity vector space. Despite this assumption not having a strict mathematical basis, LBP can provide useful results. It is the simplest ECT method and fast enough to be run in real-time. However, LBP permittivity distributions tend to be smeared and cannot capture sharp phase interfaces without thresholding. For the case of two immiscible phases, such as a tank partially filled with an incompressible liquid, the normalized permittivities can be assumed to be volume fractions in each cell (or voxel), which are integrated to obtain a total liquid volume. The total liquid volume is then multiplied by a single liquid density to get liquid mass. In addition to volume and mass, center of mass can be calculated from reconstruction results.

Linearization (Eq. 2), the linear assumption between fill level and capacitance inherent in the capacitance normalization (Eq. 3), assuming *S* is constant and not dependent on permittivity distribution (Eq. 5), and the linear mapping of LBP (Eq. 7), all introduce errors that manifest as nonlinearities in the gauging results. Section VIII.B discusses partial corrections, but these nonlinearities are not always correctable.

Landweber (LW) is a variation of the steepest gradient descent method that attempts to minimize the capacitance residuals via iteration. A variation of this method, "projected Landweber", constrains the normalized permittivity solution to be between 0 and 1 by making all values greater than 1 be 1 and all values less than 0 be 0. Eq. 8 is the projected LW iterative algorithm.

$$\epsilon^*_{k+1} = P[\,\epsilon^*_k - \alpha S^T(S\,\epsilon^*_k - C^*)]\,,$$
$$P[f(x)] = \begin{cases} 0 & \text{if } f(x) < 0 \\ f(x) & \text{if } 0 \le f(x) \le 1 \\ 1 & \text{if } f(x) > 1 \end{cases} \quad (8)$$

where α is a positive scalar that sets the *k*th step size. The derivation of Eq. 8 is available in Ref. [13]. The initial condition for ϵ^*, the number of iterations, and α must be decided, and they influence how fast LW converges and the final result. LW reconstructions tend to have a sharper interface between fluid phases than LBP. Like LBP, LW is simple enough to be run in real-time, though it is slower than LBP, and speed is heavily dependent on the number of mesh cells, or voxels, in the discretized FEM or FVM solution. Due to the large amount of data collected in this study, LW was computationally impractical to run for all time steps, so it was only run on select time steps. Results from reconstruction with LW are presented in Section IX.E.

One method for obtaining a liquid volume fraction is averaging the absolute value of the normalized capacitances [15], called the “mean C method” in this paper. While it is not a tomography technique, the mean C method is simpler and faster than LBP. The mean value, which ideally ranges from 0 to 1, is multiplied by the tank volume to get liquid volume, and then by liquid density to obtain measured mass. In reality, the measurements have nonlinearities, and the normalized capacitances can be outside of the range from 0 to 1.

III. Practical Considerations

A. Propellant Compatibility

As mentioned in the introduction, ECT systems have been tested with cryogens. The simulant liquid in this study was chosen to have a low permittivity, near that of cryogens (see Section IV.B). Since low permittivity liquids are non-conductive and the electrodes are discharged in the ECT electronics, the power dissipation inside the propellant tank is miniscule, on the order of pW/L [12]. The use of liquids with high permittivities, i.e. partially conductive liquids like water or some storable propellants, in ECT systems poses a few challenges. To prevent significant current flow through the conductive liquid in the tank, the electrodes must be electrically isolated from the liquid (and the tank wall) by a low permittivity material. The use of a high permittivity liquid increases electric field nonuniformity and worsens the empty tank assumption for sensitivity matrix calculation. Ref. [14] presents a more physically accurate sensitivity matrix to address this, but since that matrix relies on knowledge of the permittivity distribution, solving the inverse problem becomes coupled and computationally intensive. Displacement Current Phase Tomography is a method related to ECT that uses alternating current (AC) excitation and is more accurate for high permittivity liquids [16].

B. Mass and Tank Size

Discussion of the mass of a potential flight-like ECT system is warranted since this experiment was small scale. Certain components of the ECT system, e.g. electronics package, would essentially have the same mass regardless of rocket or spacecraft size. Because the electrodes need to cover most of the wall, electrode mass, as well as any tank or propellant electrical insulating material (should it be needed), would scale with the wall surface area. Because the system only measures capacitances, the electrodes conduct negligible current, suggesting the electrodes could have a thickness on the order of microns. Potential fabrication methods include electroplating or a vapor deposition process. Thin electrodes mitigate thermal stress cracking/debonding concerns associated with coefficient of thermal expansion (CTE)

mismatch between the electrodes, insulation material, and tank wall. Electrode wiring mass scales linearly with number of electrodes and tank radius.

Consider a hypothetical 16-electrode ECT system applied to a 3 m diameter spherical tank. Electronics (with enclosure) mass might be 3 kg. 10μm thick pure aluminum electrodes, a 0.2 mm thick layer of polyimide insulation, and associated wiring would yield a total system mass of about 14 kg. A 3 mm thick wall aluminum-lithium alloy tank would be approximately 230 kg, making this ECT system about 6% of the tank dry mass. Compared to a tank with propellant, the ECT system represents 0.1% of the tank mass including a 90% fill of LO_2, or 1.2% mass for the same fill level of LH_2. Ignoring other potential benefits, the mass of an ECT system could be substantially lower than the resulting reduction in propellant margin mass. A localized ECT system, perhaps installed only near a sump or vent, could save further mass by forgoing measurement of the entire tank.

Volumetric resolution worsens as radius is increases. Interestingly, the signal-to-noise ratio (SNR) improves as radius increases since electrode area scales with the square of radius, while the distance between opposing electrodes scales with the radius. The SNR improvement can be traded for volumetric resolution by increasing the number of electrodes. The limiting noise source is typically in the ECT electronics, which limits minimum electrode size, ultimately limiting the maximum number of electrodes and volumetric resolution.

C. Internal Tank Features

Many tanks, including the test tank in this study, have internal features. If the features are non-conductive, they will likely not significantly affect the ECT system's accuracy [10]. If the features are conducting to the rest of the tank, they can reduce the accuracy of the ECT system in their vicinity because they will shield parts of the tank and propellant. In addition, conductive surfaces will "intercept" electric field lines, reducing the field strength in regions that are not shielded. Larger conducting features, e.g. a metallic propellant management device (PMD) or baffle, will probably shield more liquid. However, if the conductive features are used as electrodes or have electrodes applied to them, the additional electrodes might increase the accuracy of the ECT system by increasing volumetric resolution.

IV. Experiment Design

A. Objectives and Requirements

The primary objective of the study was demonstration of accurate liquid mass gauging in a small propellant tank using an ECT system during low-G on a parabolic aircraft flight. High level requirements were derived from this primary objective. NASA FOP and the parabolic flight provider imposed many experiment requirements, including, but not limited to, structural, electrical, pressure vessel, and hazards analysis. These, along with the high-level requirements, drove the experiment design and concept of operations.

B. Fluid Selection

Testing the ECT system with a cryogen would have been ideal considering liquid propellants are often cryogens. While cryogens can be flown on research parabolic flights, cost constraints precluded their use in this experiment. Thus, selecting a simulant liquid with relative permittivity as close to cryogenic propellants ($\varepsilon_R \approx 1.2 - 1.6$) as possible was important. All 3M™ Novec™ and FC engineered fluids, as well as mineral oil and distilled water, were surveyed to compile a list of candidate simulants. Fluid dynamic similarity to cryogenic propellants was important for obtaining realistic unsettled fluid configurations. A scaling study was conducted to examine the Bond and Weber numbers of the subscale test tank (0.175 m diameter) with the simulant fluid

candidates and to compare these nondimensional numbers to a “full-scale” tank (3 m diameter) with LH_2, LCH_4, and LO_2. 3M FC-72 [17] was determined to have the best fluid dynamic similarity, and it also has the lowest relative permittivity of the candidate fluids. Dielectric spectroscopy performed at the Applied Physics Laboratory (APL) at KSC confirmed FC-72’s relative permittivity to be within the measurement uncertainty of the datasheet value of 1.7 and showed it had a low dependence on temperature. During the flights, Bond number ranged from near 0 to approximately 100,000 and Weber number from near 0 to approximately 3,000.

FC-72 has a high vapor pressure, so ground handling equipment was designed to prevent as much evaporation as possible within cost constraints. The temperature-dependent liquid properties required accurate tank temperature measurement with time, which the experimental apparatus achieves. The gas volume in the tank consisted of a mixture of FC-72 vapor and air and was assumed to be an ideal gas for state calculations.

C. Apparatus Design and Details

NASA did not do any ECT hardware development as part of this study due to cost and time constraints. A “plug-and-play” experiment apparatus was rented for the duration of the study. The apparatus is shown in Figure 1. The aluminum base plate and frame, ruggedized laptop for displaying the ECT system’s graphical user interface (GUI), Inertial Measurement Unit (IMU, left of laptop), and secondary containment box (top center) are visible. Data was stored on an external USB SSD. The test tank, ECT electronics, and fill/drain hardware were contained inside the sealed secondary containment box bolted to the base plate behind the laptop. NASA provided the power distribution, IMU, external SSD, and ground support equipment (GSE) hardware; all other hardware came with the rented apparatus. This apparatus met or exceeded all design requirements.

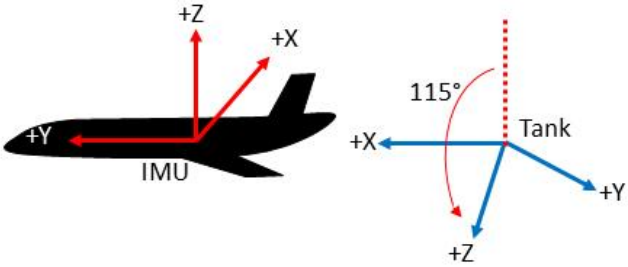

Figure 1 Experiment Apparatus Installed in Aircraft with IMU and Tank Coordinate Systems

The 6 degree-of-freedom (DoF) Analog Devices 16460 [18] IMU, connected to a RaspberryPi 4B, was used for recording motion during testing. This was placed in a case fastened to the apparatus' base plate. Custom software handled IMU data collection and storage, and it was time-synchronized with the ECT laptop clock. IMU +Y was aligned with the long side of the apparatus base plate, IMU +X pointed out away from the tank, and IMU +Z was normal to the apparatus base plate pointing "up". The tank +X axis was aligned with the IMU +Y axis, and the tank was rotated -115º about its +X axis resulting in the tank +Y and +Z axes having components in the IMU -Z direction. Figure 1 shows these coordinate systems. The "horizontal" orientation is shown in Figure 1, where "up" is perpendicular to the baseplate in IMU +Z. Relative to the horizontal orientation, the "vertical" orientation is rotated 90 deg about the IMU +X axis such that the laptop end is pointing up. Ground tests were performed in both orientations. Rotation rates were small for the ground tests, so the there was no need for kinematic transformations of the measured accelerations to account for the difference between the IMU and tank origins. Flight tests were only performed in the horizontal orientation, with the +Y IMU axis pointing in the aircraft forward direction. The experiment was considered a rigid body and the aircraft motion was large relative the test apparatus, so there was no need for kinematic transformations from the IMU origin to the tank origin.

The test tank was made of aluminum and approximately spherical with an internal diameter of 0.175 m. It had eight spherical-octant-shaped, approximately 1 mm thick, electrodes adhered to the inside wall of the tank. Each hemisphere of the tank had four electrodes covering most of

the inside wall surface. The electrodes were insulated from the tank wall and fluid by a solid polymer-composite insulator with a relative permittivity of about 3.5. The gaps between the four electrodes in each half of the tank were 6 ± 1 mm, and the gap between electrodes across the tank split plane was 15 ± 1 mm. The gap uncertainties come from electrode installation placement error and, while their uncertainty was estimated, the actual locations of the electrodes could not be measured due to the rental contract prohibiting the tank from being opened. There was additional geometry inside the tank that was confirmed to exist but not disclosed and therefore not accounted for in this study. The gaps between the electrodes were filled with a solid polymer with a relative permittivity of about 3.5 to prevent liquid from flowing between the electrodes. The gap filler was slightly recessed into the gaps, and none is present within 1.5 mm of the tank split plane or around the fill/drain valve ports. The split plane contained eight aluminum tabs that projected radially 7 mm into the tank; these were extraneous features leftover from a previous iteration of the tank. The tank remained sealed during testing and was equipped with low-volume fill/drain valves to minimize liquid transfer error. This test tank was a prototype; Section X discusses some of its mechanical flaws, error sources, and corresponding suggested mechanical improvements. Simplified internal tank geometry, assuming zero electrode placement error, was created in CAD for usage in simulation and internal volume estimation. Figure 2 shows this model's fluid occupied volume. The octant indentations represent the electrodes, and the embossed strips are the gaps between the electrodes. The tank X-axis is normal to the split plane, which cuts through the center of the widest gap.

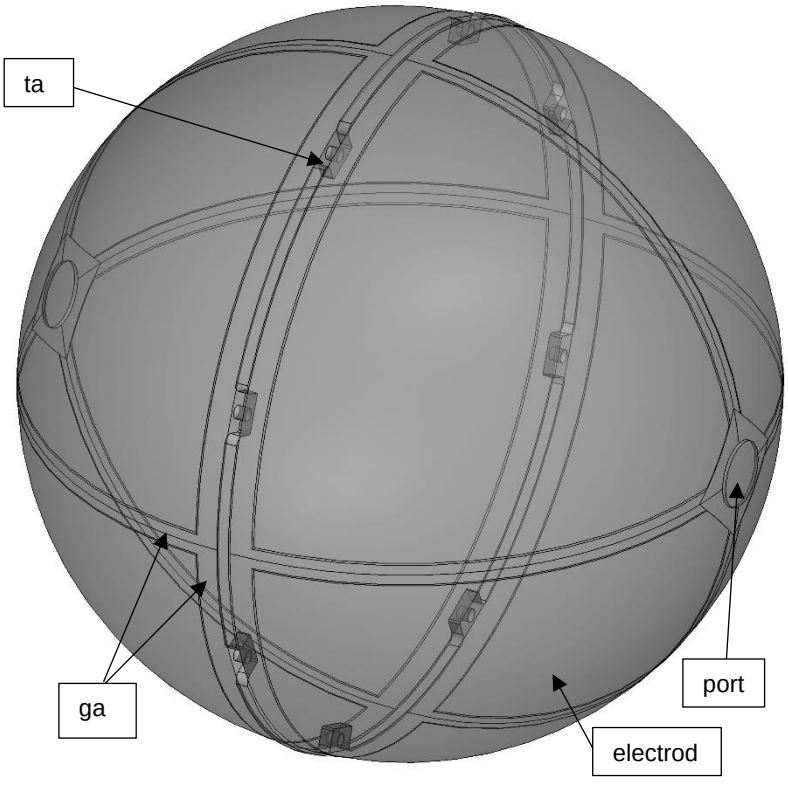

Figure 2 Tank Internal Volume CAD, translucent

A Maxim DS18B20 digital temperature sensor was fastened to the outside wall of the tank. The internal fluid temperature was assumed to be the tank wall temperature since the tank was

operated in temperature-controlled environments (a laboratory or aircraft), sealed in a secondary containment box, and had a large thermal mass and thermal conductivity. Temperatures varied from approximately 23-29 °C over all collected data.

The ECT electronics consisted of a power supply, on-board processor, and capacitance measurement circuitry, with ethernet connectivity for sending data to the laptop. The ECT electronics were mounted to an aluminum plate adjacent to the test tank inside the secondary containment box.

The following data were collected for every ground and flight test: raw capacitances between all electrode pairs (100Hz), tank wall and ECT electronics temperatures (100Hz), 3-axis accelerations and 3-axis rotation rates from the IMU (variable data rate, ≈400Hz), and the actual (scale-measured) mass of liquid in the tank.

V. Ground Testing

Tests were performed on the ground prior to the flight campaign to practice/refine test procedures and to generate data for mass gauging calculations. Capacitances were measured with the tank empty and full and used to normalize measured capacitances (Eq. 3). Temperatures varied from approximately 23-29 °C over all collected data. The various temperatures during the empty and full tests allowed for derivation of temperature corrections of capacitance. Capacitance measurements were taken at 10 fill levels between 0 and 100%, in the horizontal and vertical orientations, in order to derive settled corrections for those orientations (see Section VIII.B).

Impulse free-decay slosh testing was performed on the ground. The apparatus, with the IMU on board, was placed on a rolling cart. The cart was manually pushed along one axis, quickly stopped, and the slosh was allowed to decay. Actuation was repeated once in the horizontal and vertical orientations, for each of 10 fill levels, or notional volume fractions (NVF). “Notional” indicates these target volume fractions were not precisely hit during filling. The actual liquid mass, and therefore actual volume fraction, in the tank for each test *is* known accurately due to filled liquid mass being measured with a precision scale.

VI. Parabolic Flight Testing

The NASA Flight Opportunities Program (FOP) funded the flights of this experiment on a parabolic flight aircraft. The experiment flew on four flights over three days. Fill level was varied between flights: 5%, 20%, 50%, and 80% NVFs were tested, in that order. The actual volume fractions were within 2% of the NVFs. Each flight typically consisted of 30 parabolas: two Martian gravity, three Lunar gravity, and 25 near-0-G (low-G) parabolas. Parabolas are flown five in a row, with the aircraft doubling back on its flight path between each row. With four flights, this totals 100 low-G parabolas over the experiment campaign. Generally, there were a few minutes of 1-G flight between the parabola sets, and about 50 s of hyper-G (≈1.8 G) and 18 s of low-G for each parabola. Data was recorded from before takeoff until parking at the hangar after landing. The low-G portions of the parabolas were somewhat unsteady, oscillating around 0 G, which is why they are referred to as “low-G” in this paper. Hyper-G and level flight were steadier. Every parabola was unique, and different pilots resulted in slightly different motion characteristics. The unsteadiness of the low-G portions was actually a benefit for this experiment because it drove significant, somewhat random, liquid motion and resulting distributions inside the tank, allowing for the characterization of the low-G mass gauging error for this particular ECT system. The Bond number range of the low-G portions is similar to that of

some space vehicle reaction/attitude control maneuvers, and the high-G portions are analogous to propulsive burns, albeit without the corresponding propellant tank draining.

VII. Electrostatic Simulation

Electrostatic simulations of the empty tank were necessary for deriving the sensitivity matrix (see Section II), which was necessary for ECT reconstruction. These simulations only had to be done once. Software with an electrostatic solver, STAR-CCM+ [19], was used for all simulations. A mesh independence study was conducted to find an adequate mesh resolution. Since the test tank had three-plane symmetry, this symmetry was enforced on the mesh, i.e. the mesh of each of the eight spherical octants associated with each of the eight electrodes was identical, which facilitated consistent numerical error. A nominal empty or full simulation used the following boundary conditions: the electric potential of the tank wall and seven electrodes were held at 0 V and the eighth electrode was held at a non-zero potential. The simulated electric field was imported into MATLAB [20] and transformed to yield the electric field from the perspective of the other seven electrodes being individually raised to a potential. A similar transformation process was used for the simulated electrode pair capacitances, yielding an 8x8 capacitance matrix. The capacitance matrix is symmetric, and the diagonal of the matrix are self-capacitances, which are not used in the present solution. This left 28 unique capacitances. Total simulation time was less than one minute.

Additional electrostatic simulations were performed to generate “simulated data” for testing ECT algorithms. This followed a similar process to the empty tank simulations, except a specific permittivity (test liquid) distribution was applied to the tank volume. Since this distribution was not always symmetric, a simulation with each electrode individually raised to a potential had to be run. The normalized simulated capacitances were used to develop and test the ECT algorithms because, unlike the test data, the true (simulation input) liquid distribution was known, which allowed for error calculation, and the simulated data did not contain electrical noise and other sources of error.

Simulated and test capacitances were compared for the empty and full cases in order to validate the electrostatic simulation. Additionally, reconstruction comparisons were made between simulated data and test data for settled (known liquid distribution) cases. The normalized simulated and test capacitances were similar enough to result in qualitatively similar reconstructed 3D distributions when processed with the same ECT reconstruction algorithm. The validated simulation methodology implies that any remaining error in ECT (test) mass gauging and reconstruction, after accounting for known uncertainties, comes from the ECT algorithm, tank design/fabrication flaws, and other ECT system error sources.

VIII. Data Processing

A. Measurement Data Processing

ECT system measured capacitances, tank temperature, IMU, and scale measurements were read into MATLAB for post-processing. The raw capacitance data were filtered with a high-order, 10 Hz-cutoff, low-pass filter to reduce electrical noise. 10 Hz is more than twice the highest third-mode slosh frequency of the tank, meaning that liquid motion signal content was retained. Capacitances of like-pairs of electrodes were averaged, then normalized, leaving 28 unique capacitances vs. time. Temperature and IMU data were also low-pass filtered. Initial fluid state in the tank for each test was determined by the temperature and liquid mass immediately after a filling procedure was completed. The initial fluid state and the transient temperature were used to account for evaporation and condensation; the time-varying, temperature-corrected,

actual liquid mass and volume were calculated and stored. Liquid mass losses during filling were considered. Empty and full tank capacitances measured over time and in multiple tests were used to derive the linear dependence of capacitance on temperature. Notably, temperature corrections were relatively small, 0-0.6 %/ºC.

Table 1 is a matrix of time-averaged measurements of the empty tank capacitances. Each row index and each column index represent an electrode number (see Eq. 1), so each element is the capacitance for that electrode pair. The diagonal elements are self-capacitances, which are not useful, so they are shown as zero. This tank geometry (nominally) has five unique electrode pair configurations, listed in order of increasing capacitance magnitude: 1. Opposing (across tank), 2. Diagonal across the split plane between tank hemispheres, 3. Diagonal within a hemisphere, 4. Adjacent across the split plane between tank hemispheres, and 5. Adjacent within a hemisphere. With an ideal geometry and no noise, like the simulations, all of the capacitances of a given electrode configuration will be identical, and the empty (and full) tank capacitance matrix is symmetric. An asymmetric capacitance matrix can be caused by noise, tank geometry asymmetries, and fluid distribution asymmetries. Low-pass filtering for electrical noise and time-averaging made the random noise negligible for the capacitances presented in Table 1.

Table 1 Empty Tank Capacitance Matrix, Farads

0	5.71E-13	7.36E-14	5.24E-13	2.01E-13	5.20E-14	2.37E-14	5.97E-14
5.72E-13	0	5.27E-13	7.37E-14	5.97E-14	1.94E-13	5.74E-14	2.33E-14
7.40E-14	5.33E-13	0	5.49E-13	2.28E-14	5.60E-14	1.91E-13	5.23E-14
5.25E-13	7.55E-14	5.51E-13	0	5.24E-14	2.14E-14	5.55E-14	1.72E-13
2.01E-13	6.13E-14	2.3E-14	5.18E-14	0	5.36E-13	7.23E-14	5.46E-13
5.16E-14	1.95E-13	5.69E-14	2.25E-14	5.40E-13	0	5.64E-13	7.42E-14
2.33E-14	5.77E-14	1.90E-13	5.70E-14	7.31E-14	5.67E-13	0	5.29E-13
5.97E-14	2.4E-14	5.28E-14	1.74E-13	5.53E-13	7.68E-14	5.38E-13	0

The matrix of test measured empty tank capacitances in Table 1 is not symmetric, which supports the assertation that tank geometry asymmetries exist. The mean of the all elements of the same electrode configuration approximates the nominal, zero-error, capacitance for that electrode configuration. Each element of the matrix in Table 2 is the percent difference between the corresponding element of the matrix in Table 1 and the mean of the all elements of with its electrode configuration.

Table 2 Empty Tank Capacitance Matrix Electrode Configuration Variation, %

0	4.7	-0.8	-3.8	6	-6.9	3	6.8
4.8	0	-3.3	-0.6	6.9	2.2	2.8	1.4
-0.2	-2.2	0	0.7	-0.7	0.2	0.5	-6.4
-3.7	1.8	1.1	0	-6.1	-6.8	-0.7	-9.4
5.8	9.7	-0.1	-7.2	0	-1.8	-2.5	0.2
-7.6	2.9	1.8	-2.2	-1	0	3.4	0
1.2	3.3	0.3	2	-1.4	3.9	0	-3
6.8	4.3	-5.5	-8.3	1.4	3.5	-1.4	0

There is significant variation in capacitance for a given electrode configuration, up to 9.7% for configuration 2, and 9.4% for configuration 4. This is a consequence of the electrode placement error mentioned in Section IV.C.

B. Settled Corrections

When the liquid was settled, the relationship between actual and measured mass (or volume) was not linear due to various ECT system errors. During ground testing (Section V), capacitance measurements were taken at 10 fill levels between 0 and 100%, in the horizontal and vertical orientations in order to derive settled corrections for volume gauging in those orientations. These corrections allow for the removal of some of the nonlinearity in the gauging measurements. A settled correction was applied when the IMU acceleration vector and CM angles (with respect to the orientation's "up" axis) were within specific, small angle limits, i.e. when the liquid was mostly settled in the orientation for which the correction was derived. For the parabolic flights, this resulted in the settled corrections being tapered in or out during the transitions between low-G and high-G.

Most real launch vehicles and spacecraft have only one primary acceleration axis, so a fill and drain test need only be performed with the tank in that orientation to obtain data for deriving settled corrections. They are referred to as "corrections" in this study because they were applied after the data was collected. However, in a real application, they would be derived beforehand and programmed into the real-time processor of the ECT system, making them more of a settled "calibration" than a correction.

All fully settled portions of ground and flight-day (but not in-flight) data were identified. The 28 capacitances were time-averaged for each portion. The normalized capacitances were averaged in the mean C method (see Section II) to calculate a volume fraction, which was multiplied by tank volume to obtain a measured liquid volume point. This was done for every portion, yielding multiple measured volume points. This was repeated with LBP. Two types of settled corrections were derived.

The first type, called "capacitance corrections", fit 28 splines to the 28 measured capacitances across measured fill levels. An additional 28 splines were fit for the same capacitances across actual fill levels. Subtracting these yields 28 splines that provide the normalized capacitance errors given the measured volume (one for each electrode pair). These were computed for each orientation and each method (mean C and LBP). The capacitance error splines are evaluated at a measured volume, and the resulting capacitance errors are subtracted from the measured capacitances to correct them. The measured volume is then recomputed using the corrected capacitances.

The second type of correction, called a "volume correction", was derived by fitting a spline to the actual vs. measured volume points, and the fit was evaluated at measured volumes to obtain corrected measured volumes. This correction does not affect (or correct) any capacitance measurements. The volume correction process is the same for both the mean C and LBP methods, but their spline fits are different.

Table 3 lists the minimum and maximum errors of all of the settled measured volume points (see above) for the mean C method and LBP for both horizontal (H) and vertical (V) orientations. Liquid volume error is defined as $e = \frac{v_m - v_a}{v_a}$, where v_m is the ECT measured liquid volume and v_a is the actual liquid volume in the tank at that fill level. "Capacitance" indicates capacitance corrections and "Volume" indicates volume corrections.

Table 3 Settled Correction Methods Error Comparison

Correction Method	H Min Error, %	H Max Error, %	V Min Error, %	V Max Error, %
mean C, Uncorrected	-7.8	6.9	-13	68
mean C, Capacitance	-12	1.2	-11	7.0
mean C, Volume	-1.8	2.2	-2.4	2.2
LBP, Uncorrected	-6.6	32	-17	134
LBP, Capacitance	-7.1	2.5	-13	12
LBP, Volume	-2.1	2.0	-2.5	1.9

Overall, the volume corrections resulted in less error and improved gauging linearity more than the capacitance corrections. All results presented in Section IX used the volume correction type. The corrected volume data was used in the calculation of the other parameters, e.g. mass.

Theoretically, it would be possible to perform settled tests or simulations in many orientations and fill levels, which would allow settled corrections to be derived for any fill level and orientation. These could then be applied whenever the liquid surface is close to planar, using acceleration and/or CM data to determine orientation. Furthermore, these would potentially allow for the correction of transient measurement variations due to approximately-planar sloshing. However, it was decided that this was not worth the effort because of filtering (Section VIII.C) and the fact that this project is primarily concerned with low-G, for which corrections of this type are not possible because the liquid may be in a nonplanar/unsettled configuration.

C. Liquid Motion Filtering

This section describes filtering of the mass gauging measurement. Filtering of the capacitances to reduce electrical noise is covered in Section VIII.A. As will be discussed in Sections IX.A and IX.B, the liquid motion (slosh) caused variability in the gauging results, requiring the ECT-computed liquid mass (or volume) to be filtered in order to reduce measurement variability and improve the ECT system accuracy. “Filter” will henceforth refer to filtering out the liquid motion effects in the ECT gauging results.

Only filters that could be implemented in real-time were considered. Linear phase finite impulse response (FIR) low-pass filters, including a backwards-looking moving average smoother, meet the real-time criterion but have phase delays. The phase delay is approximately the width of the window for a backwards-looking moving average. Rate limiting filters are a type of filter that limits the rate of change of the input signal. For each new time point, the rate-of-change of the input signal, computed by finite difference, is compared to a rate limit. If the rate limit, which can be positive or negative, is violated, the output value at the new time point is calculated by the rate limit multiplied by the time step added to the previous data point. Higher rate limits result in less filtering because the output signal more closely tracks the input signal. A rate limiting filter is only active when a rate limit is violated, but rate limiting during prior time steps can cause a transient offset between the input and output signals, i.e. phase delay. The phase delay is worse for lower rate limits (higher filtering) because it takes more time steps for the output to track changes in input. The phase delay from a rate limiting filter can be lower than a backwards moving average when both are designed for a similar magnitude of noise reduction. To further reduce phase delay, the offset can be reset by setting the output signal equal to the input signal (offset=0) if specified (system dependent) criteria are met. Rate limits should be selected to bound the rates of the system. Having different positive and negative rate limits that do not correspond with the physics of the system can result in a low or high bias. For

example, having a small positive rate limit and a large negative rate limit for filtering the results of a steady (but noisy) process will result in the output signal being biased low, while having equal magnitude positive and negative rate limits would not result in a bias. Rate limiting is not computationally intensive, and backward differences permit real-time usage. In filter testing, differences in output for finite difference accuracy orders over three were negligible, thus third order was selected. One disadvantage of rate limiting a signal is that the output signal is piecewise linear, not smooth. If a smooth output signal is required, either the rate limited output must be smoothed, or a different filter, e.g. moving average, must be used.

In a real flight tank the various fill and drain rates will be knowable to within some uncertainty, so rate limit tables can be pre-generated for a rate limiting filter implemented in the tank's ECT system. A launch vehicle upper stage will be used as an example. For an on-orbit cryogenic tank when no propellant is being consumed, the negative rate limit could be set to the worst-case boil-off rate. Main engine burn results in the highest drain rate, and the drain rate, along with its uncertainty (for adding margin), will be known from engine modeling and testing. The ECT system would know when the engine is burning, look up the negative rate limit in a table, and set the negative rate limit to that for the duration of the burn. Because the ECT system will have a settled liquid (in primary thrust axis) calibration (see Section VIII.B), the accuracy during settling or a burn will be higher, which would allow for the use of the offset reset feature to reduce phase delay after a transition from low-G to high-G.

After comparing various filters, a rate limiting filter was selected for the ECT system in this study. No liquid was added to, or drained from, the tank during a test, meaning the rate limit could theoretically be zero, but this is equivalent to setting the output signal equal to the first time point of the input signal and is akin to a 0 Hz cutoff frequency in a classical low-pass filter, which is not useful. Similar to the launch vehicle upper stage example above, the rate limiting filter for this ECT system utilizes the offset reset feature at transitions from unsettled, low-G to settled, high-G. The "settled, high-G" state was determined by when the IMU acceleration vector and CM angles (with respect to the horizontal orientation's "up" axis) were within specific, small angle limits, i.e. when the liquid was mostly settled in the horizontal orientation. The selection of rate limits is discussed in Section IX.B.

D. Uncertainty

Formal uncertainty calculations were performed on all data. All reported errors are for a 95% confidence level. The adjective "actual" will refer to scale-derived measurements and "ECT-measured" will refer to capacitance-derived measurements.

CAD of the tank was used to calculate an accurate estimate of total internal volume (2.792 L), which is estimated to have an uncertainty of ±1% and no random error. The digital tank temperature sensor has a fixed bias error of 0.3 °C, and has internal filtering, so no random error was reported. The test liquid [17] datasheet provides equations for density and vapor pressure versus temperature without reported uncertainties, so their uncertainties are assumed to be negligible. Temperature uncertainty was propagated through these equations. The precision scale was calibrated and had a fixed bias error of ±0.01 g and a negligible random error. The fill operation evaporation loss was measured to be 4 ±2 g per operation during the flight campaign (±1 g per operation during the ground test campaign) and used to correct the scale-measured mass. Phase change in the tank was calculated. These uncertainties were fully propagated through calculations to provide the transient uncertainties for actual liquid mass, volume, and volume fraction.

The ECT system's capacitance measurements had a fixed bias error of 2.5e-17 + 0.005C F, where C is the measurement value. The capacitance measurement random error was assumed

to be normally distributed and calculated from the standard deviation of static measurements for each electrode pair, generally on the order of 1e-16 F. The capacitance measurement, temperature, and temperature correction linear fit uncertainties were propagated to the empty and full capacitance measurements and normalization, resulting in transient uncertainties for the normalized capacitances.

For the mean C method, the normalized capacitance uncertainty was propagated through the average to obtain the uncertainty on ECT-measured volume fraction, and ultimately volume uncertainty along with ECT-measured mass uncertainty. Normalized capacitance uncertainty was propagated through LBP reconstruction calculations using Monte Carlo, i.e. random sampling of the normal distribution of the normalized capacitance. A normal distribution was fit to the resulting volumes, and the standard deviation of that fit was used to calculate random error for ECT-measured volume due to the normalized capacitance uncertainty. The volume uncertainty was propagated to volume fraction and mass uncertainties in a similar manner as the mean C method. Random uncertainty due to the settled corrections, which, in uncertainty terminology, are actually a form of fixed bias (offset) error correction, was determined to be negligible. This make sense because there is unique volume for every fill level in a given tank orientation. Of course, the orientation had uncertainty, but this was captured in the random uncertainty on the mean measurements instead of in the settled corrections.

Some effort was spent quantifying the error of the LBP *process*, i.e. errors associated with linear and approximate-inverse assumptions of the LBP reconstruction algorithm applied to an inherently nonlinear and ill-posed problem. A code was written to rapidly generate millions of random unsettled-liquid-like distributions, simulate the capacitances using the sensitivity matrix, perform LBP, calculate volume error, and then calculate fixed bias and random error versus fill level. This extra uncertainty was included in transient results when the liquid was in an unsettled state, resulting in a wider LBP confidence interval during those times. The LBP process random error was also included in the uncertainty intervals for mean measurement results. The sensitivity matrix elements were assumed to have no uncertainty, and errors associated with tank geometry, which are known to exist but were never quantified (see Section IV.C), are still not accounted for. A similar method was used to estimate the errors associated with the mean C method process, but this was ultimately not used because it was determined to be unnecessary.

The uncertainty on the total tank volume was accounted for in the mean C method, but not LBP because LBP returns a volume directly. In order to account for tank volume uncertainty in the total uncertainty of the LBP results, an uncertainty would have to be calculated for the volume of each cell in the simulation mesh. The cell uncertainties would then have to be propagated through the sensitivity matrix calculation and the liquid volume calculation step after reconstruction. This was impractical and neglected.

In Section IX, total accounted-for uncertainty will be presented as a 95% confidence interval band around the gauging curves. Maximum liquid mass errors, defined relative to both actual liquid mass and full-tank liquid mass, from the transient results are also reported. Additionally, for every test, an uncertainty interval at a 95% confidence level about the mean of the test's measurements is reported as a "time-averaged accuracy". These results provide estimates of this ECT system's accuracy, the determination of which was the primary objective of this experiment.

IX. Test Results and Discussion

A. Results Primer

In the interest of conciseness, results presented in this section represent a subset of the large amount of test data collected. The tests selected for presentation are representative; they are not necessarily the tests with the highest accuracy gauging. Unless otherwise noted, liquid mass error is defined as $e = \frac{m_m - m_a}{m_a}$, where m_m is the ECT measured liquid mass and m_a is the actual liquid mass currently in the tank, which was derived from precision scale measurements. Note that this error is *not* relative to a full tank. The "Mean C" curve is the mean C method with the settled corrections. The "LBP" curve is LBP with the settled corrections. The "rate limited" curves have most of the liquid motion effects filtered out by a rate limiting filter (see Sections VIII.C and IX.B). The "actual" line is a scale-derived measurement. The 95% confidence interval for each parameter is plotted as a lighter-shade band ("95% CI" in the plot legends) around the parameter curve and represents the known transient uncertainty (see Section VIII.D). For example, in the liquid mass plots, the CI represents the uncertainty of the transient mass measurements. The liquid mass error curves are an estimate of this ECT system's transient accuracy, and the distance between the CI and 0 on these plots represents unaccounted-for system uncertainties.

The ECT sensitivity varied throughout the volume of the tank. Liquid near the edges of an electrode, where the electric field was highest, had a larger effect on capacitance of that electrode than liquid in the center of the tank, where the electric field was the lowest. The liquid moving between areas of high and low sensitivity caused variations in the capacitance measurements, thus causing oscillations in the mean C method results. The sensitivity matrix used in LBP, and many other ECT algorithms, accounts for some of the volumetric sensitivity. However, the ill-posed nature of the inverse problem (see Section II), along with the capacitances variability and inaccuracies in modeled geometry, resulted in the variation in the LBP results. The uncertainty of the LBP process for random, unsettled liquid configurations was characterized (see Section VIII.D) and can be seen as a widening of the LBP CI during unsettled portions of the tests.

B. Liquid Motion Filtering: Selection

The liquid gauging results were filtered to reduce measurement variability and improve the ECT system accuracy. Data from one ground and one flight test are shown for comparing the effectiveness of different filters. Figure 3 is a plot of corrected liquid volume vs. time from the 50% NVF free-decay ground test with a zoomed inset plot of the last decay portion. Figure 4 is a plot of corrected liquid volume vs. time from one set of five parabolas from the 50% NVF flight. Figure 5 is zoomed in on the last low-G portion of Figure 4. The "ECT C Corrected" curve is the corrected mean C method, which is filtered with different techniques. The same filtering is applicable to corrected LBP results (or the results from any other ECT method). The "30s MA filter" applies a moving average (MA) with a backwards-looking 30 s window. While somewhat arbitrary, a 30 s window was chosen based on approximate timescales for common upper stage maneuvers and slosh, and even though a larger window would smooth out the liquid motion variations more, it would cause worse phase delay. The "rate limit" curves utilize a rate limiting filter (described in Section VIII.C) with different rate limits. The "high" rate limit was estimated from the liquid oxygen consumption rate in a 3 m diameter-class launch vehicle upper stage during main engine burn, scaled by the volume ratio of the test tank to the stage's tank. It is considered a realistic bound for a negative (drain) rate limit. The "medium" rate limit is 1/7th the high rate. While the high rate limit generally results in less filtering than the MA, the medium rate limit value was set to result in more. The "low" rate limit is 1/10th the medium rate. Both positive

and negative rate limits have the same magnitude to prevent an output bias because the test tank was filled and drained at the same (zero) rate during tests. Although a rate limit of approximately zero is physically accurate for these tests, this results in all but the first data point being ignored, which is not useful. Liquid volume is used in Figures 3-5, but the same rate limits are applicable to liquid mass when multiplied by liquid density.

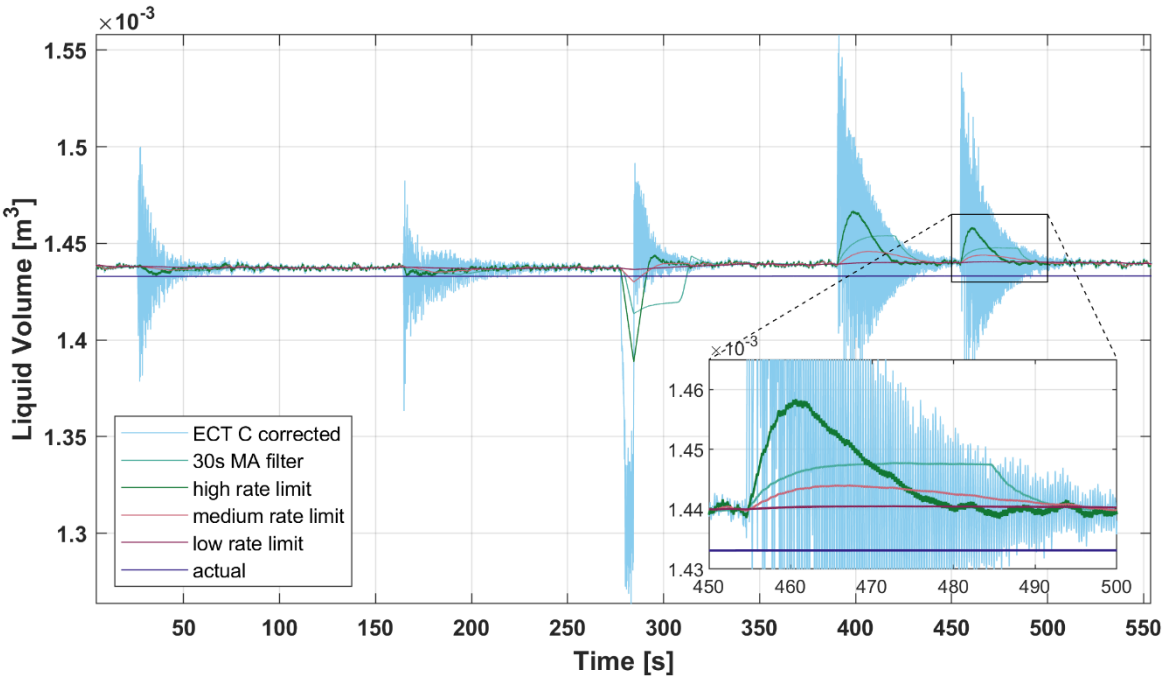

Figure 3 Filter Comparison (50% NVF, impulse free-decay test)

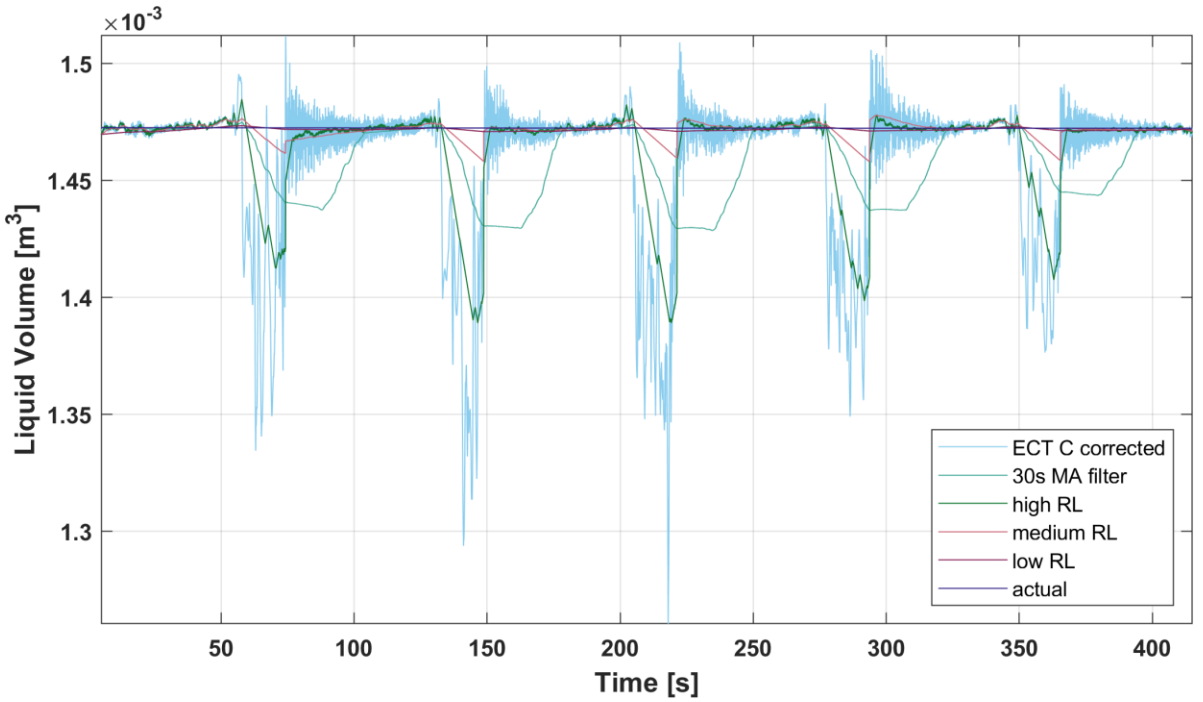

Figure 4 Filter Comparison (50% NVF flight, 5 parabolas)

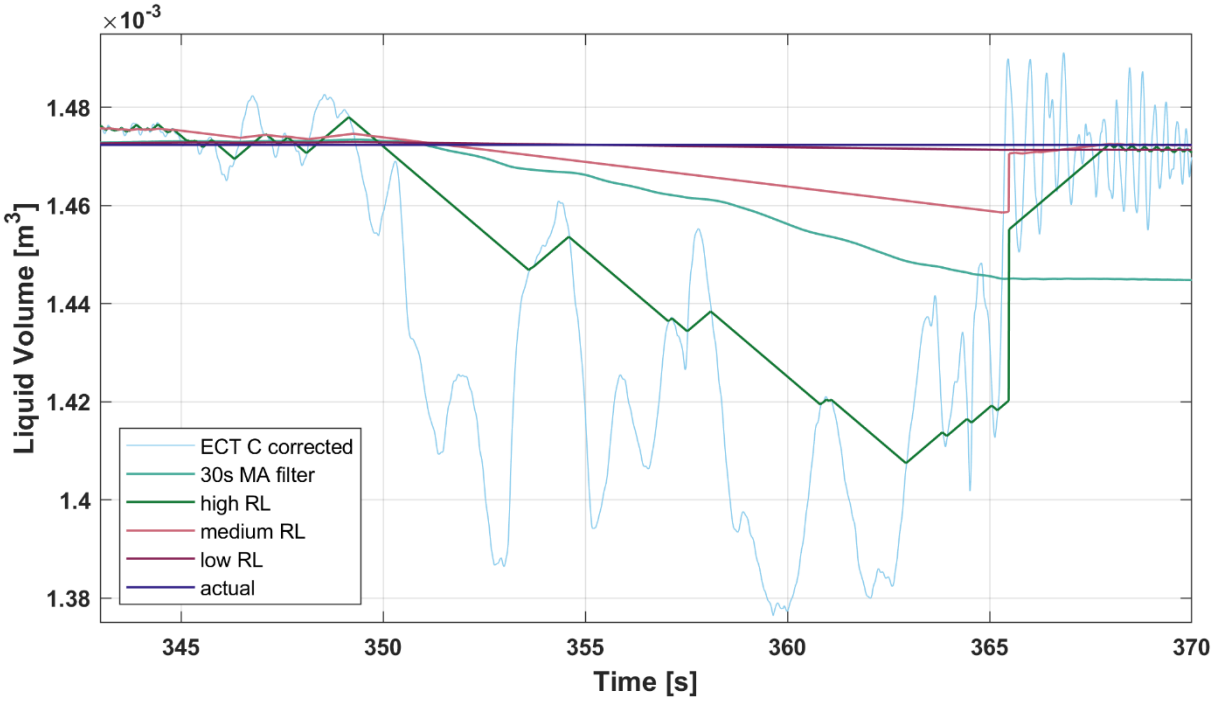

Figure 5 Filter Comparison, Parabola 5

The effectiveness of the 30 s MA filter at suppressing the oscillations from slosh is between that of high and medium rate limits. In Figure 3, the MA line changes slope around 485s because it is backwards looking, and the moving average contacts the rapid change in the “ECT C Corrected” curve around 455 s (485-30). Similar slope changes are visible in the MA line in Figure 4. The rate limited curves exhibit less phase delay than the MA filter. Phase delay is further reduced by the use of the rate limiting filter’s offset reset feature (see Section VIII.C), the

effect of which can be seen as a jump in the high and medium rate limit curves in Figure 5 near 365 s. The offset reset feature was not used in any of the rate limited ground test results because it did not seem to help, but it was used in the rate limited flight test results because it seemed to help more often than not. Not using the offset reset feature, e.g. where the high-G gauging uncertainty is high, still results in less phase delay than the moving average filter. The high rate limit retained some of the signal oscillation, while the low rate limit effectively removed all oscillation. While somewhat arbitrary, this range of rate limits was chosen to demonstrate their effects on filtering transient gauging data. The medium rate limit was selected to create the "rate limited" curves in Sections IX.C and D. Despite the low rate limit being the most physically relevant to this test tank and resulting in the lowest error, the authors felt that demonstrating the effects of a higher rate limit was useful and that the medium rate limit offered a good balance.

While a rate limiting filter was chosen for this study using the above process, many other filters could have been used instead to filter out the variations due to liquid motion. A comprehensive examination of optimal filters for various, specific applications is outside of the scope of this paper.

C. Ground Test Results

Transient plots of motion data, liquid mass, and liquid mass error are presented from the 50% NVF impulse free-decay test. Transient liquid mass and mass error plots from the 5%, 30%, and 70% NVF impulse free-decay tests are also presented in this section, with additional plots in Appendix A. Figure 6 shows the 3-axis accelerations and 3-axis rotation rates measured by the IMU in the IMU axes for the 50% NVF test in both horizontal and vertical orientations. This is presented first to quantitatively characterize the primarily single-axis motion of the impulse tests.

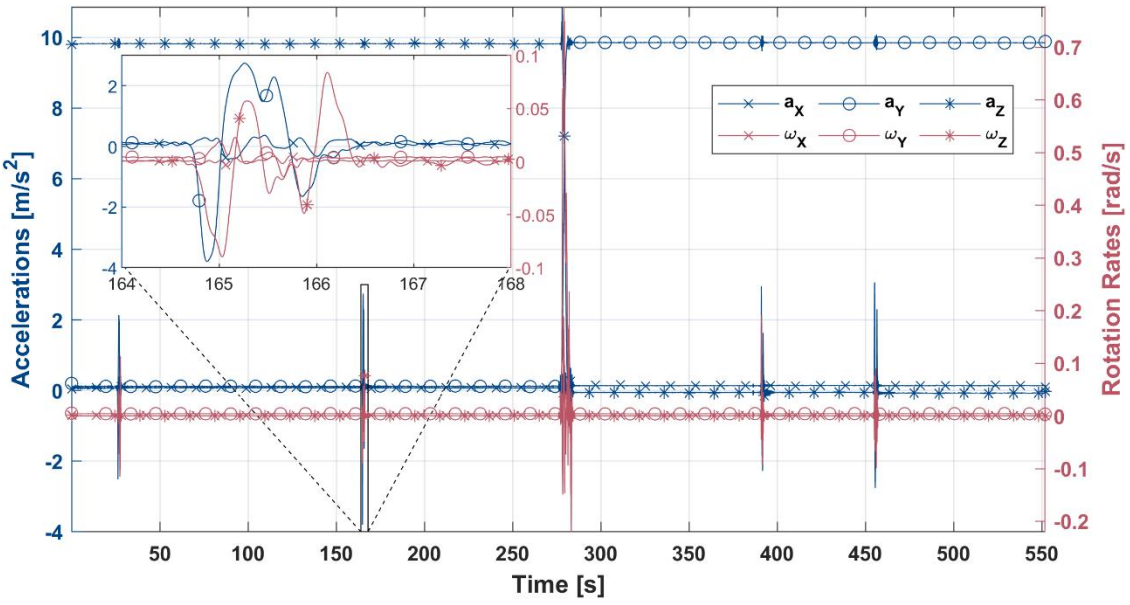

Figure 6 IMU Data, 50% NVF Ground Slosh Test

Refer to Figure 1 for coordinate system and experiment orientation information. The experiment started in the horizontal orientation (a_Z reads 1 G), was manually given two impulses, rotated up to the vertical orientation (a_Y reads 1 G) around 280 s, then given two impulses. Each impulse was primarily in one axis, along Y in the horizontal orientation or along Z in the vertical orientation. The time between impulses allowed for the slosh to decay. This was the standard process for all of the ground slosh tests. The inset plot in Figure 6 is zoomed in on

the second impulse. The initial push, slow, reverse, and stop accelerations are all visible in a_Y. There were minor oscillations about all axes. This motion profile is representative of all of the horizontal orientation impulses in the ground testing. The vertical orientation impulses were similar, except with motion primarily in the Z direction instead of Y, and the minor oscillations were a little (1-3x) larger, but still relatively small. The reason the oscillations were larger was because the experiment was sitting on its end with the long side of the baseplate pointing up, which allowed the apparatus to rock more than in the horizontal orientation. Breaking waves were audible in the tank for many fill levels' impulses, meaning the impulses were generally strong enough to exciting vigorous sloshing.

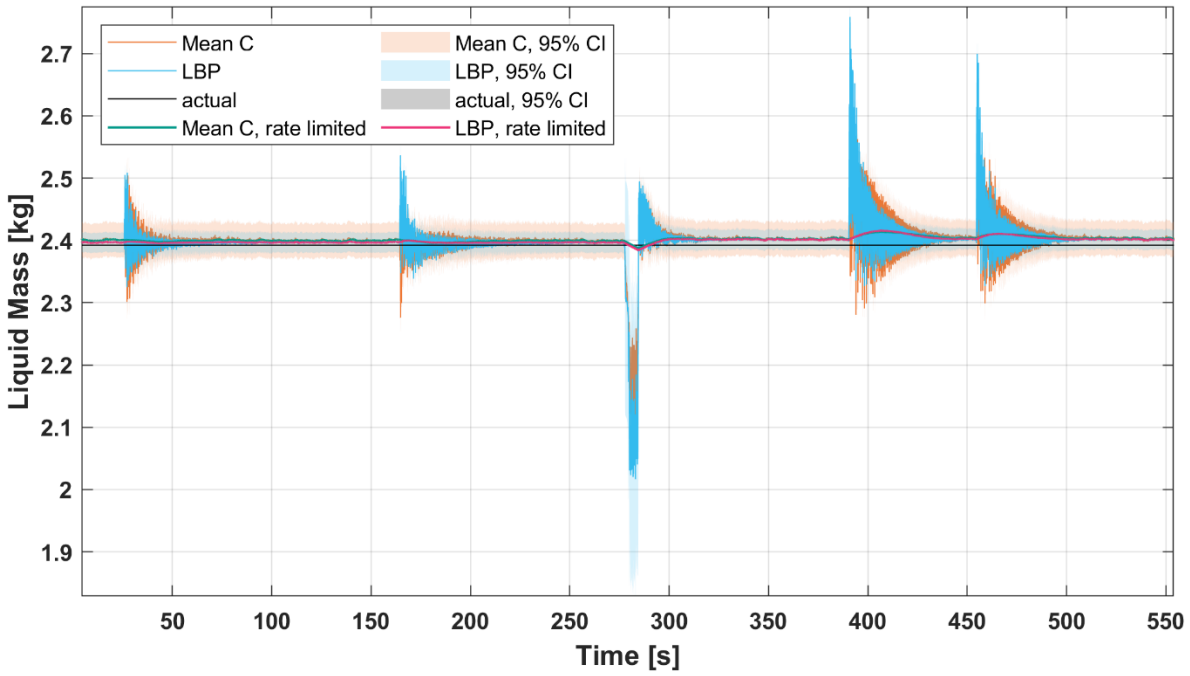

Figure 7 ECT Liquid Mass vs. Time, 50% NVF Ground Slosh Test

Figure 7 and Figure 8 are for the same test shown in Figure 6. The impulses caused a slosh wave inside the tank that decayed over time due to damping. The uncorrected results had different offsets for both orientations and both methods that the settled corrections corrected. When the liquid was mostly settled, the actual liquid mass was within the corrected mean C method's and LBP's CIs, indicating good accuracy. The only portion of this plot that did not have a settled correction applied was during the 90 deg rotation to the vertical orientation (near 270s) because the liquid was not settled and not in an orientation for which a correction had been derived. The fully settled liquid mass value for each orientation was nearly constant. The mean C method results have a wider CI than the LBP results because the uncertainty of the total tank volume is relatively high and was propagated to the total uncertainty calculation for the mean C method volume, while LBP returns a liquid volume directly, so tank volume uncertainty is not included in its total uncertainty. The only exception to this is when the liquid is unsettled during the rotation, where the aforementioned widening of the LBP CI is visible. The comments from this figure apply to the other ground test results and will not be repeated for sake of brevity.

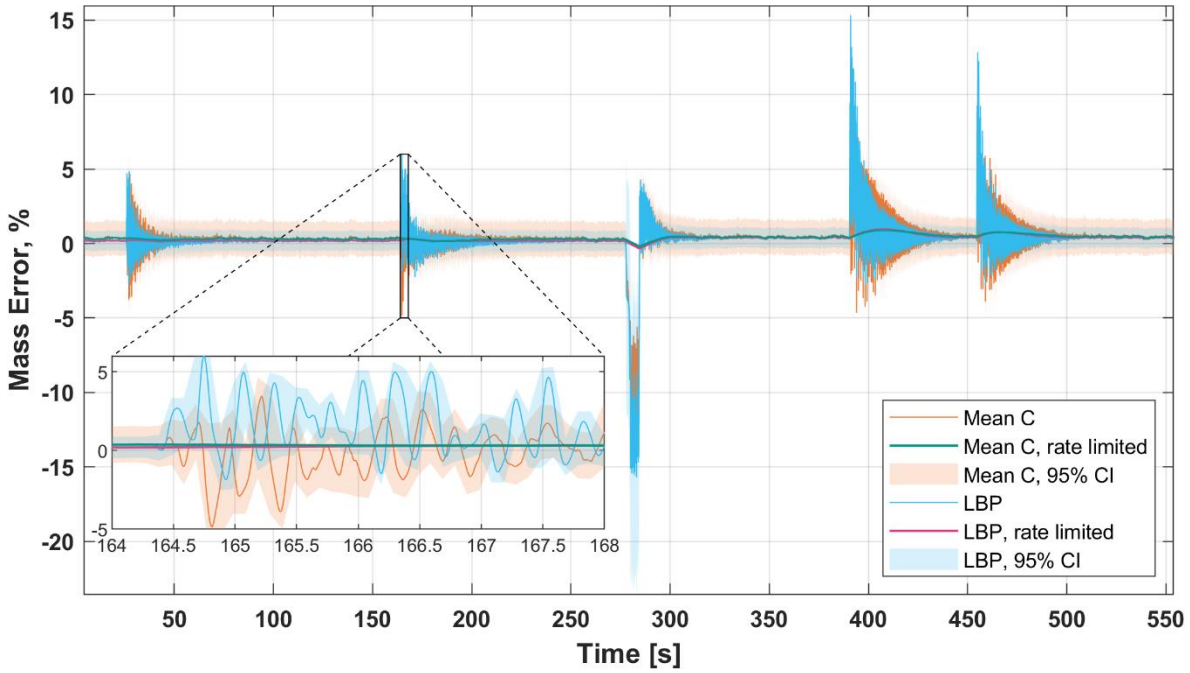

Figure 8 ECT Liquid Mass Error vs. Time, 50% NVF Ground Slosh Test

Figure 8 is the percent error calculated from the transient data shown in Figure 7. As mentioned previously, liquid mass error is defined relative to the actual liquid mass currently in the tank, not to a full tank. The larger error in the vertical orientation than the horizontal orientation was likely due to the large electrode gap being more exposed to fluid in the vertical orientation (see Section IV.C). It is easier to compare the mean C and LBP methods in the zoomed inset plot. Some features are present in both curves, but they can also exhibit no correlation or anti-correlation. The slosh oscillations in both methods have similar magnitudes and decay at approximately the same rate. Tabulated maximum absolute value errors for all tested fill levels for the mean C method and LBP are presented in Table 4 and Table 5, respectively. In all of the tests, the corrected mean C method and LBP error curves were near 0% when the liquid was mostly settled, indicating good accuracy. Filtering out the liquid motion effectively increased the mass gauging system accuracy.

Figures 9-14 are plots of liquid mass and mass error for the 5%, 30%, and 70% NVF tests. Plots of volume fraction and the transient results from other fill levels are included in Appendix A.

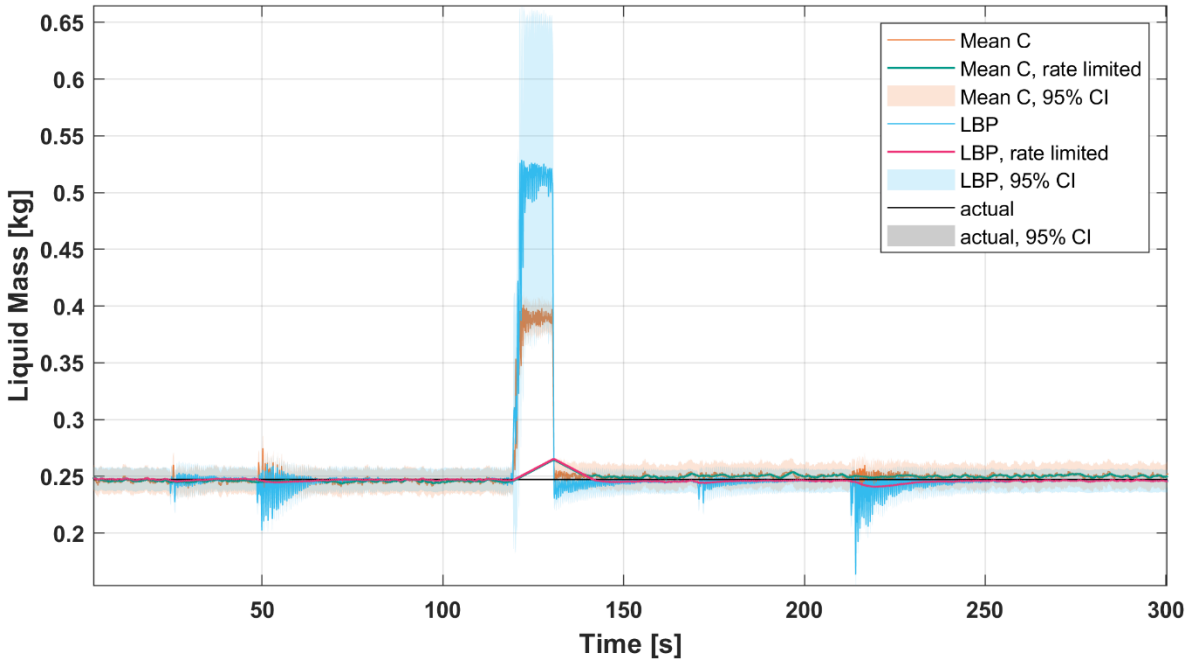

Figure 9 ECT Liquid Mass vs. Time, 5% NVF Ground Slosh Test

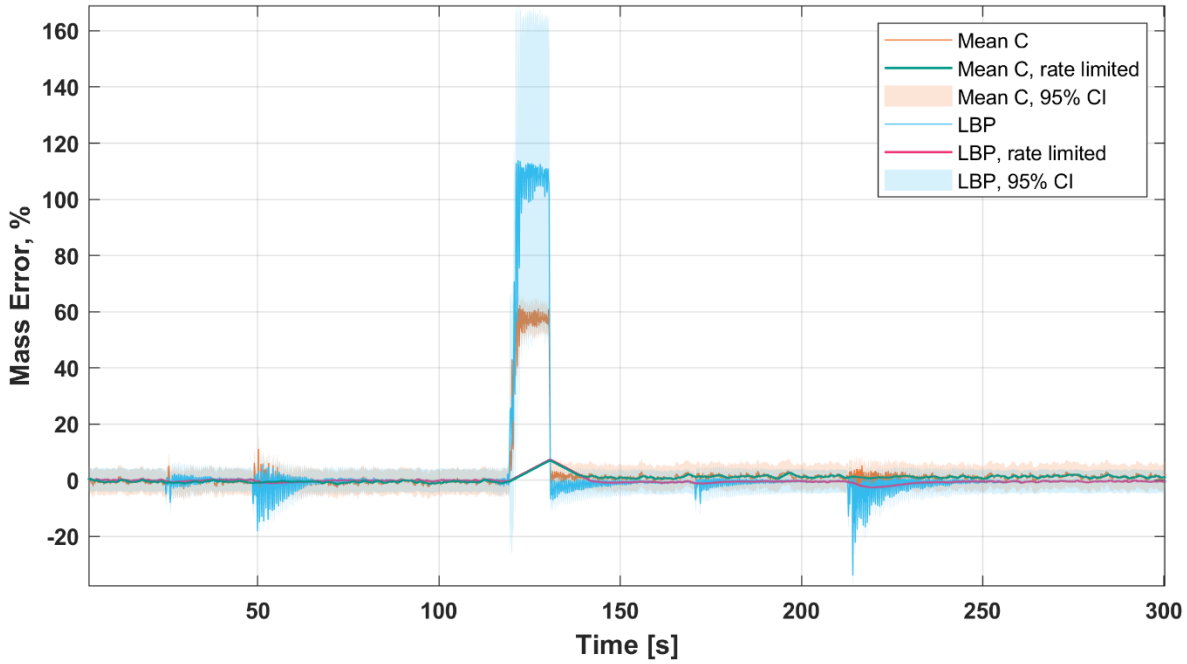

Figure 10 ECT Liquid Mass Error vs. Time, 5% NVF Ground Slosh Test

The lowest fill levels tended to have higher errors, particularly during the rotation. Shown in Figure 10, the liquid reorienting during the rotation in the 5% NVF test resulted in the highest error seen during ground testing. Once the liquid was mostly settled in the vertical orientation, the settled corrections were applied, resulting in low error.

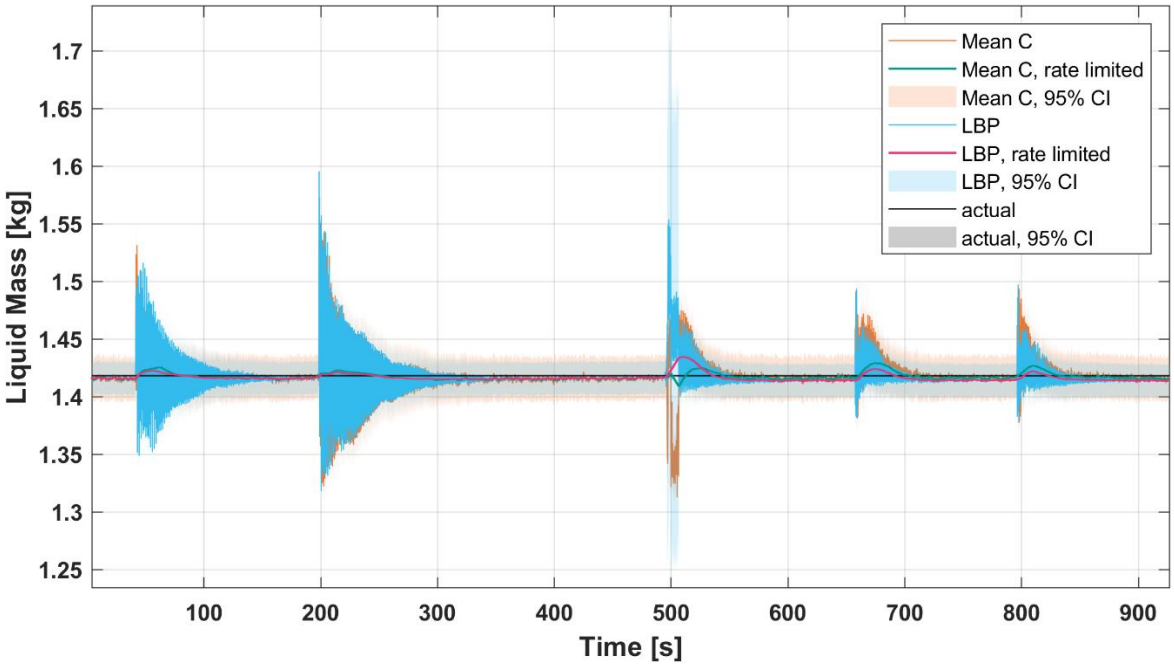

Figure 11 ECT Liquid Mass vs. Time, 30% NVF Ground Slosh Test

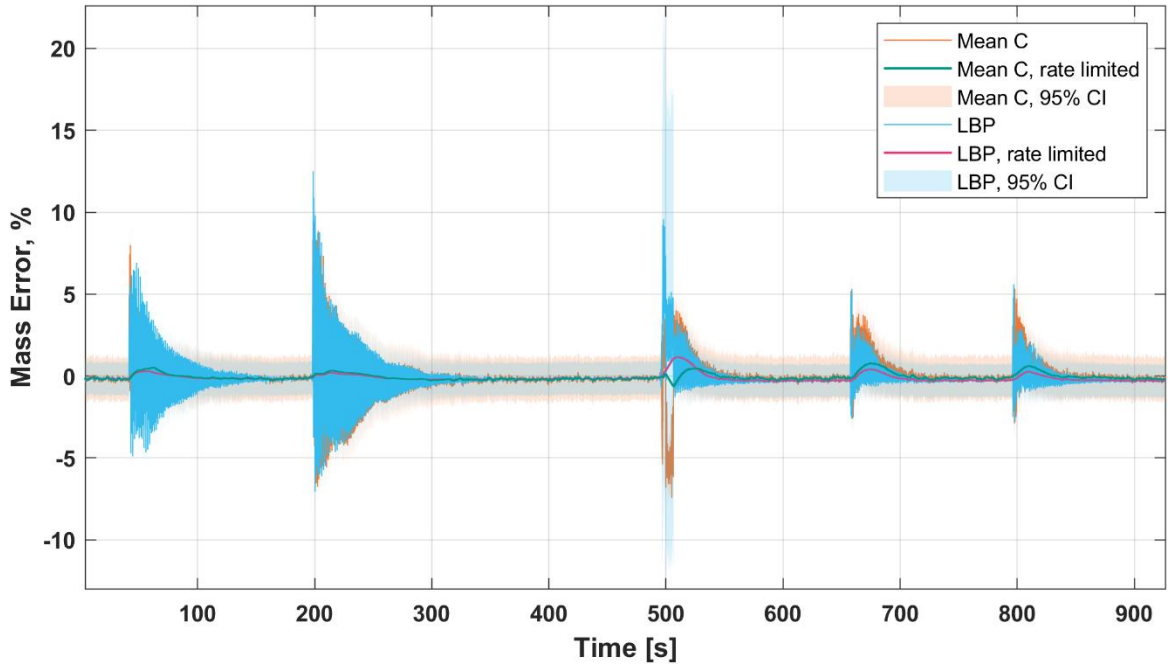

Figure 12 ECT Liquid Mass Error vs. Time, 30% NVF Ground Slosh Test

Unlike for the 5% NVF test, the liquid reorienting during the rotation in the 30% NVF test (Figure 12) resulted in a similar error range to that of the impulse sloshing.

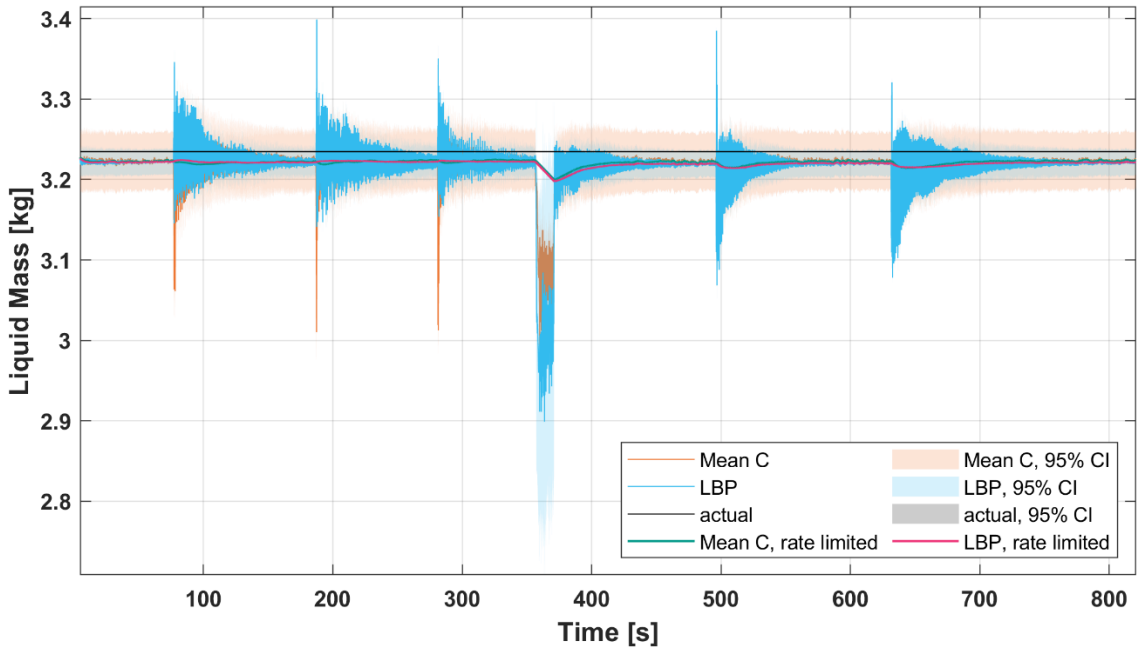

Figure 13 ECT Liquid Mass vs. Time, 70% NVF Ground Slosh Test

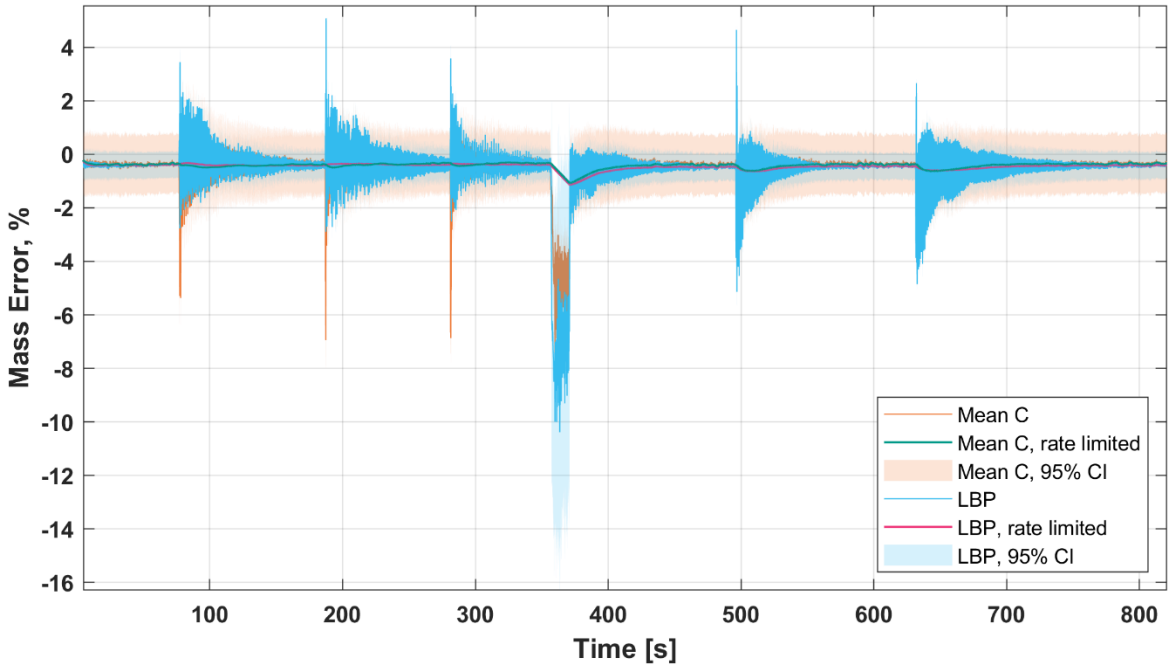

Figure 14 ECT Liquid Mass Error vs. Time, 70% NVF Ground Slosh Test

In Figure 14, the LBP curve has a larger oscillation magnitude and mostly covers the mean C data.

The following tables list the *maximum* absolute value measured liquid mass errors from all ground tests. As mentioned previously, liquid mass error is defined as $e = \frac{m_m - m_a}{m_a}$, where m_m is the ECT measured liquid mass and m_a is the actual liquid mass currently in the tank. The first column is the NVF test identifier. The “H” and “V” columns are for the horizontal and vertical

orientations, respectively, excluding the rotation between orientations. The “all” columns used all of a fill level’s data, including the unsettled rotation, and include error in both percent and grams. The “RL” columns used the rate limited filtered data. The “Full” column used all of the fill level’s rate limited data, but defined error relative to the 100% full tank liquid mass, $e_{Full} = \frac{m_m - m_a}{m_T}$, where m_T is the full tank liquid mass.

Table 4 Maximum Liquid Mass Errors, Ground Tests Mean C Method

NVF, %	H, %	RL H, %	V, %	RL V, %	all, g	all, %	RL all, g	RL all, %	RL all, %Full
5	11.2	1.5	9.7	2.7	154	62.4	18	7.1	0.4
10	9.4	0.9	7.0	0.9	166	34.3	11	2.2	0.2
20	14.2	0.8	10.9	1.4	147	14.2	15	1.4	0.3
30	9.3	0.5	5.3	0.8	132	9.3	11	0.8	0.2
40	6.3	0.4	9.8	0.7	181	10.3	15	0.9	0.3
50	4.9	0.4	8.7	0.9	283	11.8	21	0.9	0.5
60	3.8	0.5	6.9	0.4	288	10.1	23	0.8	0.5
70	6.9	0.5	3.7	0.6	247	7.6	35	1.1	0.7
80	5.3	0.2	3.7	0.4	226	6.1	18	0.5	0.4
90	4.2	0.5	1.2	0.5	227	5.4	29	0.7	0.6

Table 5 Maximum Liquid Mass Errors, Ground Tests LBP Method

NVF, %	H, %	RL H, %	V, %	RL V, %	all, g	all, %	RL all, g	RL all, %	RL all, %Full
5	18.2	1.1	33.9	2.7	282	113.9	18	7.4	0.4
10	7.4	0.5	15.7	0.6	294	60.9	13	2.7	0.3
20	19.7	1.4	5.8	0.7	204	19.7	15	1.4	0.3
30	12.5	0.3	5.6	0.4	177	12.5	16	1.2	0.4
40	7.8	0.3	12.6	1.1	221	12.6	19	1.1	0.4
50	6.0	0.3	15.3	1.0	376	15.7	24	1.0	0.5
60	4.3	0.5	8.3	0.4	408	14.3	25	0.9	0.5
70	5.1	0.4	5.1	0.6	336	10.4	37	1.1	0.8
80	4.9	0.4	4.1	0.2	365	9.9	27	0.7	0.6
90	2.5	0.5	3.8	0.5	402	9.7	33	0.8	0.7

The “all” errors were dominated by the rotation. There was not a clear trend for mass error in grams. The mass error in percent tended to increase as fill level decreased. This was due to rapidly decreasing actual liquid mass, which appears in the denominator of the percent error calculation. The unfiltered mean C method generally had lower maximum errors than unfiltered LBP. The highest filtered, oriented error was 2.7%, and this occurred during the 5% NVF test in the vertical orientation. The maximum error relative to full tank liquid mass was below 1% for all fill levels and tended to increase slightly as fill level increased due to m_a approaching m_T. These maximum mass errors give a sense of the worst-case transient error for this ECT system during slosh testing in a 1 G environment.

The previous results looked at the data in a transient manner. Since the fill level did not change during a test, all of the data points could be considered measurements of a single,

constant measurand, allowing for the calculation of measurement uncertainty. In a real tank application, this would be like averaging multiple liquid mass measurement samples, treating the variability due to liquid motion as random noise. The uncertainty interval (UI) on that mean measured mass is the ECT sensor system's accuracy for that fill level. This is different than the uncertainty propagated and displayed on the previous transient plots as a confidence interval. The fixed bias potion of the transient uncertainty is included in the mean measurement's UI, but the random uncertainty comes from the probability distribution of all of the measurements. The mass measurements are not normally distributed because the test process (periods of settled and sloshing) was not a Gaussian random process, and the resulting probability distribution was asymmetric about its mean. For each test, a nonparametric kernel distribution was fit to the probability distribution of measurements, and the inverse cumulative density function (ICDF) of that fit returned the asymmetric UI for a 95% confidence level.

Table 6 lists the actual, scale-derived volume fractions and liquid masses in the tank for each test/NVF. The uncertainty on the actual volume fraction is dominated by the uncertainty on the total tank volume. The test times represent the amount of data used for the mean and UI calculation, which was all of the data for the ground tests.

Table 6 Actual Mass, Ground Tests

NVF, %	Actual VF, %	Actual Mass, g	Test Time, s
5	5.3 +/- 0.06	247 +/- 1	297
10	10 +/- 0.11	483 +/- 1	565
20	22 +/- 0.22	1039 +/- 1	748
30	30 +/- 0.31	1418 +/- 1	923
40	38 +/- 0.38	1758 +/- 1	846
50	51 +/- 0.51	2392 +/- 1	550
60	61 +/- 0.62	2863 +/- 1	947
70	70 +/- 0.70	3235 +/- 1	816
80	79 +/- 0.79	3681 +/- 1	662
90	89 +/- 0.90	4164 +/- 1	653

Table 7 shows the mean measured masses and the UIs about the mean measured masses in different formats for each test using the mean C method results. "RL" used the rate-limited filtered results. The UI is given in grams, % of measurement, and % full scale (full tank). Table 8 is the same as Table 7 but for the LBP method. The term "time-averaged accuracy" is used to distinguish these from the "maximum transient mass errors".

Table 7 Time-Averaged Liquid Mass Gauging Accuracy, Ground Tests, Mean C Method

NVF, %	Mean Mass, g	Mean Mass UI			RL Mean Mass, g	RL Mean Mass UI		
		g	%	%Full		g	%	%Full
5	253	+132 , -14	+52 , -5.6	+2.8 , -0.3	249	+13 , -10	+5.3 , -4.0	+0.28 , -0.21
10	485	+12 , -12	+2.4 , -2.5	+0.25 , -0.26	484	+11 , -11	+2.2 , -2.2	+0.23 , -0.23
20	1045	+29 , -26	+2.8 , -2.5	+0.62 , -0.56	1045	+16 , -15	+1.5 , -1.5	+0.33 , -0.33
30	1418	+39 , -31	+2.8 , -2.2	+0.84 , -0.66	1417	+19 , -18	+1.4 , -1.3	+0.42 , -0.38
40	1757	+30 , -41	+1.7 , -2.3	+0.64 , -0.88	1758	+23 , -22	+1.3 , -1.2	+0.50 , -0.47
50	2401	+62 , -47	+2.6 , -2	+1.3 , -1.0	2402	+29 , -27	+1.2 , -1.1	+0.61 , -0.58
60	2853	+41 , -41	+1.4 , -1.4	+0.88 , -0.89	2854	+32 , -32	+1.1 , -1.1	+0.68 , -0.68
70	3219	+40 , -56	+1.2 , -1.7	+0.86 , -1.2	3221	+35 , -36	+1.1 , -1.1	+0.75 , -0.78
80	3681	+42 , -48	+1.1 , -1.3	+0.9 , -1.0	3683	+41 , -40	+1.1 , -1.1	+0.88 , -0.86
90	4146	+44 , -44	+1.1 , -1.1	+0.95 , -0.94	4148	+44 , -44	+1.1 , -1.1	+0.94 , -0.94

Table 8 Time-Averaged Liquid Mass Gauging Accuracy, Ground Tests, LBP Method

NVF, %	Mean Mass, g	Mean Mass UI			RL Mean Mass, g	RL Mean Mass UI		
		g	%	%Full		g	%	%Full
5	254	+249 , -26	+98 , -10	+5.3 , -0.56	247	+20 , -16	+8.0 , -6.5	+0.42 , -0.34
10	486	+15 , -18	+3.1 , -3.6	+0.32 , -0.38	484	+14 , -14	+2.9 , -2.9	+0.30 , -0.30
20	1044	+20 , -15	+1.9 , -1.5	+0.42 , -0.33	1043	+14 , -14	+1.4 , -1.4	+0.30 , -0.31
30	1417	+38 , -25	+2.7 , -1.7	+0.81 , -0.53	1417	+17 , -14	+1.2 , -1.0	+0.36 , -0.31
40	1761	+29 , -35	+1.7 , -2.0	+0.63 , -0.76	1761	+21 , -17	+1.2 , -0.99	+0.44 , -0.37
50	2399	+58 , -30	+2.4 , -1.2	+1.2 , -0.64	2400	+21 , -17	+0.86 , -0.69	+0.44 , -0.36
60	2852	+44 , -42	+1.5 , -1.5	+0.94 , -0.90	2853	+18 , -18	+0.62 , -0.64	+0.38 , -0.39
70	3217	+36 , -51	+1.1 , -1.6	+0.77 , -1.1	3220	+19 , -22	+0.58 , -0.69	+0.40 , -0.48
80	3669	+31 , -38	+0.83 , -1.0	+0.66 , -0.81	3672	+20 , -20	+0.54 , -0.53	+0.43 , -0.42
90	4141	+23 , -20	+0.56 , -0.5	+0.50 , -0.44	4145	+20 , -20	+0.48 , -0.48	+0.43 , -0.43

All actual masses fall within the UIs in Tables 7 and 8, meaning the various sources of uncertainty are captured adequately. The extreme positive UI limit for the 5% NVF case is due to the jump in the measurement during the rotation between orientations being significantly larger than for the other fill levels. The rate limiting filter reduces the random uncertainty component of the total uncertainty by reducing the magnitude of the slosh-induced oscillations. If the random uncertainty is already low, as it is for many fill levels over 5% VF, then using the rate limited data does little to improve accuracy. These UIs provide a sense of the time-averaged accuracy of this ECT system during slosh testing in a 1 G environment.

D. Flight Test Results

Transient plots of motion data, liquid mass, and liquid mass error are presented for one set of five low-G parabolas from the 50% NVF flight. Transient liquid mass and mass error plots are also presented for one set of five low-G parabolas from the other three flights. Figure 15 shows the 3-axis accelerations and 3-axis rotation rates measured by the IMU in the IMU axes for five parabolas during the 50% NVF flight. This is presented first to quantitatively characterize the parabolic flight motion.

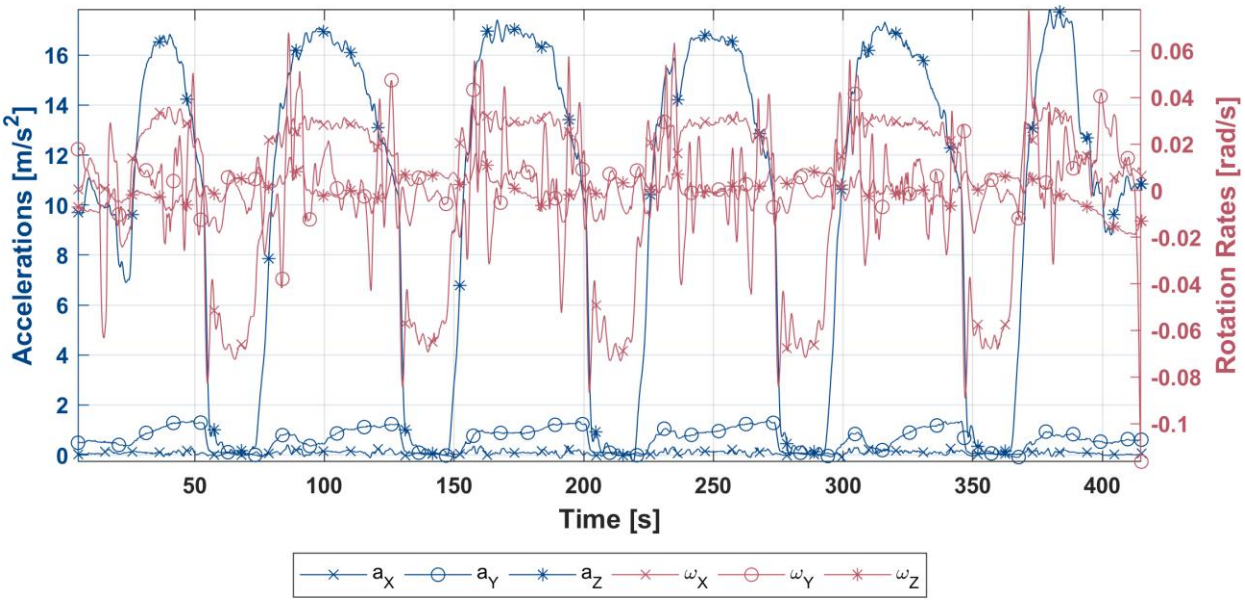

Figure 15 IMU Data, 50% NVF Flight

Refer to Figure 1 for coordinate system and experiment orientation information. The variation in a_Z from 1 G to about 1.8 G (hyper-G) to near 0 G is clearly visible. There is a small a_Y component, about 1 m/s^2 during hyper-G, associated with the aircraft pitching. This resulted in "down" not being precisely perpendicular to the aircraft deck. Lateral acceleration, a_X, is negligible. Pitch rate, ω_X, is the largest amplitude rotation rate and follows a_Z because the parabola maneuver consisted of the plane pitching up to climb (hyper-G) then pitching down to simulate free fall. Yaw rate, ω_Z, is negligible. Roll rate, ω_Y, can be significant during hyper-G and was mainly in response to atmospheric turbulence, but since the experiment was mounted near the center of the cabin, which should have been near the aircraft's roll axis, the roll rate does not show up much in the accelerations. The high (negative) roll rate at the end of this set of parabolas was the aircraft banking to line up its flight path for the next set of parabolas. As this figure shows, each parabola was unique in both timing and magnitude.

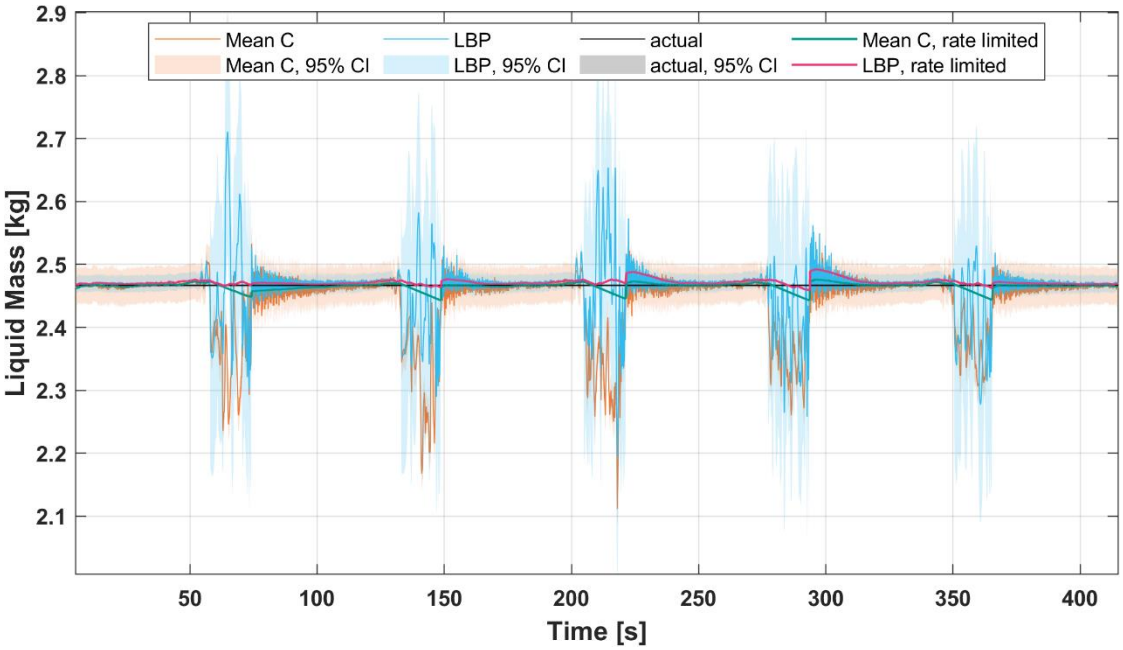

Figure 16 ECT Liquid Mass vs. Time, 50% NVF Flight Test

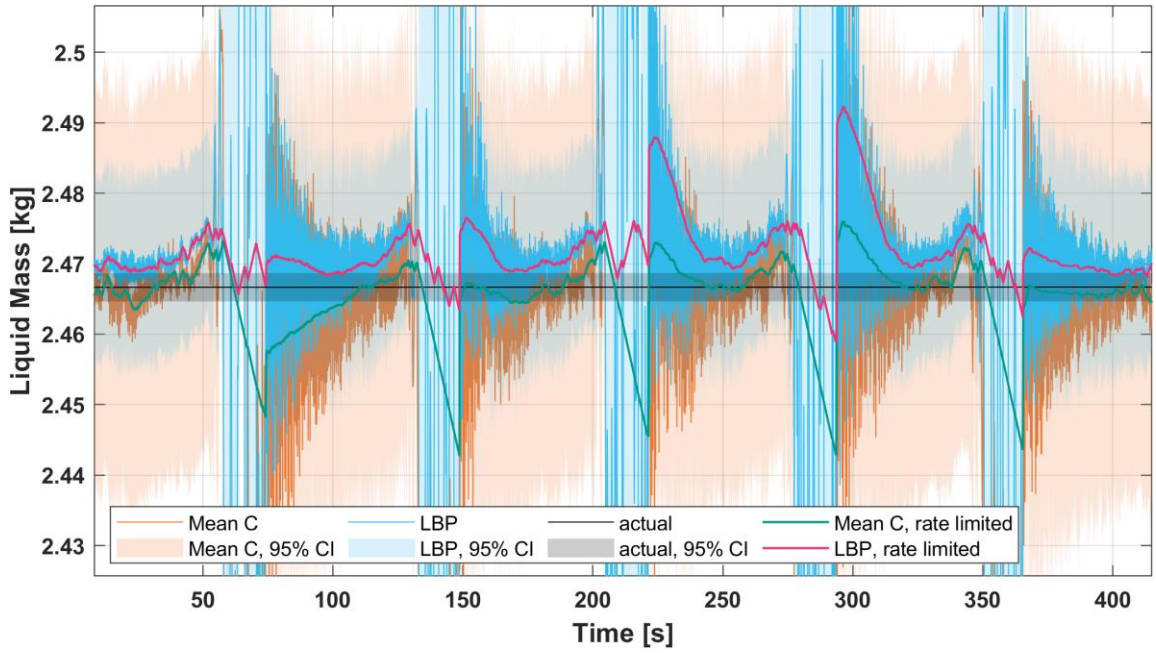

Figure 17 ECT Liquid Mass vs. Time, 50% NVF Flight Test, Zoomed in Y

Figures 16 and 17, and the following 50% NVF plots, are for the same parabolas shown in Figure 15. During settled, high-G flight, the actual liquid mass was within the corrected mean C method's and LBP's CIs, indicating good accuracy. The CI on actual mass is too small to be visible in these plots, and the CIs are not shown on the rate limited curves for plot coherence. The decay waveform after a low-G portion at the beginning of a hyper-G portion was due to the free-decay of slosh, and the primary frequency of these portions was near the theoretical first asymmetric slosh mode frequency. The remaining high frequency content during steady level flight (before 50 s in this plot) or hyper-G post-slosh-decay was due to small aircraft motions and atmospheric turbulence causing small amplitude random (not clearly first mode) slosh. The

settled liquid mass measurements appear repeatable, but low-G measurements are much more varied due to sensitivity variation (see Section IX.A). Both mean C method and LBP have up and down spikes during low-G. The rate limited curves have the higher frequency liquid motion effects, such as slosh and spikes, filtered out. The abrupt changes in the rate limited curves at the transitions from low-G to high-G are caused by the offset reset feature of the rate limiting filter (see Section VIII.C). Except during low-G, where the widening of the LBP CI is visible, the mean C method results have a wider CI than the LBP results because the uncertainty of the total tank volume is relatively high and was propagated through the total uncertainty calculation for the mean C method volume, while LBP returns a liquid volume directly (see Section VIII.D).

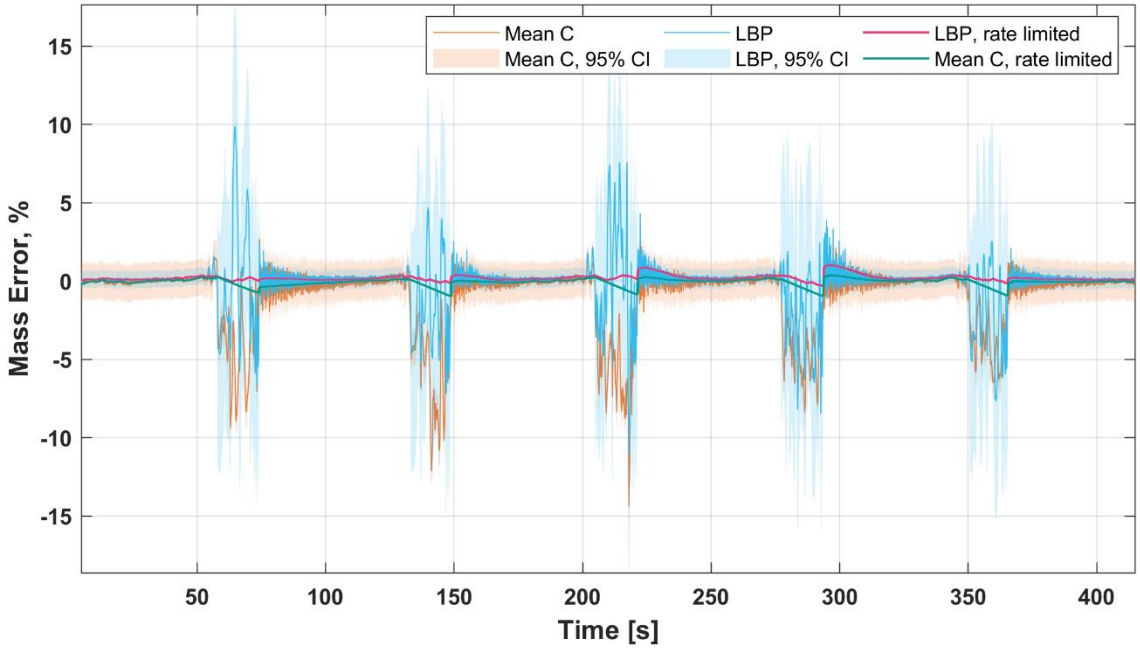

Figure 18 ECT Liquid Mass Error vs. Time, 50% NVF Flight Test

Figure 18 is the percent error calculated from the data shown in Figure 16. As mentioned previously, liquid mass error is defined relative to the actual liquid mass currently in the tank, not to a full tank. During settled, high-G flight, the corrected mean C method and LBP curves were near 0%, indicating good accuracy. The error percent during low-G varies. Filtering out the variations from liquid motion resulted in less error during low-G, effectively increasing the mass gauging system accuracy. All of the above comments for results presented in Figures 16-18 apply to other flights' results.

In Figure 17, the offset reset feature helps reduce phase delay in the rate limited mean C curve, but it does not help the rate limited LBP curve in this case. Whether or not the offset reset feature helped was case and method dependent, but it was used for all rate limited flight data curves for consistency. For the set of parabolas shown in Figure 18, the mean C method error in low-G ranges from about -14% to 4%, and the LBP method ranges from about -12% to 10%. The mean C method filtered curve ranges from about -1.0% to 0.4%, and the LBP filtered curve ranges from about -0.3% to 0.4% error during low-G and up to 1% at the transition from low-G to high-G.

Figure 19 and Figure 20 are Figure 15 and Figure 18, respectively, zoomed in on the first parabola in order to show the low-G portion in more detail.

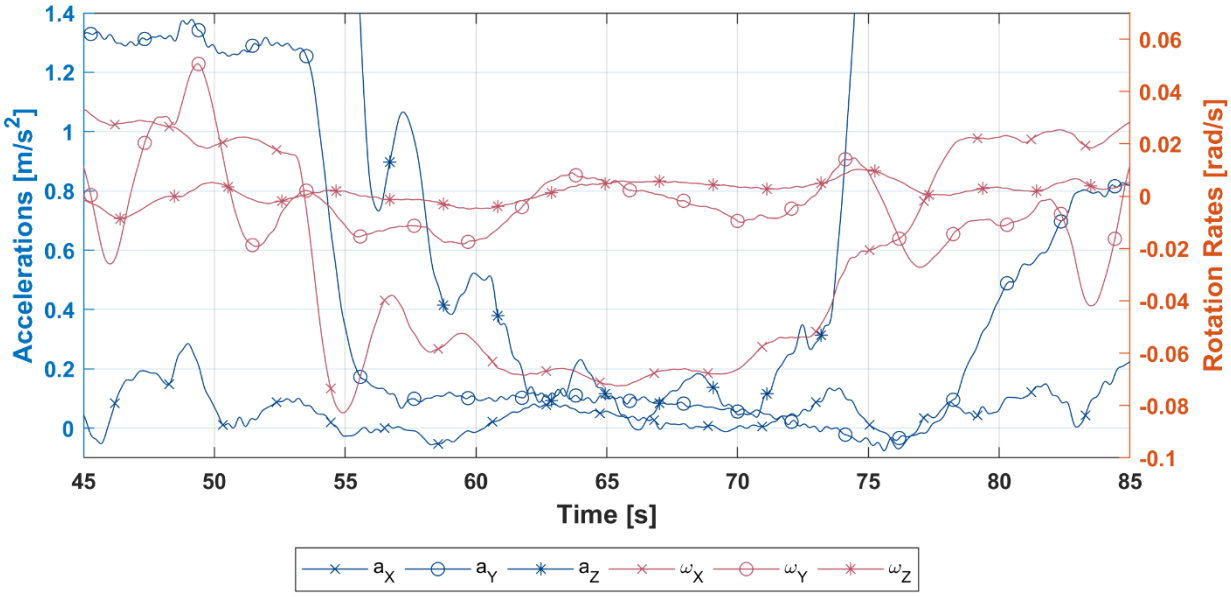

Figure 19 IMU Data, parabola 1

Every parabola was unique, but the general characteristics were similar and all included high-G, transition to low-G, small oscillations near 0 G, transition to high-G, and high-G portions. The Figure 19 acceleration y-axis is zoomed in on the low end to show the unsteadiness in a_Z during the low-G portion of the parabola. a_Z oscillates below 1 m/s^2 and hits 0 briefly. The low-G a_Z oscillations are due to the pitch rate, ω_X, oscillations as evidenced by similar relative magnitude peaks with the pitch rate leading 90 deg out of phase. The slight correlation between roll rate, ω_Y, and yaw rate, ω_Z, could be evidence of roll-yaw coupling, however, the magnitude of the yaw rate is quite low. The coupling between roll rate and lateral acceleration, a_X, is clear, and shows that the IMU origin was not on the aircraft roll axis.

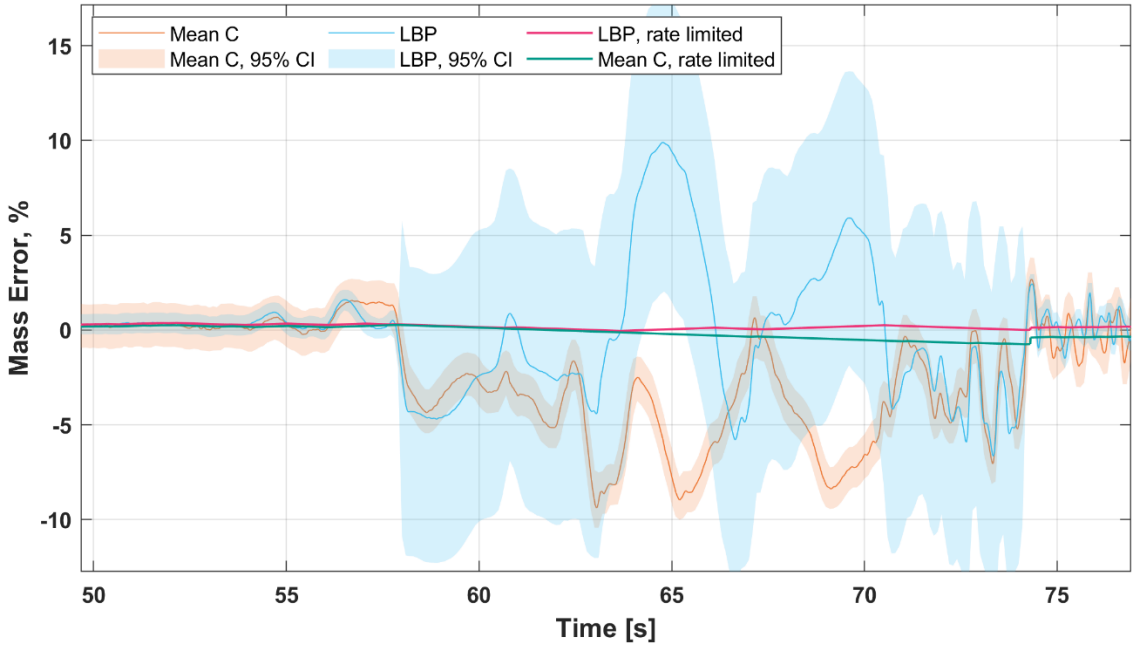

Figure 20 ECT Liquid Mass Error vs. Time, 50% NVF, 1 parabola

The oscillations during low-G generally correspond in time with the motion oscillations, but the peak magnitudes do not correspond, i.e. a large motion peak does not imply a large amplitude response in the ECT system, due to the chaotic nature of slosh and the previously discussed sensitivity variations. It is easier to compare the mean C and LBP methods in this plot. Some features are present in both curves, but they can also exhibit no correlation or anti-correlation. The limited rates of the filtered curves are visible during the large up and down spikes. The aforementioned wider LBP CI during low-G is more obvious in this plot.

Figures 21-26 are the liquid mass and mass error plots for a set of five parabolas from the 5%, 20%, and 80% NVF flights. Plots of volume fraction are included in Appendix B.

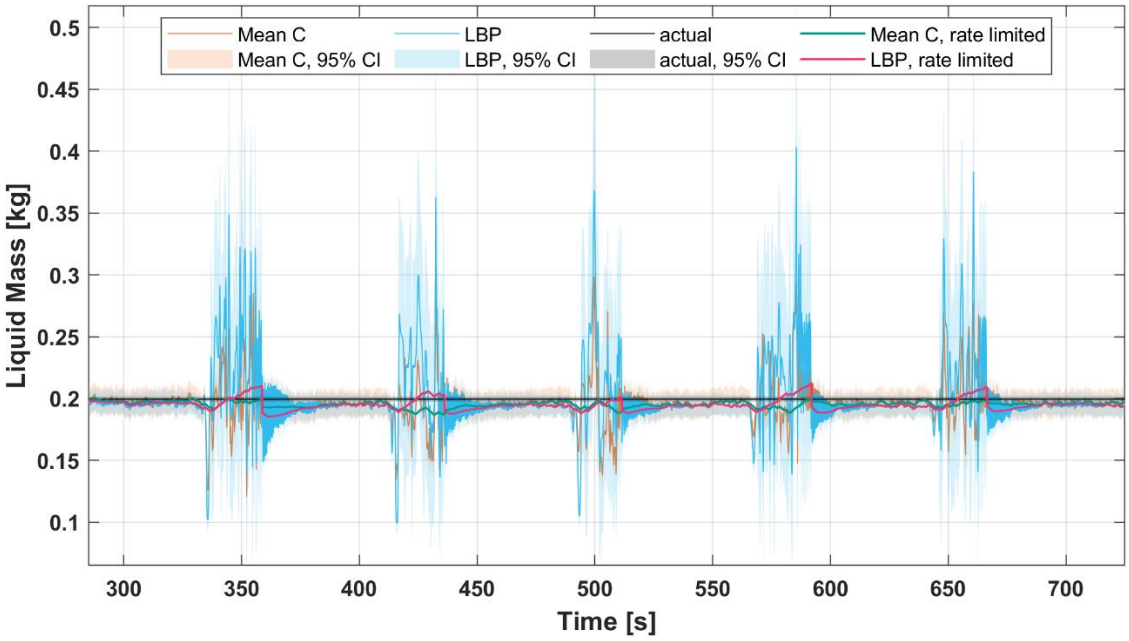

Figure 21 ECT Liquid Mass vs. Time, 5% NVF Flight Test

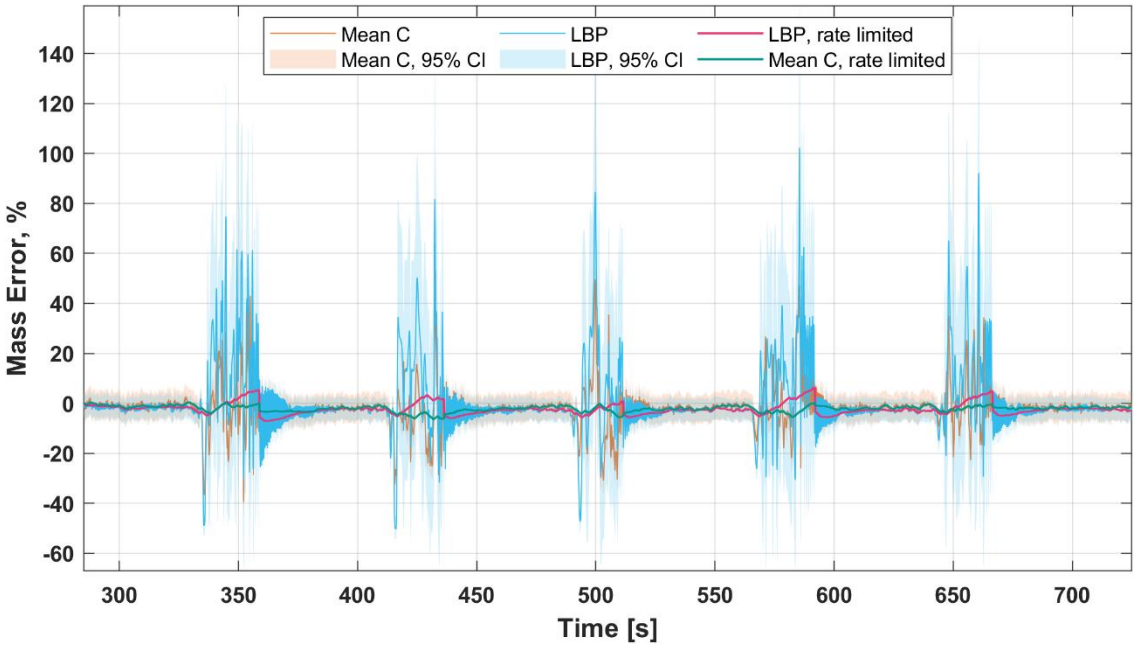

Figure 22 ECT Liquid Mass Error vs. Time, 5% NVF Flight Test

For the set of parabolas in Figure 22, the mean C method error during low-G ranges from about -40% to 53% and the LBP method ranges from about -50% to 102%. For reference, -40% error at this fill level is about 80 g, or 47 mL, about 1.7% of the total tank volume. The mean C method filtered curve ranges from about -6% to 0.4%, and the LBP filtered curve ranges from about -7% to 6% during low-G.

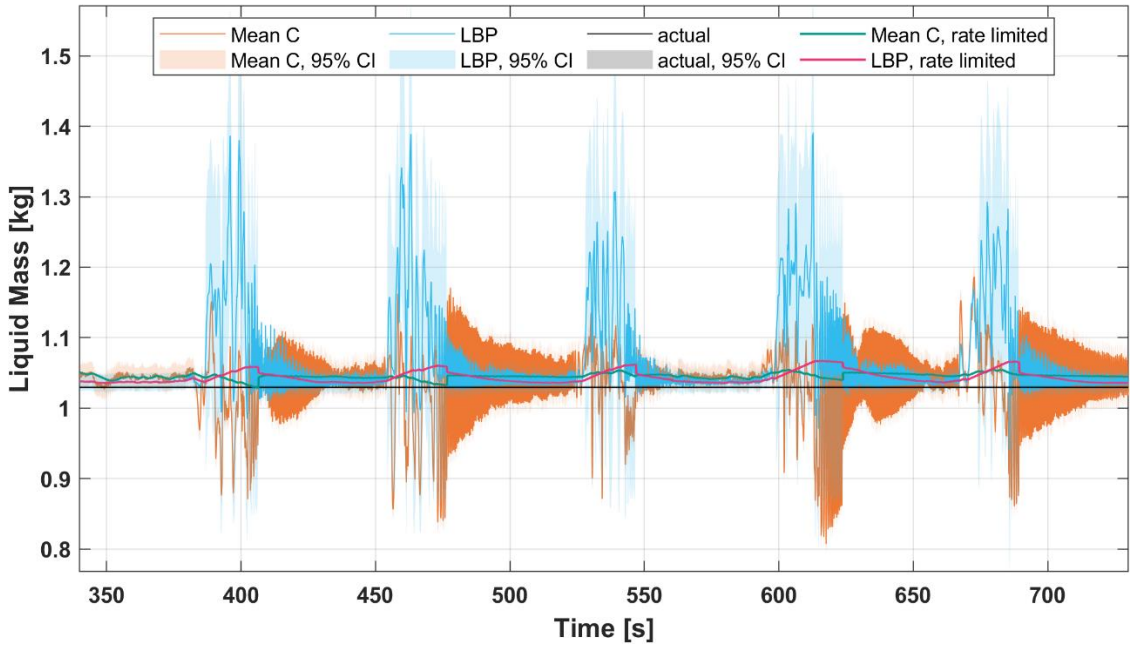

Figure 23 ECT Liquid Mass vs. Time, 20% NVF Flight Test

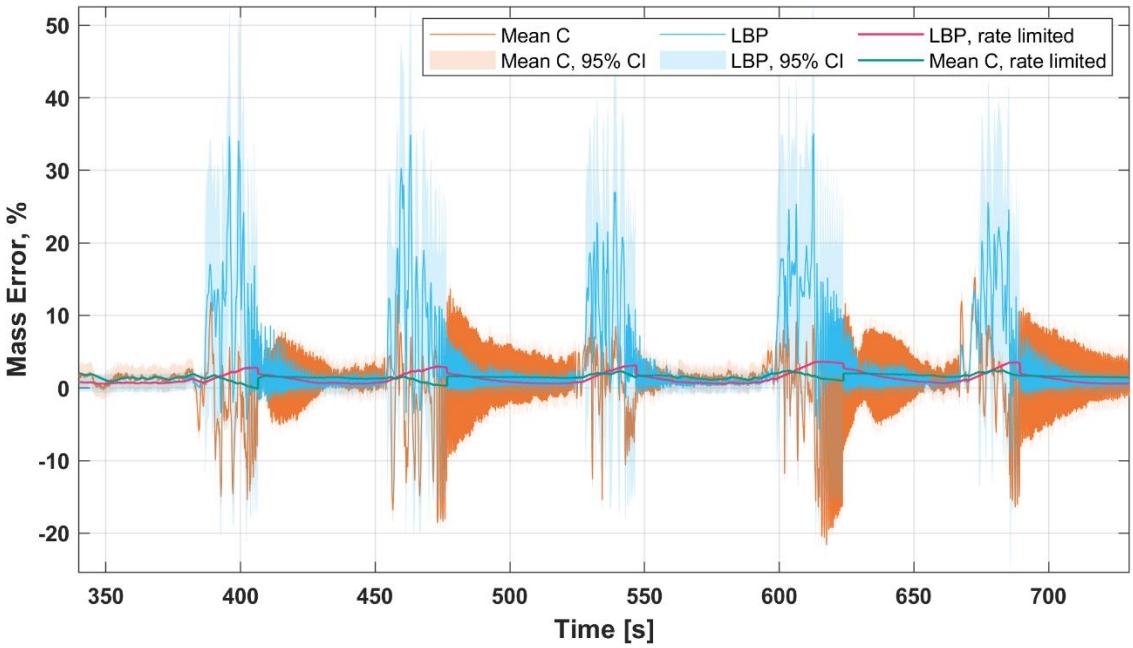

Figure 24 ECT Liquid Mass Error vs. Time, 20% NVF Flight Test

The 20% NVF fill level had the largest ECT measurement oscillations from slosh between low-G periods. Unlike the other fill levels, the mean C method calculates significantly larger slosh oscillations during hyper-G than LBP. Furthermore, if the absolute value in the mean C method is removed, the hyper-G slosh oscillation magnitudes look similar to those calculated by LBP. The large slosh wave motion for this fill level resulted in some of the primarily negative normalized capacitances' oscillations being out-of-phase with some of the other capacitances. Negative normalized capacitance occurs when a measured capacitance is less than the corresponding empty tank capacitance, which can happen when the presence of test liquid in certain regions of the tank warps the electric field in such a way as to reduce the capacitance below that of the empty tank value. The absolute value flips the negative valleys, making them positive peaks and partially in-phase, resulting in larger amplitude oscillations when all of the capacitances are averaged together compared to averaging the non-absolute-valued capacitances. The larger amplitude slosh delayed the activation of settled corrections for a few seconds into the hyper-G environment, as much as 6 s for the fourth parabola in Figure 24. For this set of parabolas, the mean C method error ranges from about -22% to 15% and the LBP method ranges from about -9% to 35%. Filtering out variation due to liquid motion results in less error during high-G and low-G sloshing, effectively increasing the mass gauging system accuracy. The mean C method filtered curve ranges from about -0.2% to 2.5%, and the LBP filtered curve ranges from about 0.5% to 3.7%. Like the 50% NVF plot (Figure 18), the mean C method low-G measurements tended to be lower than the LBP low-G measurements.

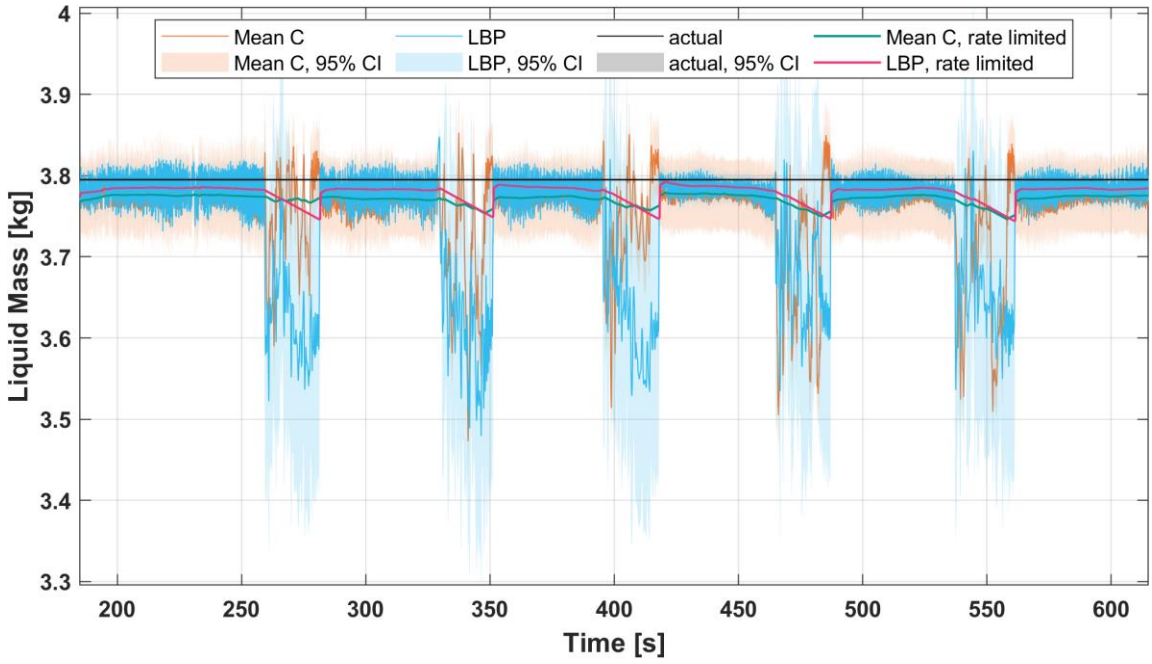

Figure 25 ECT Liquid Mass vs. Time, 80% NVF Flight Test

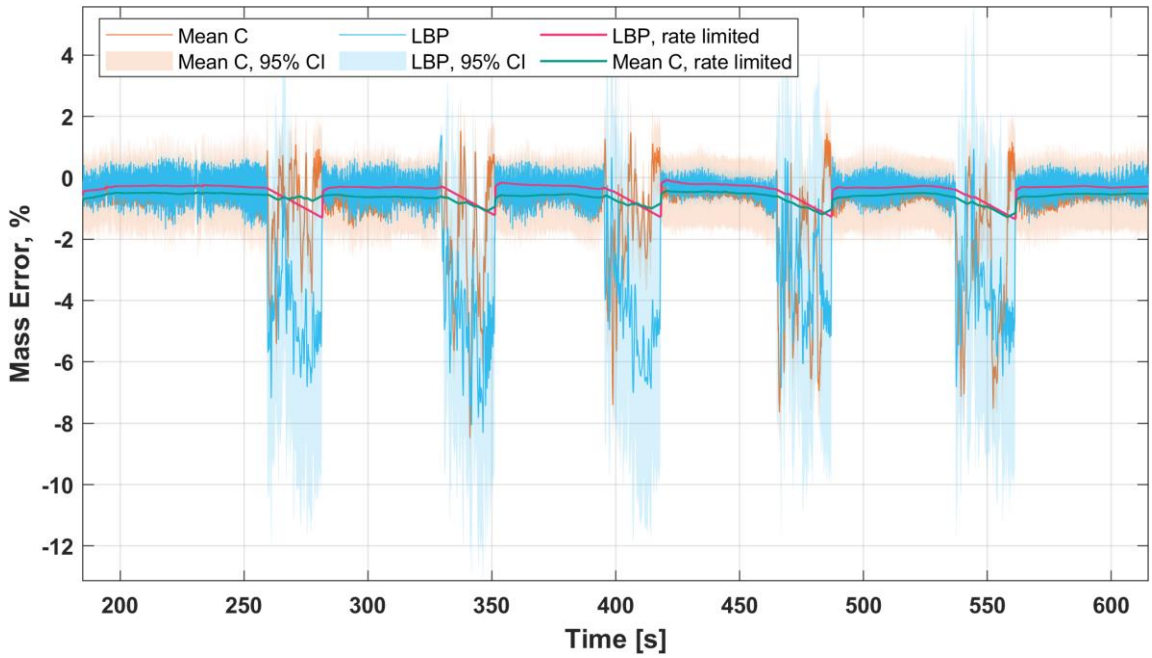

Figure 26 ECT Liquid Mass vs. Time, 80% NVF Flight Test

For the set of parabolas in Figure 26, the mean C method error during low-G ranges from about -8.5% to 1.7%, and the LBP method ranges from about -8.3% to 1.4%. The mean C method filtered curve ranges from -1.3% to -0.4%, and the LBP filtered curve ranges from about -1.3% to -0.1%. Unlike the 20% and 50% fill levels, the mean C method low-G measurements tended to be lower than the LBP low-G measurements.

The mean C method and LBP mass error CIs encompassed the 0% error line for all fill levels during the settled, hyper-G portions of the parabolas, indicating accurate settled liquid mass gauging. The variations during low-G would occasionally cause mass error to be within the measurement uncertainty of, or cross, 0% error. However, the variations swept a wide range of mass errors, so the precision of the ECT system without filtering was worse during low-G. The LBP method's low-G variations tended to span a wider range of errors than the mean C method, indicating the LBP mass measurements were less precise. Using a rate limiting filter to filter out liquid motion effects significantly reduced the variation from the steady settled value, improving the precision and accuracy of the ECT system.

Table 9 and Table 10 are the flight data equivalents of Table 4 and Table 5, respectively. The values in the first two data columns of each table are the magnitude of the largest low-G spike during that flight in grams and percent. Note that these spikes may or may not be in the presented transient plots because only five of the 25 low-G parabolas from each flight were plotted.

Table 9 Maximum Liquid Mass Errors, Flight Mean C Method

NVF, %	g	%	RL, g	RL, %	RL, %Full
5	140	70.2	25	12.3	0.5
20	239	23.2	54	5.3	1.2
50	364	14.8	76	3.1	1.6
80	327	8.6	49	1.3	1.0

Table 10 Maximum Liquid Mass Errors, Flight LBP Method

NVF, %	g	%	RL, g	RL, %	RL, %Full
5	262	131.3	58	29.1	1.2
20	362	35.2	75	7.3	1.6
50	294	11.9	118	4.8	2.5
80	346	9.1	220	5.8	4.7

The mass error in percent tended to increase as fill level decreased. This was due to rapidly decreasing actual liquid mass, which appears in the denominator of the percent error calculation. The filtered data maximum errors generally did not correspond in time with the maximum errors of the unfiltered data. Like for the ground tests, the mean C method generally had lower maximum errors than LBP. These maximum mass errors give a sense of the worst-case transient error for this ECT system during low-G flight testing.

The previous results looked at the data in a transient manner. As was described and done for Tables 7 and 8, all of the data points from a test could be considered measurements of a single, constant measurand, allowing for the calculation of a measurement mean and UI, which is the ECT sensor system's accuracy for that fill level.

Table 11 shows the actual, scale-derived volume fractions and liquid masses in the tank for each test (NVF). The uncertainty on the actual volume fraction is dominated by the uncertainty on the total tank volume. The test times represent the amount of data used for the mean and UI calculation: one set considers all data from the flights, while the other uses only the low-G portions of the flights. The 80% NVF flight had a different pilot that flew parabolas that were

more unsteady, and the flight was shorter, so the total low-G time was significantly lower than the other flights.

Table 11 Actual Mass, Flight Tests

NVF, %	Actual VF, %	Actual Mass, g	Total Test Time, s	Low-G Test Time, s
5	4.2 +/- 0.06	200 +/- 2	10080	408
20	22 +/- 0.2	1030 +/- 2	10535	346
50	53 +/- 0.5	2467 +/- 2	9890	317
80	81 +/- 0.8	3795 +/- 2	8247	254

Table 12 shows the mean measured masses and the UIs about the mean measured masses in different formats for all data from each flight test using the mean C method results. “RL” used the rate-limited filtered results. The UI is given in grams, % of measurement, and % full scale (full tank). Table 13 is the same as Table 12 but for the LBP method.

Table 12 Time-Averaged Liquid Mass Gauging Accuracy, Flight Tests Mean C Method

NVF, %	Mean Mass, g	Mean Mass UI			RL Mean Mass, g	RL Mean Mass UI		
		g	%	%Full		g	%	%Full
5	199	+19 , -14	+9.7 , -7.1	+0.41 , -0.3	199	+16 , -11	+8.1 , -5.3	+0.34 , -0.22
20	1037	+53 , -75	+5.1 , -7.2	+1.1 , -1.6	1038	+19 , -35	+1.9 , -3.4	+0.42 , -0.75
50	2455	+33 , -97	+1.3 , -3.9	+0.7 , -2.1	2460	+29 , -70	+1.2 , -2.8	+0.61 , -1.5
80	3775	+51 , -85	+1.3 , -2.3	+1.1 , -1.8	3778	+43 , -44	+1.2 , -1.2	+0.93 , -0.94

Table 13 Time-Averaged Liquid Mass Gauging Accuracy, Flight Tests LBP Method

NVF, %	Mean Mass, g	Mean Mass UI			RL Mean Mass, g	RL Mean Mass UI		
		g	%	%Full		g	%	%Full
5	199	+59 , -26	+30 , -13	+1.3 , -0.55	198	+55 , -21	+28 , -11	+1.2 , -0.45
20	1043	+96 , -16	+9.2 , -1.5	+2.0 , -0.34	1039	+30 , -11	+2.9 , -1.1	+0.64 , -0.24
50	2461	+37 , -111	+1.5 , -4.5	+0.8 , -2.4	2463	+35 , -105	+1.4 , -4.3	+0.76 , -2.2
80	3767	+69 , -199	+1.8 , -5.3	+1.5 , -4.3	3775	+60 , -159	+1.6 , -4.2	+1.3 , -3.4

Table 14 and Table 15 are the same as Table 12 and Table 13, respectively, but only use the low-G portions of the flights.

Table 14 Time-Averaged Liquid Mass Gauging Accuracy, Low-G Mean C Method

NVF, %	Mean Mass, g	Mean Mass UI			RL Mean Mass, g	RL Mean Mass UI		
		g	%	%Full		g	%	%Full
5	202	+87 , -58	+43 , -29	+1.9 , -1.2	196	+14 , -17	+7.2 , -8.5	+0.30 , -0.35
20	997	+129 , -146	+13 , -15	+2.8 , -3.1	1038	+20 , -22	+2.0 , -2.1	+0.44 , -0.47
50	2327	+142 , -149	+6.1 , -6.4	+3.0 , -3.2	2453	+30 , -30	+1.2 , -1.2	+0.64 , -0.64
80	3720	+124 , -169	+3.3 , -4.5	+2.7 , -3.6	3762	+42 , -42	+1.1 , -1.1	+0.89 , -0.89

Table 15 Time-Averaged Liquid Mass Gauging Accuracy, Low-G LBP Method

NVF, %	Mean Mass, g	Mean Mass UI			RL Mean Mass, g	RL Mean Mass UI		
		g	%	%Full		g	%	%Full
5	230	+118 , -84	+51 , -36	+2.5 , -1.8	200	+22 , -22	+11 , -11	+0.46 , -0.47
20	1143	+161 , -137	+14 , -12	+3.4 , -2.9	1053	+15 , -25	+1.4 , -2.4	+0.32 , -0.55
50	2440	+192 , -149	+7.9 , -6.1	+4.1 , -3.2	2464	+35 , -36	+1.4 , -1.4	+0.75 , -0.76
80	3639	+157 , -127	+4.3 , -3.5	+3.4 , -2.7	3766	+60 , -60	+1.6 , -1.6	+1.3 , -1.3

All actual masses fall within the UIs in Tables 12-15, meaning the various sources of uncertainty are captured adequately. One interesting result is that the UIs in the low-G-only results are more symmetric than for those computed using all of the flight data. This is because the liquid motion in the tank, and resulting ECT system measurements, during low-G was nearly a normal random process, resulting in nearly symmetric probability distributions. One of the goals of this project was to excite random liquid motion in the tank in low-G in order to characterize the ECT system's low-G performance, and the fact that these measurement probability distributions were nearly normal shows that this was achieved. The accuracy of the ECT system without the rate limiting filter was better for the full flights than the low-G portions due to the settled corrections being applied during high-G portions, which were the majority of the flight time. However, the accuracy of the ECT system with the rate limited data was similar for the full flights and low-G portions, and the LBP results were actually slightly better in the low-G case. The effect of the rate limiting filter is a reduction in random uncertainty component of the total uncertainty by reducing the magnitude of the slosh-induced variations; if the random uncertainty is already low, as it was for the 50% and 80% NVF cases using all of the flight data, then using the rate limited data does little to improve accuracy. These UIs provide a sense of the time-averaged accuracy of this ECT system in a flight-like environment.

E. Example Reconstructions

This section presents examples of ECT reconstruction of the liquid volume in the tank using LBP and LW. Reconstruction visualizations were created by exporting the reconstructed 3D permittivity distribution from specific timesteps from MATLAB and loading them into STAR-CCM+, which was used to generate 3D graphics. Percent liquid mass error in this section is defined relative to the actual mass in the tank, not a full-tank, similar to the "%" column of Table 10, but for specific time points instead of the maximum transient error. The mass errors are included so gauging accuracy comparisons can be made between LBP and LW.

A camera was not part of the experiment and would have only been marginally useful since the tank was opaque, which would have restricted the view to a (nonexistent) port. A fisheye lens would have been required to observe most of the inside of the tank from the port. Furthermore, the simulant liquid was transparent with no tint, which, coupled with image warping from the fisheye lens, would have made visual comparisons poor. Thus, reconstruction validation was done by comparing known (settled) liquid configurations with their ECT reconstructions. As discussed in Section VII, this was taken a step further by simulating the actual liquid configuration to generate simulated capacitance data, then comparing the test data reconstruction to a reconstruction of the simulation data, which were qualitatively similar to within the simulation mesh resolution. This comparison accomplished two things. First, it helped validate the electrostatic simulations. Second, it showed that the reconstruction errors that will be discussed shortly are not error in test data collection, but error from the tank geometry/design and the ECT reconstruction method.

The coordinate system in the lower left corner of the graphics below is in tank body frame. Refer to Figure 1 for more information about the experiment coordinate systems. There are two types of graphics: contour plots of permittivity on the tank YZ (X=0) cross-section, and 3D renderings of the liquid surface/volume. There are two primary viewpoints: View 1 has tank -X coming out of the page and IMU -Z is image "down", View 2 is at an angle with tank -X-Y+Z coming out of the page. The contour plots and about half of the volume renderings use View 1. The other volume renderings use View 2. Red represents gas for the contour plots, and blue represents the liquid in all figures.

Figure 27 and Figure 28 are from the 50% NVF ground test in the horizontal orientation at a time point when the liquid surface was quiescent. Figure 27 shows the reconstructed liquid volume via LBP (translucent) and surface (opaque) in blue. The green surface is the best estimate of the actual liquid surface, which was set by varying simulation fill height until liquid volume matched the actual (scale-derived) liquid volume in the tank. It is an "estimate" because there is some minor uncertainty on orientation and from the mesh resolution. To be clear, the green surface was not simulated, nor is it a reconstruction. The surfaces are isosurfaces computed with an iso-value halfway between the gas and test liquid permittivities. The small-scale roughness is due to the simulation polyhedron mesh being used for rendering; interpolating to a finer mesh for these figures would have made them look smoother, but they would not have been more accurate.

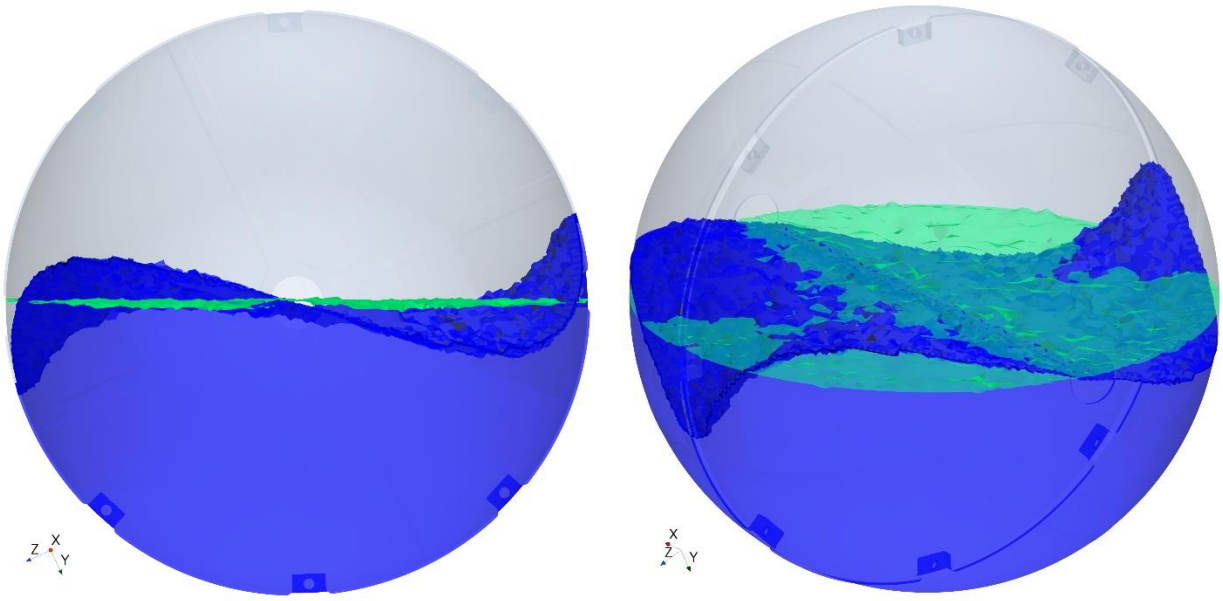

a) b)

Figure 27 LBP Liquid Volume Reconstruction from 50% NVF Ground Test: a) View 1, b) View 2 LBP reconstruction in blue, actual surface in green.

The majority of the reconstructed liquid surface is flat, though tilted slightly about X, and is warped near electrode gaps. The warping is due to many of the modeling errors discussed previously: assuming a linear solution to a nonlinear ill-posed problem, high electric field gradients near the electrode gaps, using a sensitivity matrix derived from an empty tank, the conducting tabs, unmodeled geometry, among others. The warping-near-electrode-gaps effect is present in all of the reconstructions. The warping is asymmetric because in the horizontal orientation, the tank was not in a symmetric orientation relative to the gravity vector, i.e. it was rotated about X (see Figure 1). Compared to Figure 2, the electrode gaps are difficult to see

because the tank wall had to be made more translucent in order to clearly see the liquid volume, but their locations can be inferred by examining the locations of the visible tabs in Figure 27. Warping in the vertical orientation was confirmed to be symmetric, though vertical orientation reconstructions are not presented here since they are not relevant to the flight tests. The warping results in imperfect reconstruction, which results in mass error. However, the CM and general liquid location are close to correct.

Figure 27 used LBP with a threshold halfway between the gas and liquid permittivity to make the gas-liquid interface sharp. Figure 28 shows contour plots that compare LBP and LW with and without a threshold. Figure 28b is a cross-section of Figure 27 with the same view as Figure 27a.

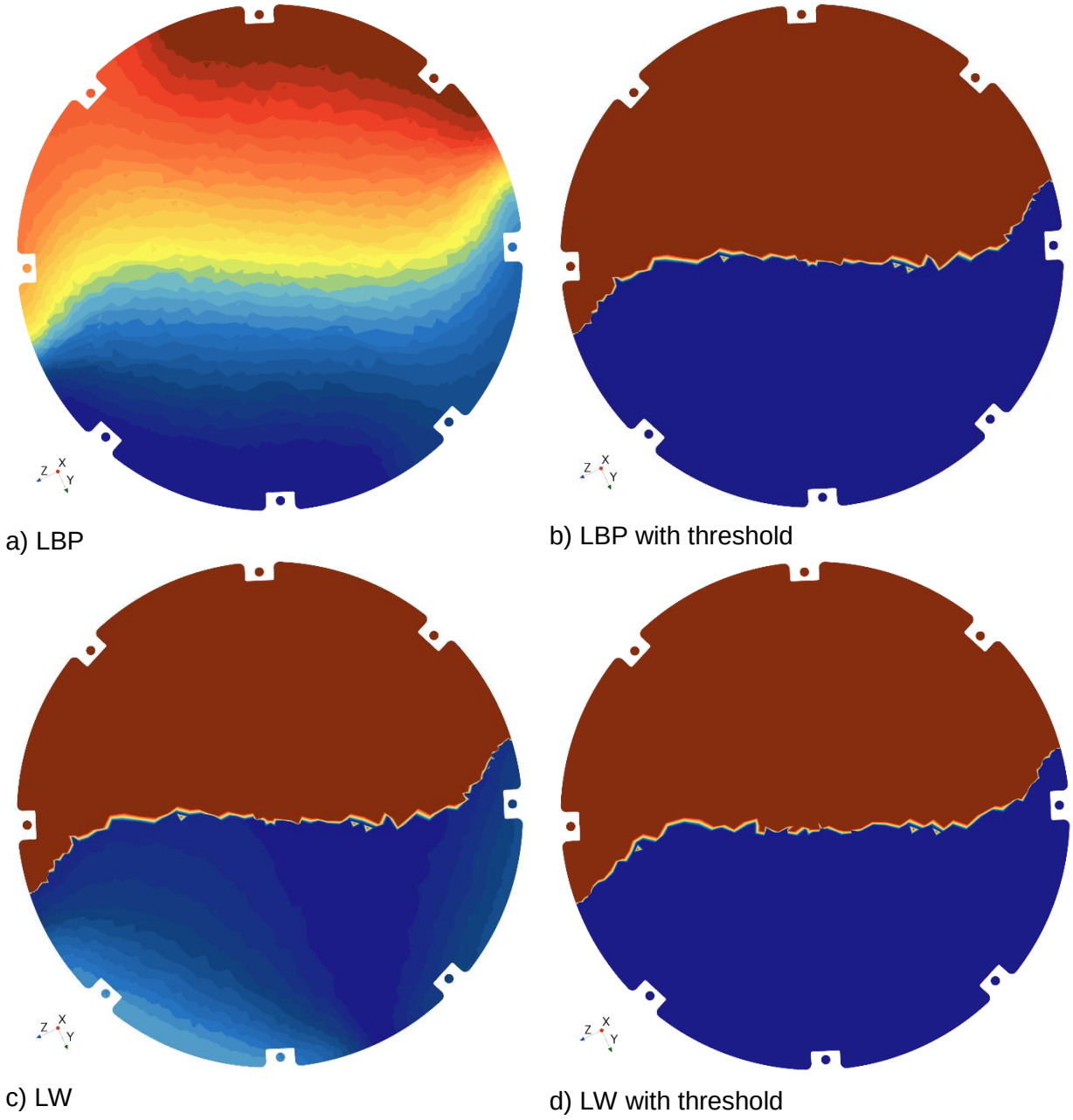

a) LBP

b) LBP with threshold

c) LW

d) LW with threshold

Figure 28 Contour Plots of 50% NVF Ground Test Reconstruction.
Gas is red, liquid is blue. Liquid mass errors: a) -4.5%, b) 5.2%, c) -8.5%, d) -4.8%

In general, LBP results in permittivity smear across most of the domain, and this characteristic is clear in Figure 28a. LW tends to sharpen the gas-liquid interface, with more iterations generally resulting in a sharper interface; some permittivity smear is still present in Figure 28c, primarily in the liquid region. LBP is used to initialize LW, which is partially why the gas-liquid interface in Figure 28b is similar to the ones in Figure 28c and d. The LW with threshold surface is slightly flatter than the LBP with threshold surface. Using a threshold can result in more or less mass error, depending on the case. Adjusting the threshold value can result in low, or even 0, mass error, but doing that arbitrarily is not recommended, and if a priori information of the “true” mass exists to guide setting the threshold value, then the need to do ECT at all is questionable.

Figures 29-31 are from the 20% NVF ground test in the horizontal orientation at a time point when the liquid surface was quiescent.

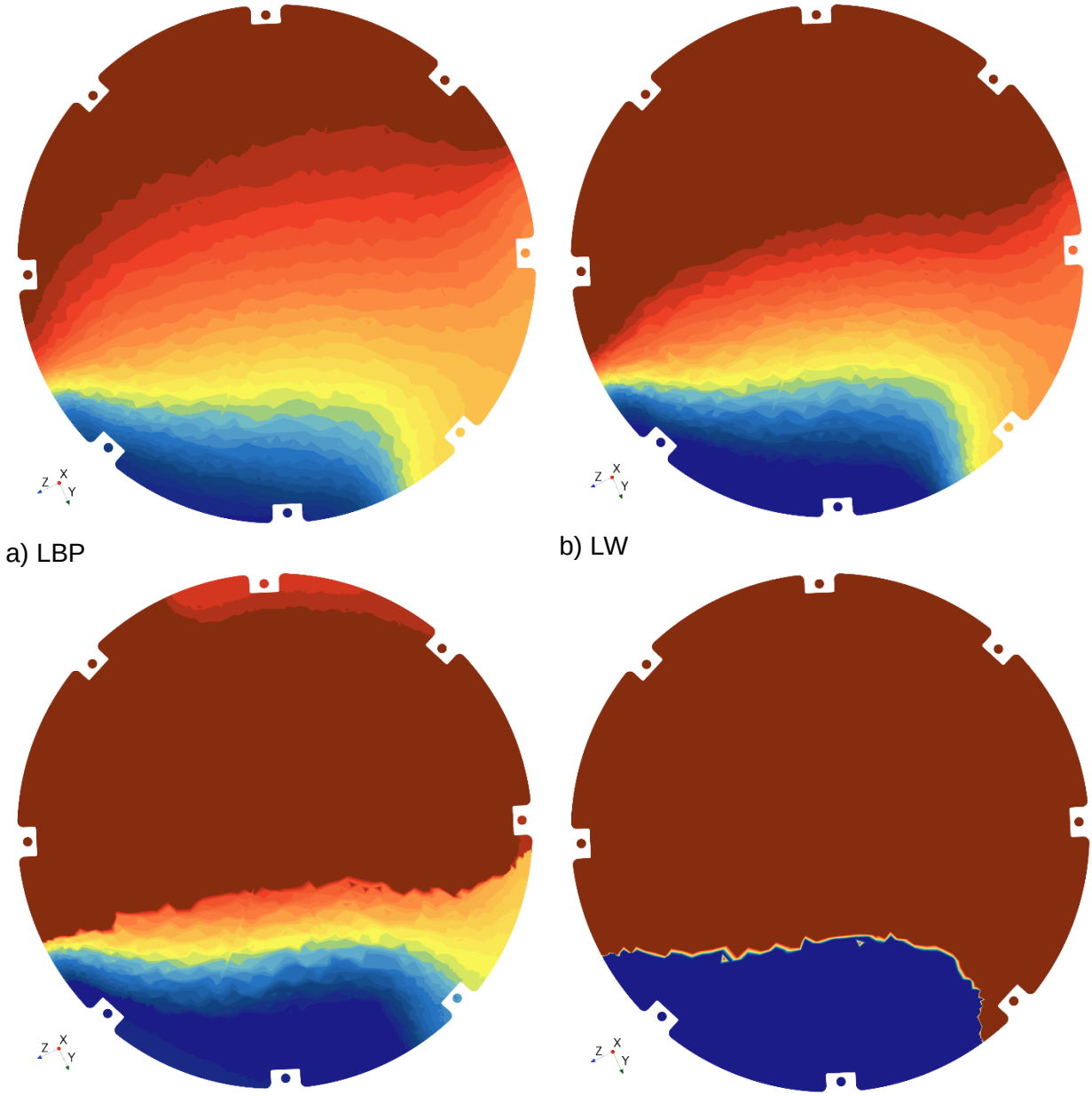

a) LBP

b) LW

c) LW with more iterations

d) LW with threshold

Figure 29 Contour Plots of 20% NVF Ground Test Reconstruction.
Gas is red, liquid is blue. Liquid mass errors: a) -7.7%, b) -8.9%, c) -18.7%, d) -24%

Figure 29a is LBP, and b-c show progressive sharpening of the gas-liquid interface with LW. Figure 29d uses a threshold halfway between the gas and liquid permittivity. The liquid mass errors are greater than those from the 50% NVF examples. Lower fill levels generally had higher % mass errors, see Table 5. Figure 30 is similar to Figure 27, but for the 20% NVF test and uses LW with threshold. The reconstructed liquid volume and surface are in blue, and the green surface represents the actual liquid surface.

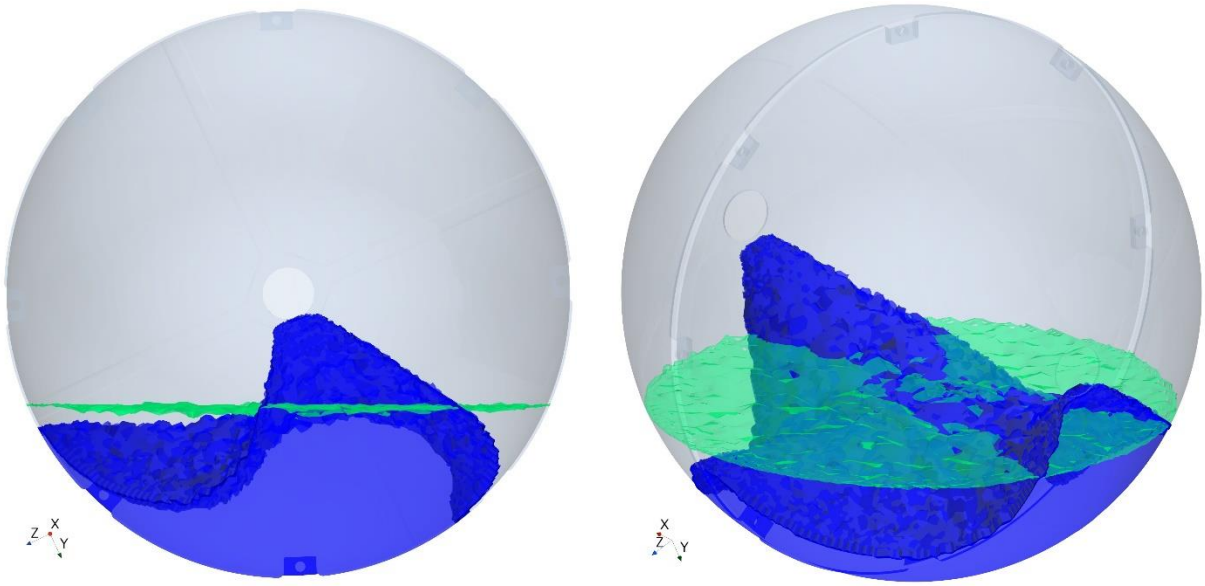

a) b)

Figure 30 LW Liquid Volume Reconstruction from 20% NVF Ground Test: a) View 1, b) View 2 LBP reconstruction in blue, actual surface in green

The warping is more extreme than what was seen in the 50% NVF reconstruction, and the negative mass error is apparent. The surface appears to be pulled up towards the gaps around the tank port holes and pulled down elsewhere. The CM and general liquid location (on bottom of tank) are close to correct despite of the warping. Unlike LBP, LW has parameters that adjust how it optimizes, e.g. number and step size of iterations, and these affect the resulting reconstruction. Furthermore, since LW is a type of steepest gradient descent, the initial condition influences which local minimum LW finds and converges towards. Figure 31 is the same case reconstructed with different LW settings.

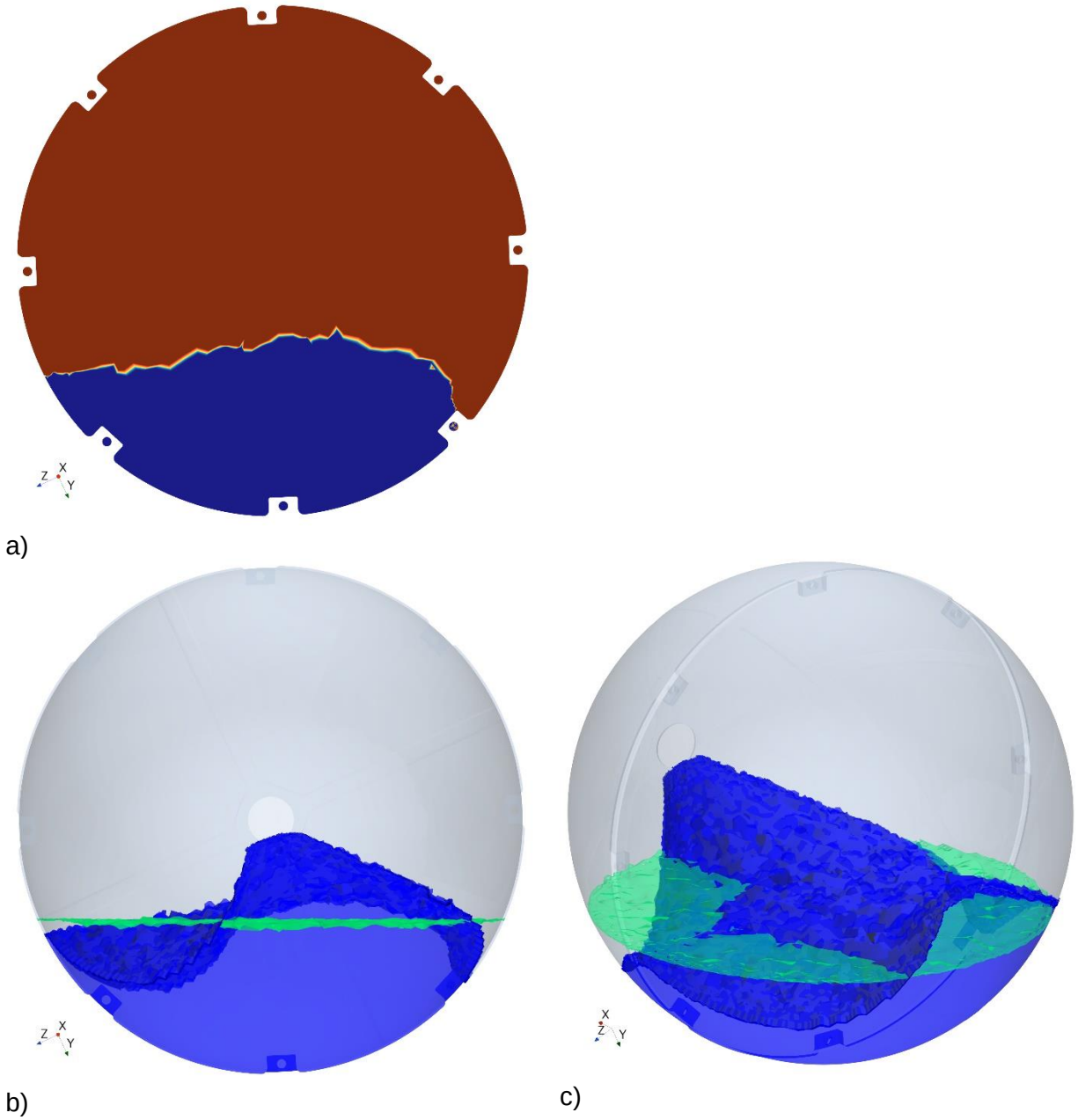

Figure 31 20% NVF Ground Test Reconstruction: a) Contour Plot, b) Volume/surface View 1, c) Volume/surface View 2

The warping is still present in Figure 31, but it is slightly flatter in the middle of the tank and has +5.8% liquid mass error instead of -24%. Adjusting LW settings involves trial and error and should be similar between cases being compared. All of the following flight test reconstruction figures used the same LW settings, similar to those used to make Figure 28d, for consistency.

Figures 33-35 are from the 50% NVF flight test at various time points before, during, and after a low-G parabola, the same low-G parabola that was plotted in Figure 19 (IMU) and Figure 20 (liquid mass error). Figure 32 is a plot of net acceleration vs. time for this parabola, with the reconstructed time points marked and labeled with their subplot letters.

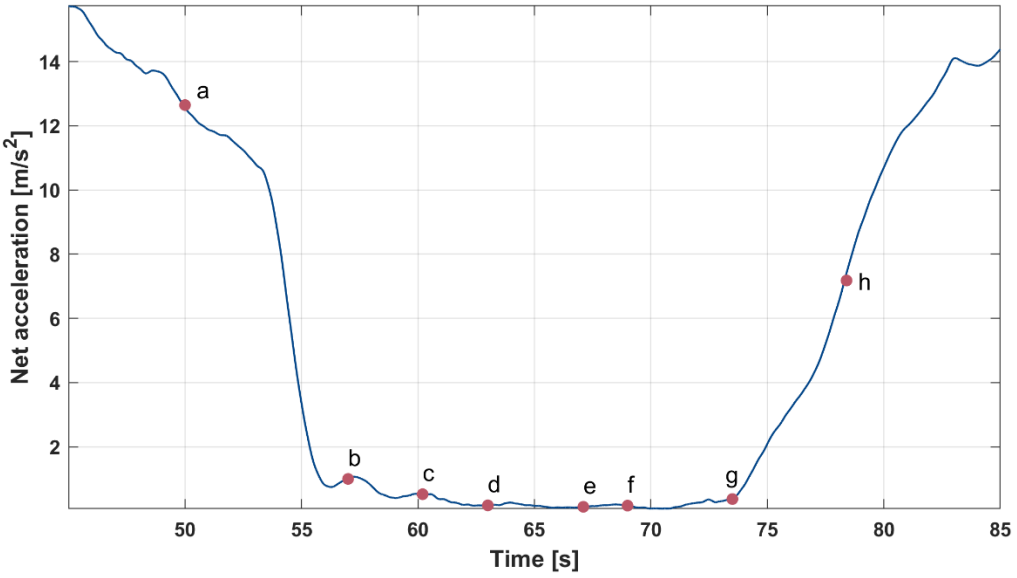

Figure 32 Acceleration at Reconstructed Time Points, 50% NVF Flight

Contour plots of permittivity are not included since the settled time points' contour plots look almost identical to Figure 28d, and 2D contour plots are not useful for 3D volume visualization for the unsettled time points. For completeness, the 50% NVF flight settled time point LBP (no threshold) reconstruction liquid mass error was -4.6%, and the LW (no threshold) one was -7.7%. Mass errors for all of the flight test time points reconstructed with LW (with threshold) are in Table 16.

Table 16 Reconstructed Time Point Liquid Mass Errors, 50% NVF Flight

Point	Error, %
a	-5.1
b	-4.9
c	-4.3
d	+7.5
e	-6.5
f	+0.8
g	-6.1
h	-5.6

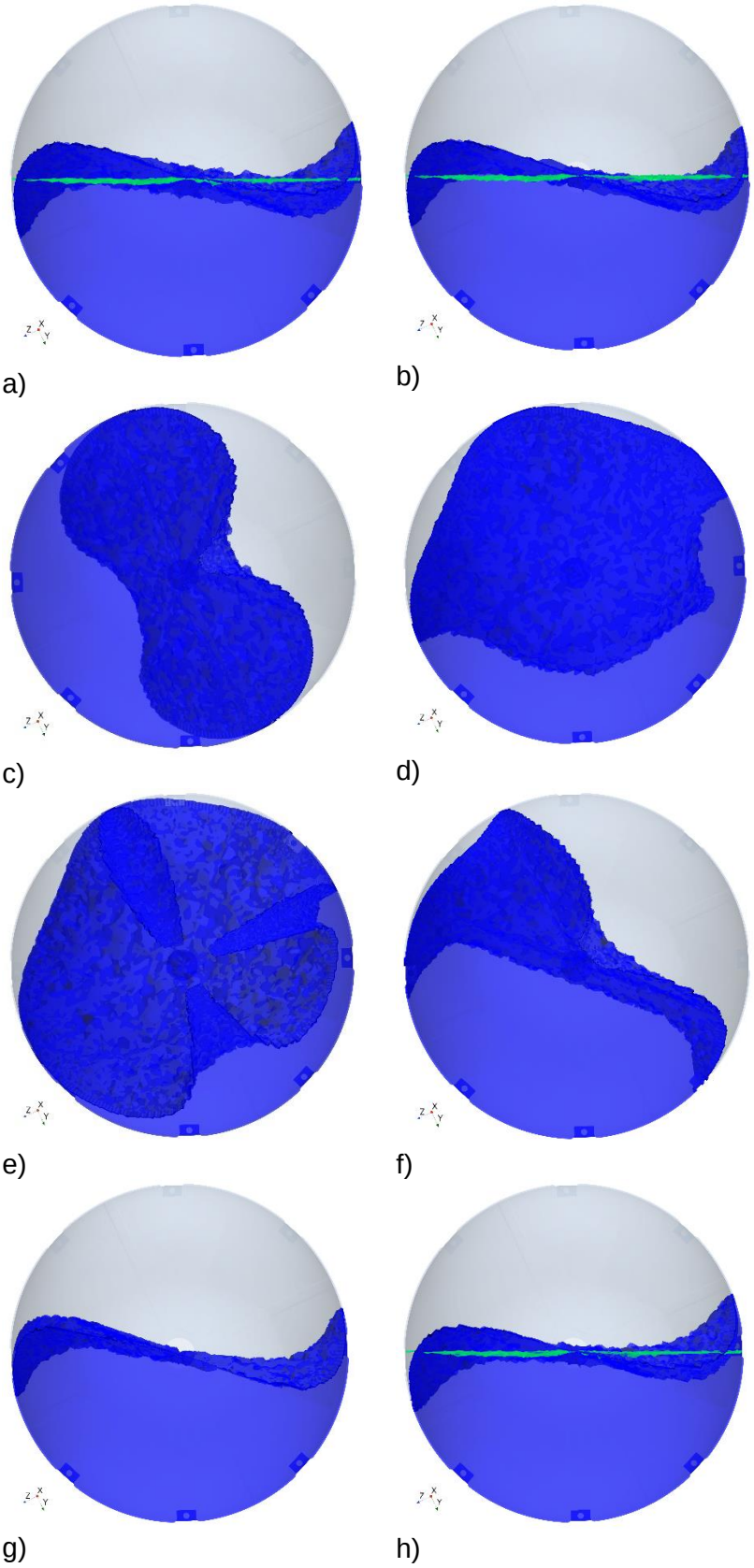

Figure 33 Reconstructed Time Points from 50% NVF Flight, View 1

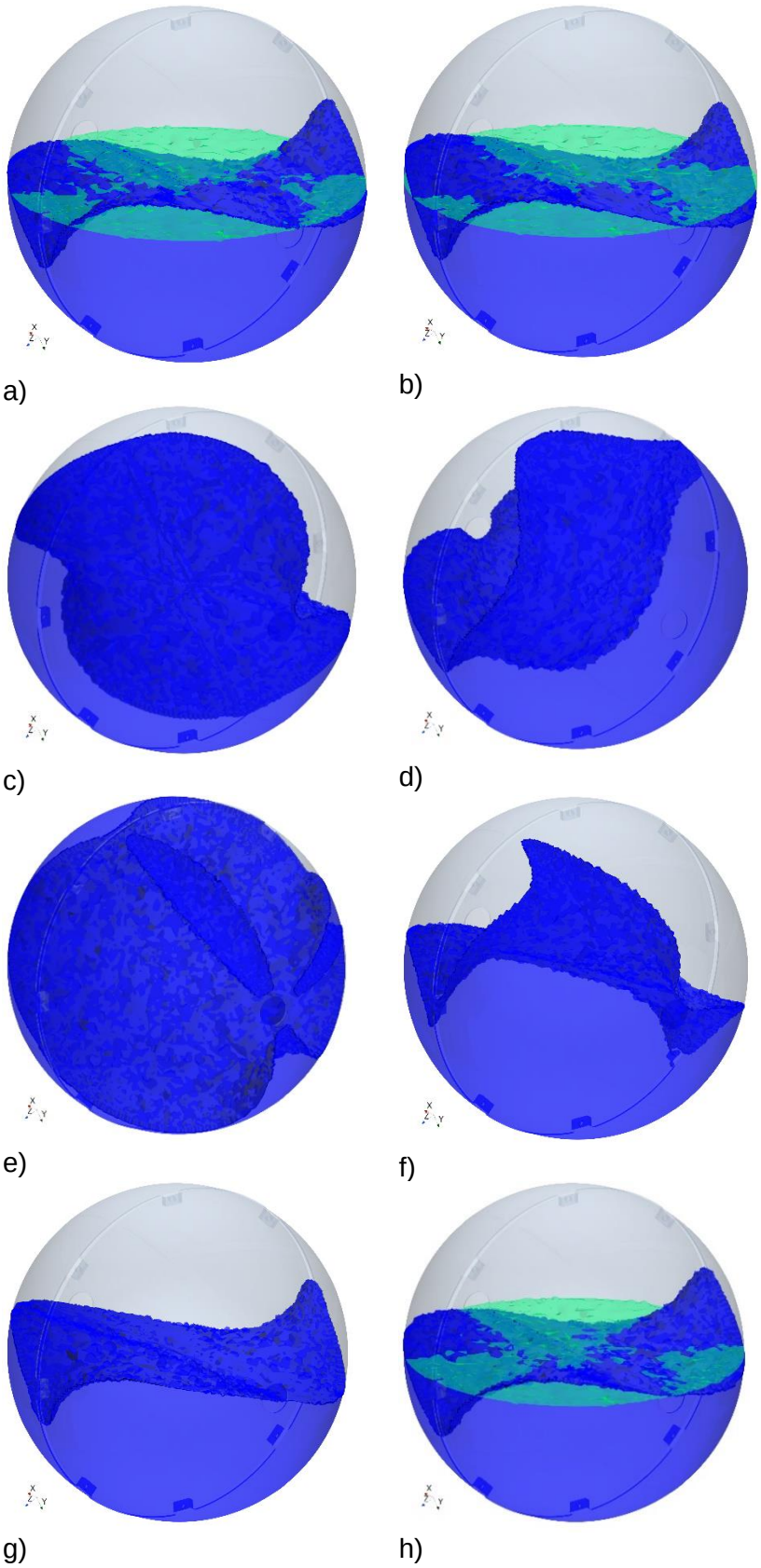

Figure 34 Reconstructed Time Points from 50% NVF Flight, View 2

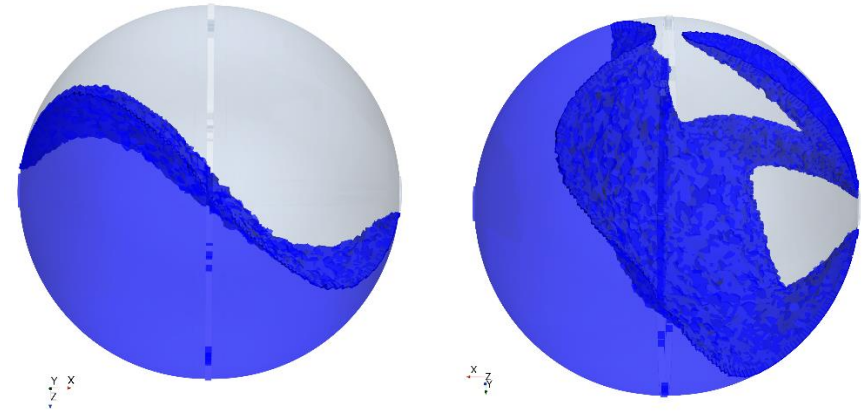

c) e)

Figure 35 Reconstructed Time Point Alternate Views:
c) tank +Y out of page, e) IMU -X out of page

Time point “a” is in hyper-G and the liquid is settled. The reconstructed volume renderings look similar to those from the 50% NVF ground test. The green surface is perpendicular to the IMU Z axis with fill level set to match the actual liquid volume in the tank. Unlike the ground test figures, this green surface is not the best estimate of the real surface because the aircraft flew at a few degrees positive angle of attack, which was visible in the IMU data as the acceleration vector having a slight IMU -Y (tank -X, aircraft aft) component. The effect of this can be seen in Figure 34a as liquid slightly above the green surface in (tank) -X and slightly below in +X, i.e. the CM also has a slight (tank) -X component. This is encouraging because it means that, even though the base solution is warped, small relative differences can be measured and supports the theory that the CM is close to correct. The net acceleration dropped to 1 m/s^2 at time point “b”. The liquid surface is tilted slightly more than at point “a”, indicating the liquid has just started to rise up the wall on the left in Figure 33b. The acceleration dropped to 0.5 m/s^2 at time point “c”. The green surface was removed since the liquid is no longer settled. The liquid is primarily on the -X+Z side of the tank, which is somewhat difficult to visualize from Views 1 and 2, which is why Figure 35c is included. There is some surface warping towards the electrode gaps around both tank ports. Based on the settled results, the real surface is likely less warped than that, though some liquid collection near the ports is expected at low Bond number. Points “d”, “e”, and “f” are near 0 g, and unsteadiness in the aircraft acceleration results in somewhat random liquid motion. The ullage bubble shifts to the opposite side of the tank between points “d” and “e”. Point “e” shows some liquid blobs remaining on the side of the tank the liquid was formerly on, and two of these blobs are detached from the bulk liquid. Figure 35e is an alternative view. Due to the slight recess of the polymer filler in the electrode gaps, and the lack of polymer in the tank split plane and around the tank ports (see Figure 2), liquid collecting in these regions at low Bond number is expected. However, the reconstructed shapes of those blobs may not be accurate due to their low volume. Point “g” is at the beginning of pull out, and “h” is approximately halfway through the transition from low-G to hyper-G. The liquid begins planar and/or rotary sloshing around point “h”, and this damps out during the time in hyper-G between this and the next parabola.

Reconstructions of other times, tests, and fill levels are not presented here for sake of brevity. Reconstructions (and mass gauging accuracy) of the 5% NVF tests are the least accurate. The 5% NVF settled reconstructions are usually blobs in an electrode gap on the bottom (direction of gravity) of the tank with no surface features indicative of the true (flat) gas-liquid interface. Thus, the volume of liquid in the 5% NVF cases is likely near or below the

volumetric/spatial resolution of this ECT system. However, that is not to say this ECT system cannot measure volumes of liquid that small; it clearly can, as was shown in Sections IX.C and D. It simply means that it cannot accurately reconstruct a 3D spatial liquid distribution, i.e. shape, of a volume near or smaller than its volumetric resolution, and this negatively affects mass gauging accuracy.

LBP is the simplest ECT method, and LW is arguably the simplest iterative ECT method. LW provided sharper gas-fluid interfaces than LBP at the expense of computational effort, and both can have thresholds applied to create binary, gas-liquid, distributions. The mass gauging accuracy of LW was similar to LBP. Despite their simplicity, and the many hardware issues discussed in Section X, these methods were able to locate liquid in the correct octant/region of the tank, get the CM close to correct, and, at least for fill levels higher than approximately 20%, reconstruct the shape of the liquid volume, granted with significant warping in the vicinity of electrode gaps. There might be ways to partially correct this warping, but it was not attempted.

X. Recommendations for ECT Hardware Improvements

The authors wish to stress the prototype nature of this ECT system: design and fabrication were inexact, and only the simplest ECT methods were implemented. The gaps between the four electrodes in each half of the tank were 6 ± 1 mm (± 17%), and the gaps between electrodes across the tank split plane were 15 ± 1 mm (± 7%). From investigating capacitance measurement imbalances (see Section VIII.A), it is clear that the electrode installation placement error contributed significantly to the overall system error. While the gap uncertainties were estimated, the actual locations of the electrodes could not be measured due to the rental contract prohibiting the tank from being opened. Some internal tank features were not disclosed by the company that built the apparatus, so these were not included in the simulation model. The accuracy of the modeled tank geometry affects the accuracy of the sensitivity matrix, so these errors in model geometry could account for the generally higher error of the LBP results compared to the mean C method results. The split plane gap contained eight aluminum tabs that projected 7 mm radially into the tank; these were extraneous features leftover from a previous iteration of the tank. Electrically conductive and grounded internal features, like these tabs, reduce the ECT system's accuracy in the vicinity of the features [10].

The gaps between the electrodes in this tank were filled with a low dielectric solid material, which prevents the liquid from interacting with some of the strong electric field that develops between electrode edge surfaces. Doing this is particularly important if the electrodes have sharp edges/corners, like the ones in this tank. Sharp electrode edges cause increased charge concentration and electric field strengthening in the tank volume near the edges, which results in larger electric field gradients and higher non-uniformity in the tank electric field, so they should be avoided in future ECT systems for this application. Spacing electrodes further from the wall helps reduce edge-to-grounded-wall interaction at the expense of higher system mass. Accurate placement of the electrodes in the tank and the simulation model are helpful in reducing uncertainty and error. While gaps between electrodes are necessary and larger gaps result in lower electric field gradients in the tank, this tank had an unnecessarily large gap around the split plane that resulted in a deadband in the settled gauging results. A trade study for size and shape of the electrodes and gaps should be done via simulation in the design phase. While not possible with this test tank, extraneous conductive features inside the tank should be avoided if they are not treated as separate electrodes. If internal features are unavoidable, which is often the case in real tanks, they should be included in the simulation model. All of these mechanical improvements would reduce the mass gauging variability

observed during sloshing and low-G by reducing the variation in sensitivity throughout the tank volume.

A previous ground based ECT slosh experiment achieved higher accuracy than this experiment for settled liquid and vigorous sloshing in 1 G [10]. That experiment had more, better fabricated, and more accurately placed electrodes, likely contributing to the higher accuracy. The tank geometry was a cylindrical section (quasi-2D) and without conducting internal features. While the specifics of the ECT methodology are not included in Ref. [10], the same company mentions using LBP in Ref. [8].

Increasing the number of electrodes would increase volumetric resolution and gauging accuracy. However, there is a limit because increasing the number of electrodes means decreasing electrode area. Every ECT system's electronics will have some noise, which limits the smallest measurable capacitance. The electrodes cannot be made so small that their capacitance is lower than the smallest measurable capacitance, i.e. below the signal to noise ratio (SNR). That said, the capacitances measured in this tank were significantly higher than the system's noise threshold, so there could (should) have been more electrodes. Like the tank, the ECT electronics package was a prototype. Electronics improvements may be able to reduce noise and increase capacitance measurement accuracy.

XI. Conclusions and Future Work

Basics of ECT theory, details of the experiment setup, data processing, and test results were presented in this paper. A large portion of post-processing effort was spent on uncertainty analysis, and the multiple definitions of accuracy have been thoroughly characterized and quantified in this project. With a target accuracy of 1% of measurement, the results indicate that this ECT sensor is not a useful gauge without additional signal processing after ECT calculations, i.e. filtering out the effects of slosh. Many types of sensors are not useful without filtering, so the inclusion of a digital filter in the ECT *system* is reasonable. If the rate limiting filter developed for this ECT system is included, then the maximum transient error (relative to actual liquid mass, not to a full tank) results indicate that this ECT system is a useful gauge for fill levels greater than 30% (greater than 10% in the horizontal orientation) in an accelerated environment (Bond number >> 100). The uncertainty of the mean mass measurement (termed "time-averaged accuracy") in an accelerated environment varied with fill level, from a maximum of about 8% (relative to actual liquid mass, not to a full-tank) at the lowest fill level to a minimum of about 0.5% at the highest fill level. In a low-G environment, this ECT system was able to achieve maximum transient errors between about 12% for the lowest fill level (5% NVF) and 1.3% for the highest fill level (80%NVF), and uncertainty of the mean mass measurements ranging from about 8.5% to 1.1%. Thus, this ECT system did not achieve the 1% target if percent was defined relative to the actual (scale-measured) liquid mass.

If the 1% target is instead full-scale, i.e. defined relative to a full tank, as is commonly done for mass gauging technologies, this ECT system in an accelerated environment was able to achieve maximum transient errors ≤ 0.8% and uncertainty of the mean mass measurements <1% for all fill levels. In a low-G environment, maximum transient errors ranged between about 0.5% and 1.6%, and uncertainty of the mean mass measurements ranged from about 0.3% to 0.9%. Thus, whether or not this ECT system achieved the 1% accuracy target is dependent on the definition of accuracy. Regardless of definition, the low-G accuracy was generally worse than that seen during the ground slosh testing, which highlights the importance of low-G, flight-like environment testing. The authors hypothesize that a significant improvement in accuracy would be achievable with the hardware improvements mentioned in Section X.

Liquid motion in the tank caused oscillations in the gauging results. Filtering out liquid motion effects significantly reduced the variations, improving the precision and accuracy of the ECT system. While the rate limiting filter is an improvement over a moving average, filtering could still be improved. In particular, the rate limits for rate limiting filters need careful adjustment to match the current physical operation, e.g. draining.

Only impulse free-decay tests were performed on the ground. Sustained excitation of planar slosh is unlikely to impact accuracy due to the success of filtering out the effects of the consistent oscillations from slosh in the pre-filtered measurements. Sustained, random, multi-axes excitation ground tests were not run and could impact accelerated environment accuracy. That said, unsteadiness during the non-parabolic (high-G) portions of the flights produced multi-axis random excitation, and the ground test results' error bounded the error during those portions of the flights. The quoted accuracy numbers are for a tank with a constant fill level. Filling and draining could negatively affect accuracy and should be tested both on the ground and in low-G. Each low-G portion of a parabola only lasted for approximately 18 s. If an ECT system is used in a tank experiencing longer periods of microgravity, filtering (with any type of filter) out the liquid motion effects on the ECT gauging results might be less successful, resulting in more gauging error. On the other hand, heavier filtering, such as lower rate limits in a rate limiting filter, could be used because the propellant drain rate would be zero or near zero for cryogens (boil-off). This would be like using a rate limit lower than the "medium" rate limit used for this study's ECT system. Additionally, extended periods of microgravity will be steadier than the low-G environment of the parabolic flights, resulting in less liquid motion. Since the liquid motion in the tank drives the gauging variations, which drive the gauging error, the long-term accuracy depends heavily on where and how much the bulk liquid moves. While some practical implementation details, mechanical design suggestions, and examples were discussed, an in-depth analysis of specific applications of ECT systems to flight tanks is beyond the scope of this paper.

The settled calibration/corrections were only useful when the liquid was settled near the orientation for which they were derived. The lack of unsettled, microgravity corrections is a major challenge for ECT mass gauging. Testing at a finer fill level resolution could improve the settled corrections, but more accurate settled corrections will not significantly reduce uncertainty. Three of the largest system uncertainties were the total tank volume uncertainty (for the mean C method only) driven by uncertainty of the as-built geometry, LBP process random uncertainty (LBP only), and the normalized capacitance uncertainty, which was composed of many propagated uncertainties. Preemptively addressing uncertainty in future ECT test programs would be worthwhile to ensure success.

While it is not clear from these results which method, mean C or LBP, is better for mass gauging, it is clear that more accurate reconstruction methods could improve the ECT system accuracy, particularly for 3D reconstruction. To be useful in an ECT measurement subsystem of a flight controller, the ECT algorithm must have a low enough computational cost to be implemented in real-time. The real-time requirement could be relaxed if low-rate gauging measurements are acceptable. Since mechanical improvements are straightforward to implement, and previous works demonstrated functionality with cryogens, the authors are focusing current research efforts on implementing more advanced ECT methods and future efforts on ECT algorithm development.

The results of this project indicate that ECT is a viable solution to the microgravity propellant mass gauging technology gap. ECT can provide measurements of the 3D distribution of the liquid in the tank in real time. The ability to directly and quantitatively compare test and simulated 3D fluid distributions could be a major advancement in CFD slosh validation, and this

is also a current research topic for the authors. The liquid velocity field can be computed by comparing (differencing) consecutive 3D liquid distributions, which can then be used to calculate the slosh forces and torques. Thus, ECT is mass gauging technology with the potential to replace mechanical slosh analogs in GN&C systems with what is effectively a sensor measurement, which would be a major advancement in GN&C of liquid fueled space vehicles. The authors believe these potential advantages make ECT a critical emerging technology worth further study and investment by NASA and the space industry.

The raw experimental data from this study is publicly available through the NASA Technical Report Server (NTRS) entry number 20220014348.

References

[1] F. T. Dodge, "Propellant mass gauging: Database of vehicle applications and research and development studies, NASA/CR-2008-215281," SwRI, 2008.

[2] K. M. Crosby, N. J. Williams, R. J. Werlink and E. A. Hurlbert, "Modal Propellant Gauging: High-resolution and non-invasive gauging of both settled and unsettled liquids in reduced gravity," *Acta Astronautica,* vol. 159, pp. 499-507, 2019.

[3] G. Zimmerili, M. Asipauskas, J. Wagner and J. Follo, "Propellant Quantity Gauging Using the Radio Frequency Mass Gauge," in *49th AIAA Aerospace Sciences Meeting*, Orlando, FL, 2011.

[4] J. D. Jackson, Classical electrodynamics, New York, NY: Wiley, 1999.

[5] Trans-sonics, "Capacitance Propellant Gaging Study for Orbiting Spacecraft, CR-87496," [Online]. Available: https://ntrs.nasa.gov/citations/19670025277.

[6] M. A. Nurge, "Electrical capacitance volume tomography with high contrast dielectrics using a cuboid sensor geometry," *Meas. Sci. Technol.,* vol. 18, no. 1551, 2007.

[7] M. Deshpande, "Fuel Mass Gauging Based on Electrical Capacitance Volumatric Tomography Techniques," NASA Flight Opportunities, [Online]. Available: https://flightopportunities.ndc.nasa.gov/technologies/39/. [Accessed 27 4 2023].

[8] A. Hunt, R. Foster-Turner and R. Drury, "Propellant Slosh Force and Mass Measurement," *Hindawi International Journal of Aerospace Engineering,* vol. 2018, 2018.

[9] S. H. Yang, Y. S. Kim, N. G. Dagalakis and Y. Wang, "Flexible Assemblies of Electrocapacitive Volume Tomographic Sensors for Gauging Fuel of Spacecraft," *Journal of Spacecraft and Rockets,* vol. 58, no. 2, pp. 499-504, 2020.

[10] P. Behruzi, A. Hunt and R. Foster-Turner, "Evaluation of liquid sloshing using Electrical Capacitance Tomography," in *AIAA Propulsion and Energy Forum*, Virtual, 2020.

[11] P. Behruzi, A. Hunt, R. Foster-Turner and A. Fischer, "Testing an Electrical Capacitance Tomography sensor in liquid hydrogen," in *AIAA SciTech Forum*, National Harbor, MD, 2023.

[12] C. Biagi, M. Nurge, R. Youngquist, J. M. Storey, L. Bird, A. Atkins, A. Swanger, N. Spangler, M. Mercado, J. Defiebre, A. Esparza and J. Hartwig, "Capacitive Mass Gauging for Fluids in Micro-g (CAPMAG)," in *30th Space Cryogenics Workshop*, Kailua-Kona, Hawaii, 2023.

[13] W. Q. Yang and L. Peng, "Image reconstruction algorithms for electrical capacitance tomography," *Measurement Science and Technology,* vol. 14, pp. R1-R13, 2003.

[14] R. Youngquist, J. Storey, M. Nurge and C. Biagi, "A Derivation of the Electrical Capacitance Tomography Sensitivity Matrix," *Measurment Science and Technology,* vol. 34, no. 025404, 2023.

[15] C. G. Xie, S. M. Huang, B. S. Hoyle, R. Thorn, C. Lenn, D. Snowden and M. S. Beck, "Electrical capacitance tomography for flow imaging: system model for development of image reconstruction algorithms and design of primary sensors," *IEE Proceedings G,* vol. 139, no. 1, pp. 89-98, February 1992.

[16] C. Gunes, Q. M. Marashdeh and F. L. Teixeira, "A Comparison Between Electrical Capacitance Tomography and Displacement-Current Phase Tomography," *IEEE Sensors Journal,* vol. 17, no. 24, pp. 8037-8046, 2017.

[17] 3M, *3M Fluorinert Electronic Liquid FC-72 Technical Datasheet,* 2019.

[18] Analog Devices, *ADIS16460 Data Sheet,* 2019.

[19] Siemens, "STAR-CCM+ 2021.1," 2021.

[20] Mathworks, "MATLAB R2021a," 2021.

Appendix A. Additional Ground Test Plots

5% NVF (mass and mass error plots shown in body text)

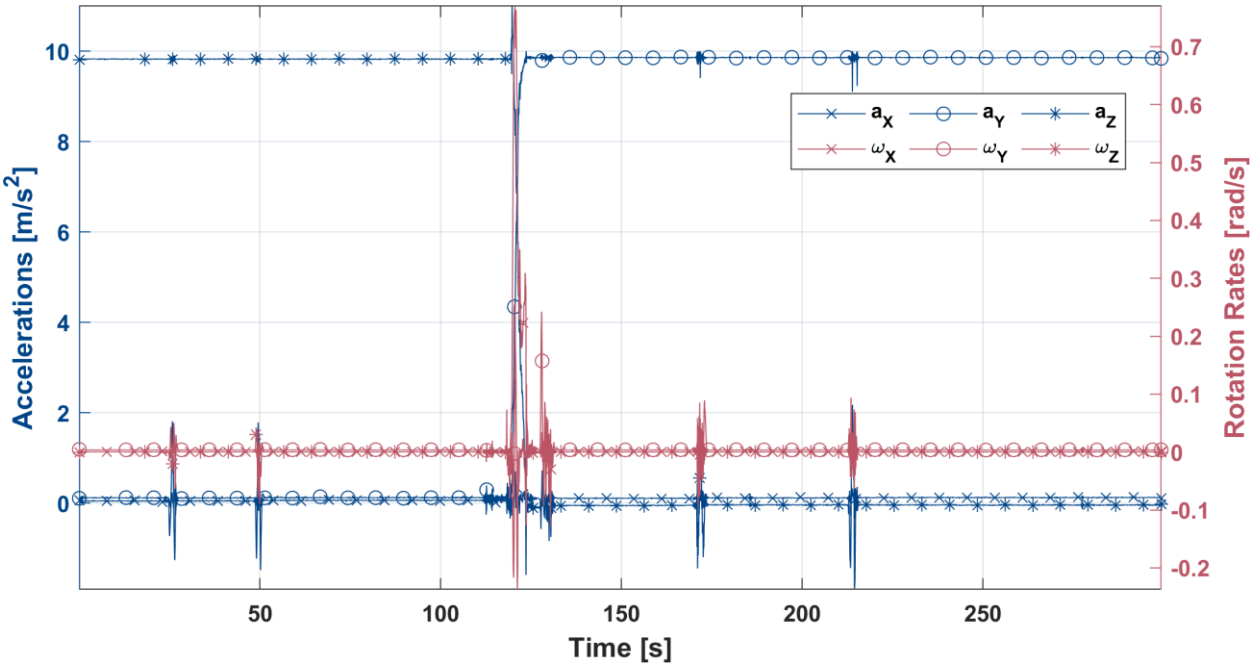

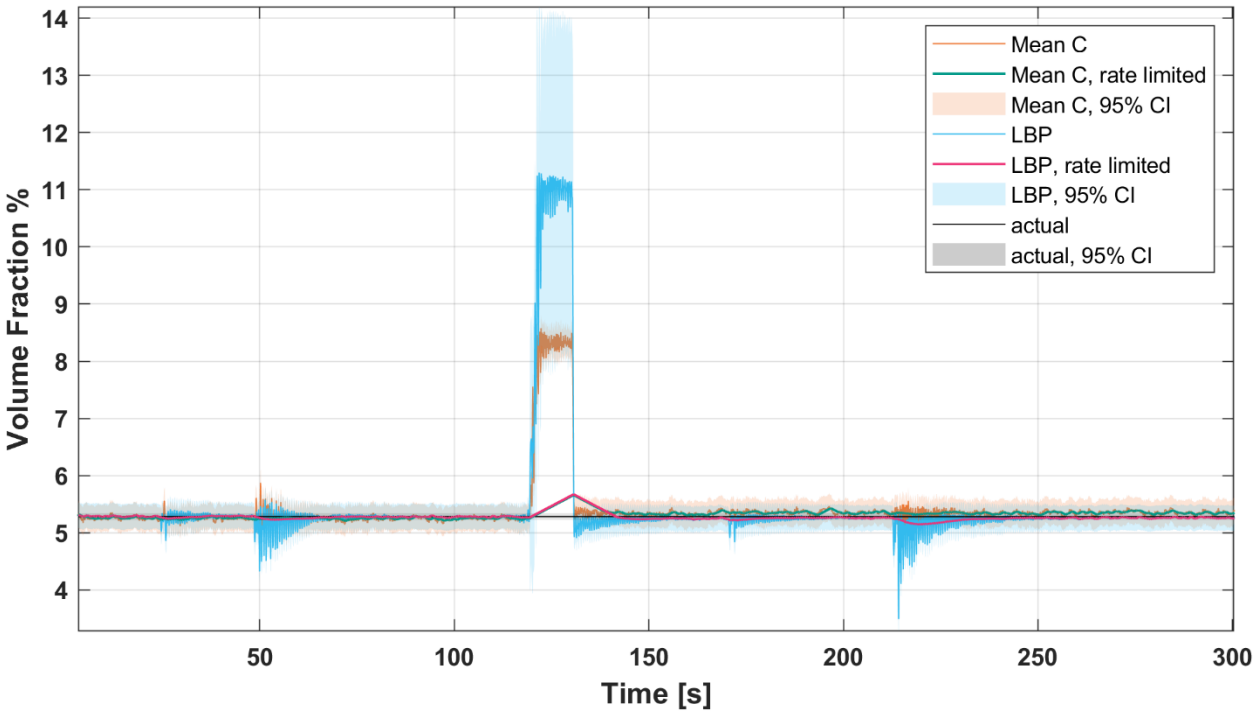

10% NVF

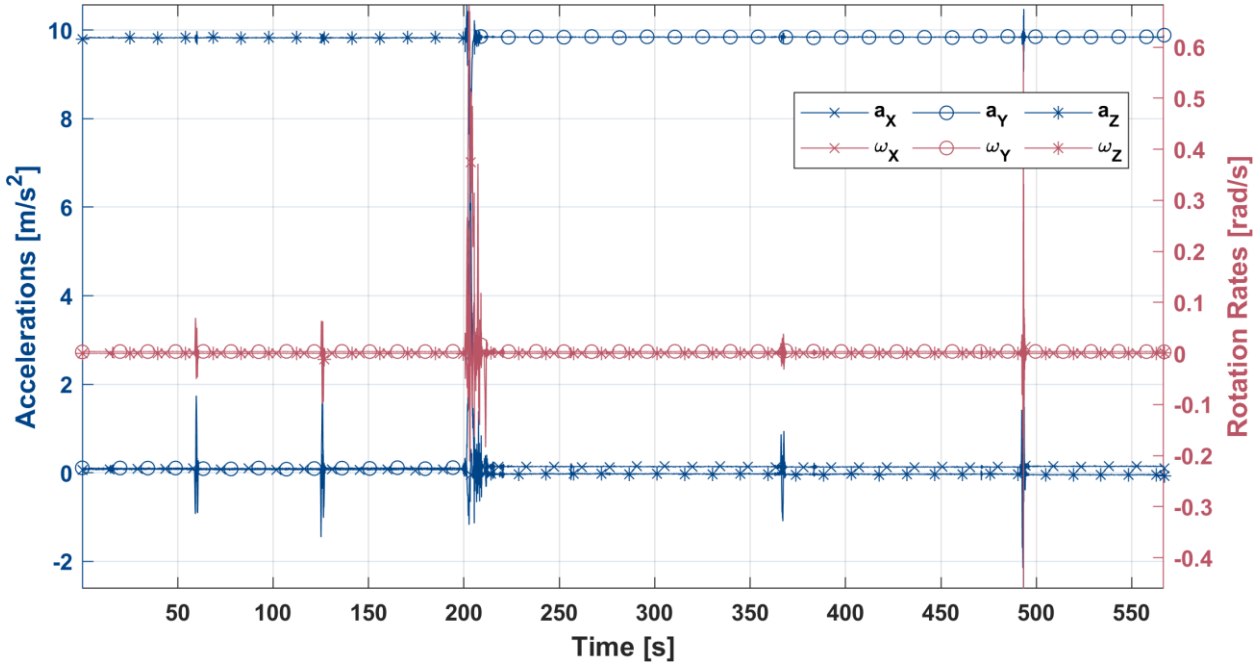
Accelerations [m/s^2]
Rotation Rates [rad/s]
Time [s]
a_X a_Y a_Z
ω_X ω_Y ω_Z

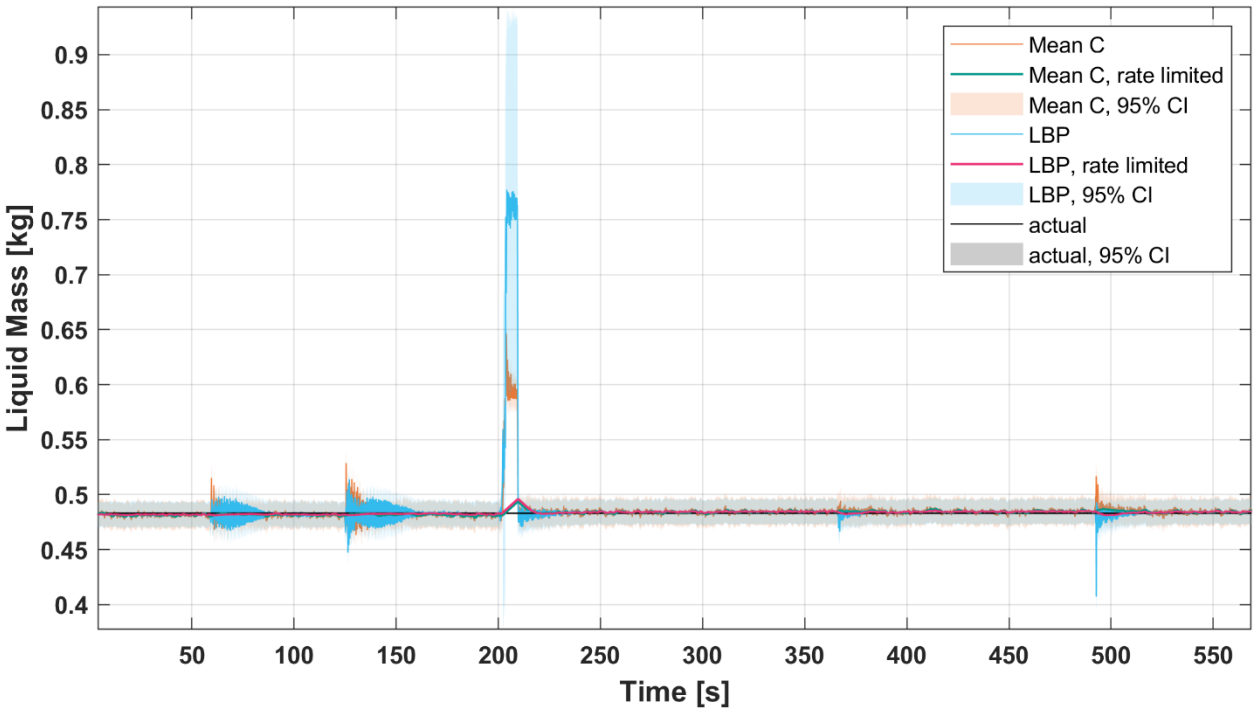
Liquid Mass [kg]
Time [s]
Mean C
Mean C, rate limited
Mean C, 95% CI
LBP
LBP, rate limited
LBP, 95% CI
actual
actual, 95% CI

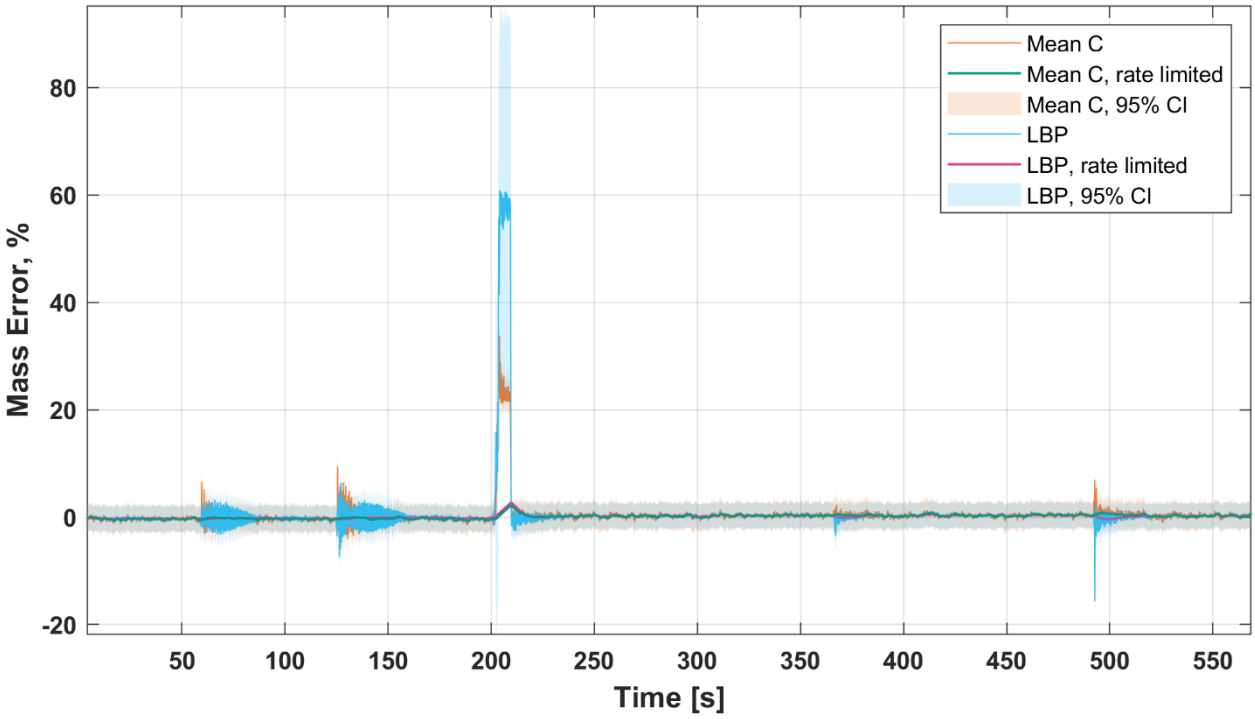
Mean C
Mean C, rate limited
Mean C, 95% CI
LBP
LBP, rate limited
LBP, 95% CI
Mass Error, %
80
60
40
20
0
-20
50
100
150
200
250
300
350
400
450
500
550
Time [s]

20% NVF

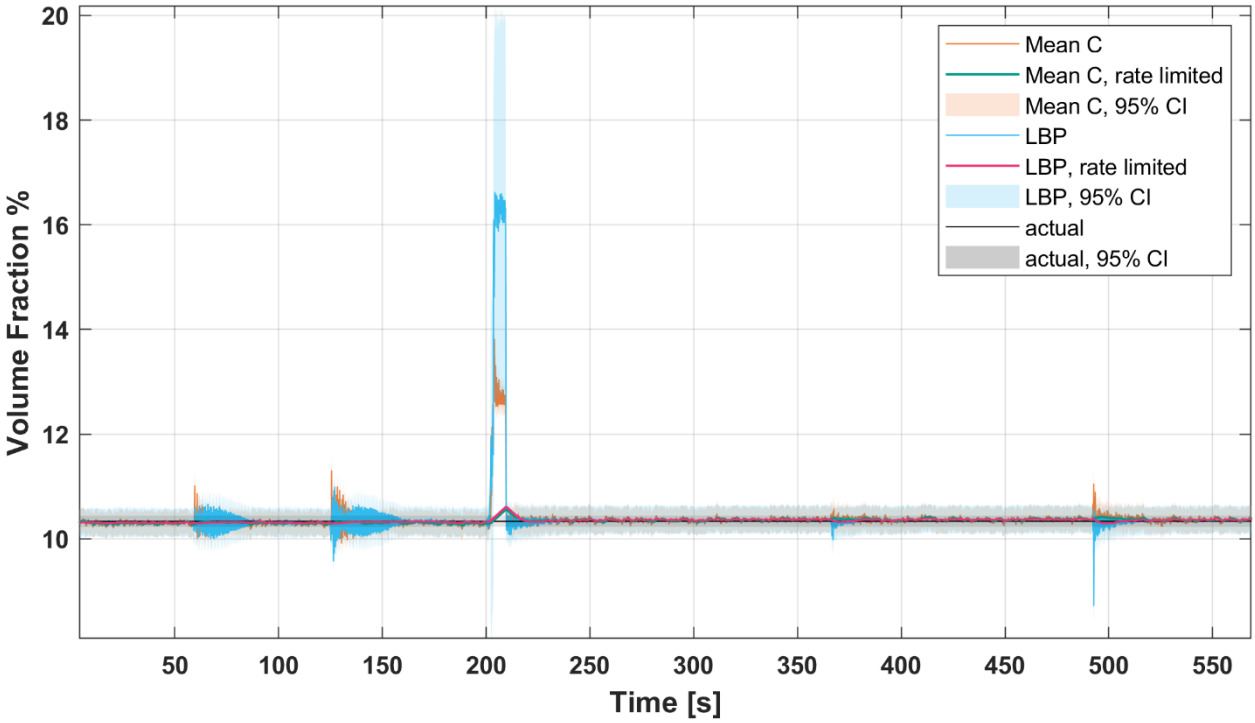
Mean C
Mean C, rate limited
Mean C, 95% CI
LBP
LBP, rate limited
LBP, 95% CI
actual
actual, 95% CI
Volume Fraction %
20
18
16
14
12
10
50
100
150
200
250
300
350
400
450
500
550
Time [s]

20% NVF Horizontal Only (data during rotation from horizontal to vertical was lost)

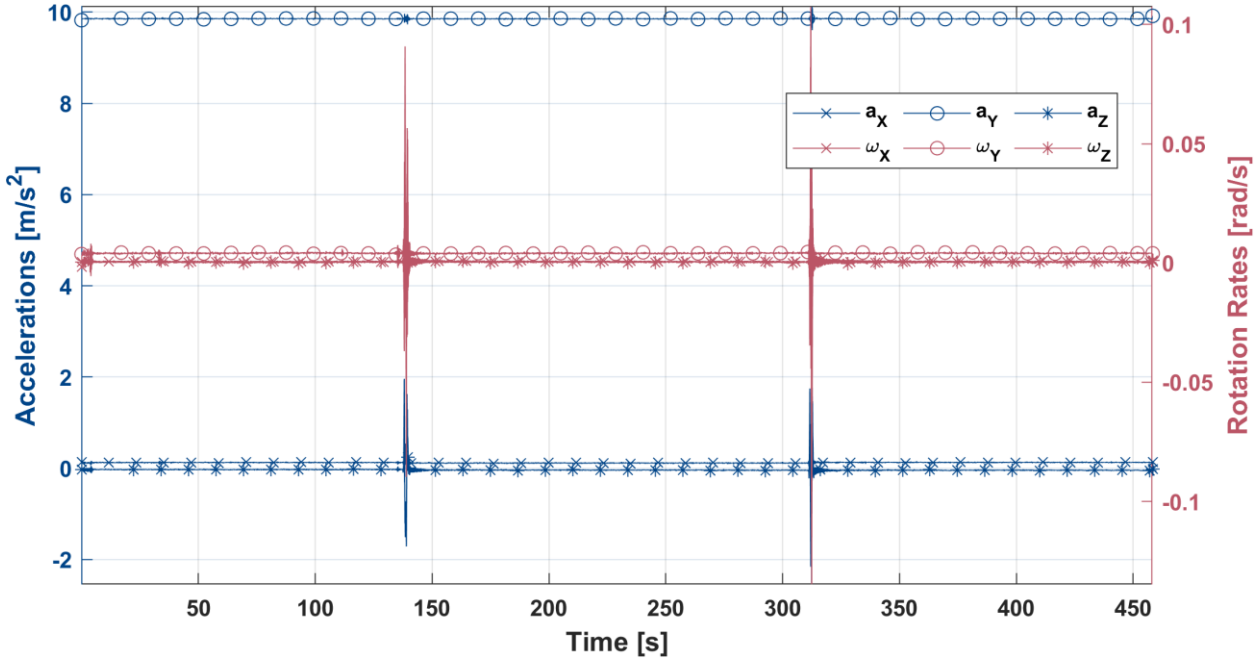

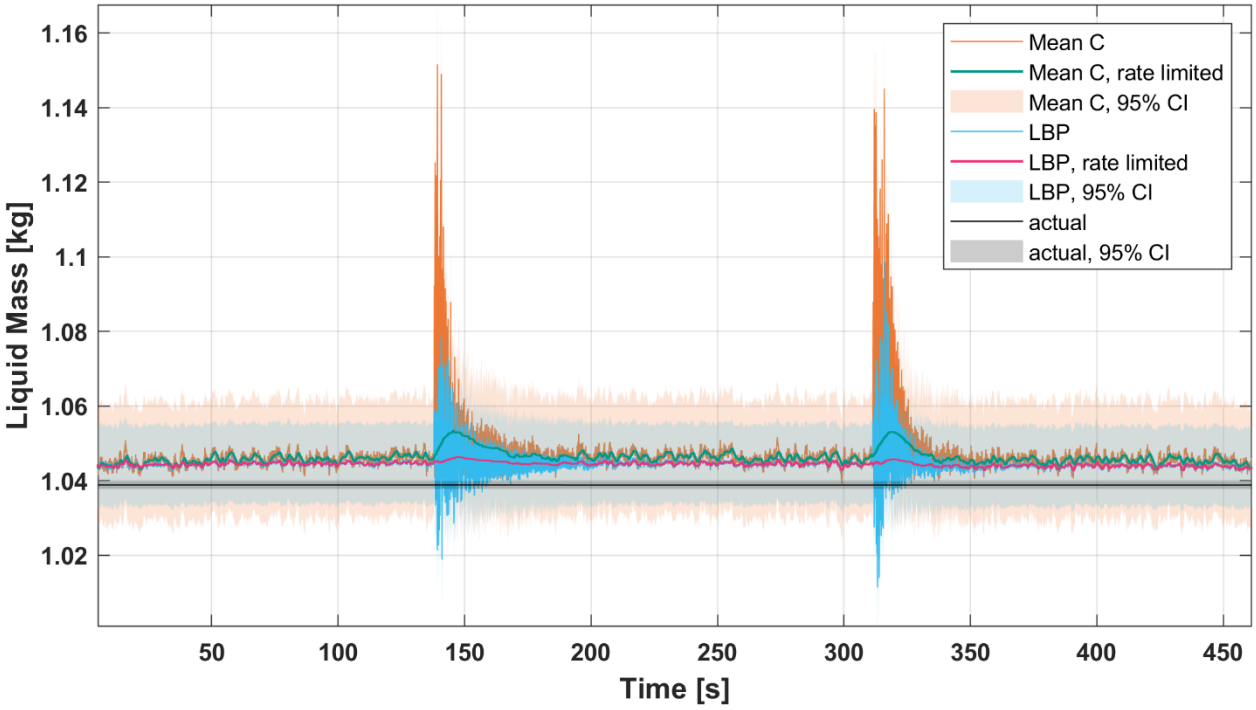

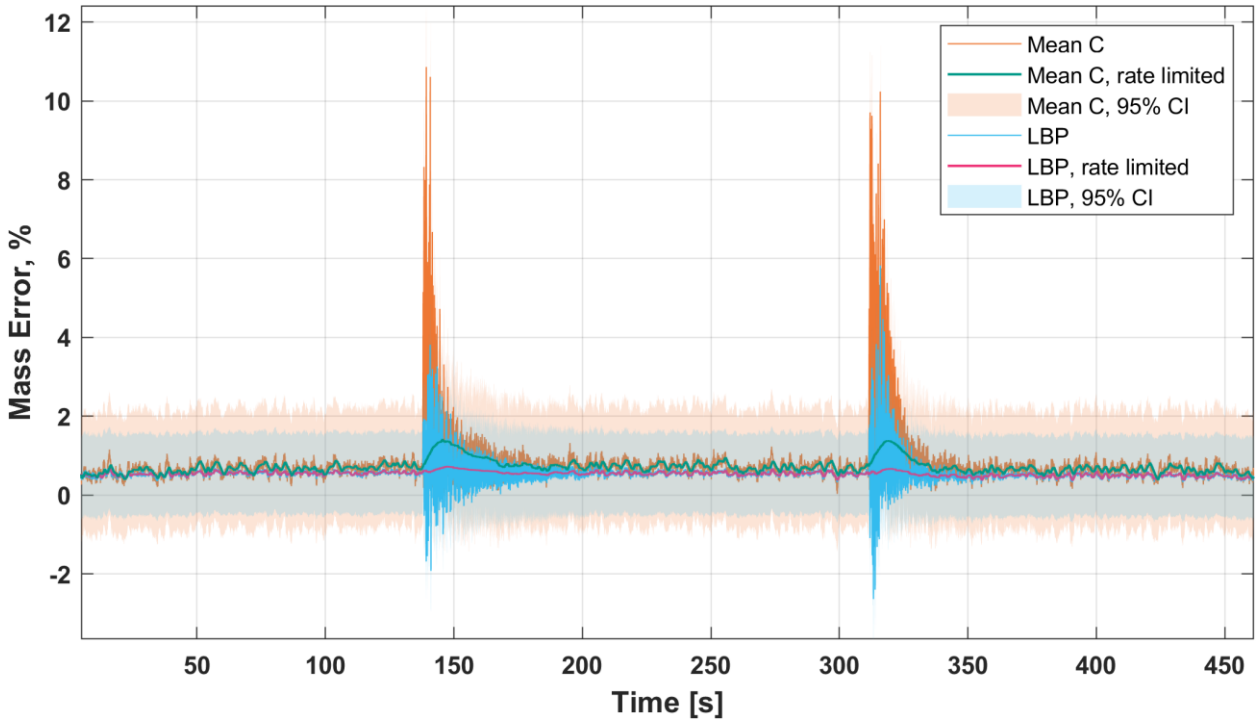
Mean C
Mean C, rate limited
Mean C, 95% CI
LBP
LBP, rate limited
LBP, 95% CI
Mass Error, %
Time [s]

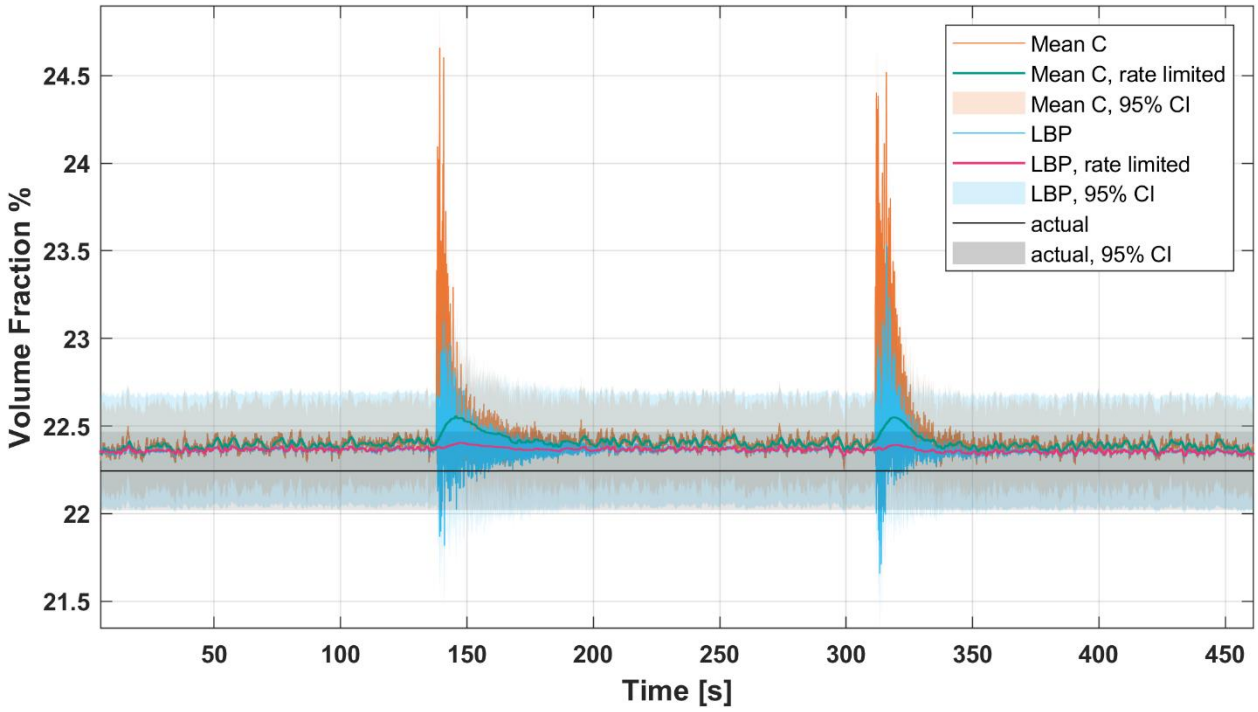
Mean C
Mean C, rate limited
Mean C, 95% CI
LBP
LBP, rate limited
LBP, 95% CI
actual
actual, 95% CI
Volume Fraction %
Time [s]

20% NVF Vertical Only

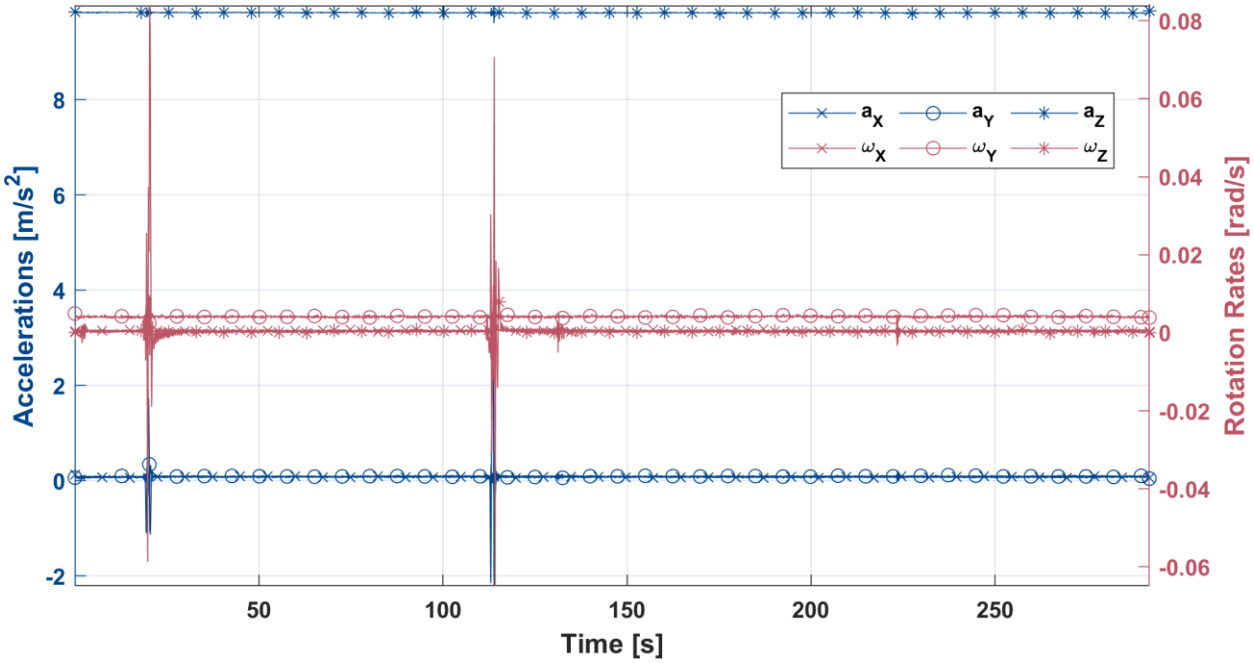

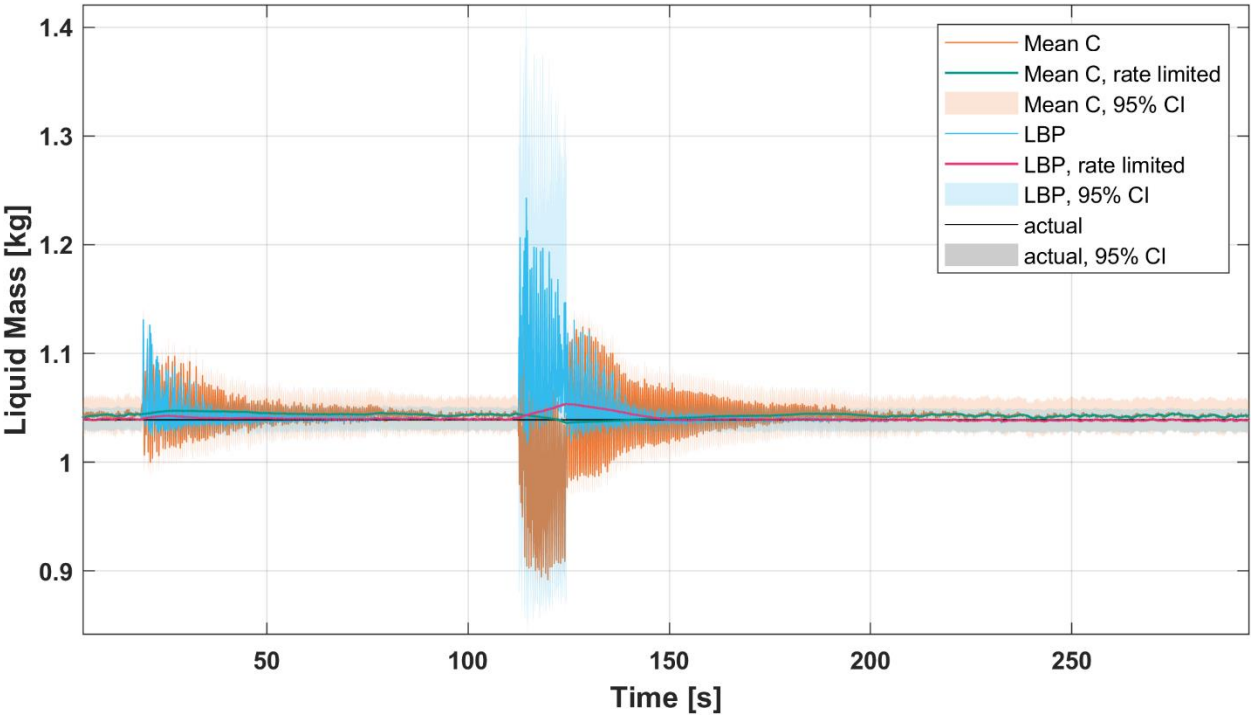

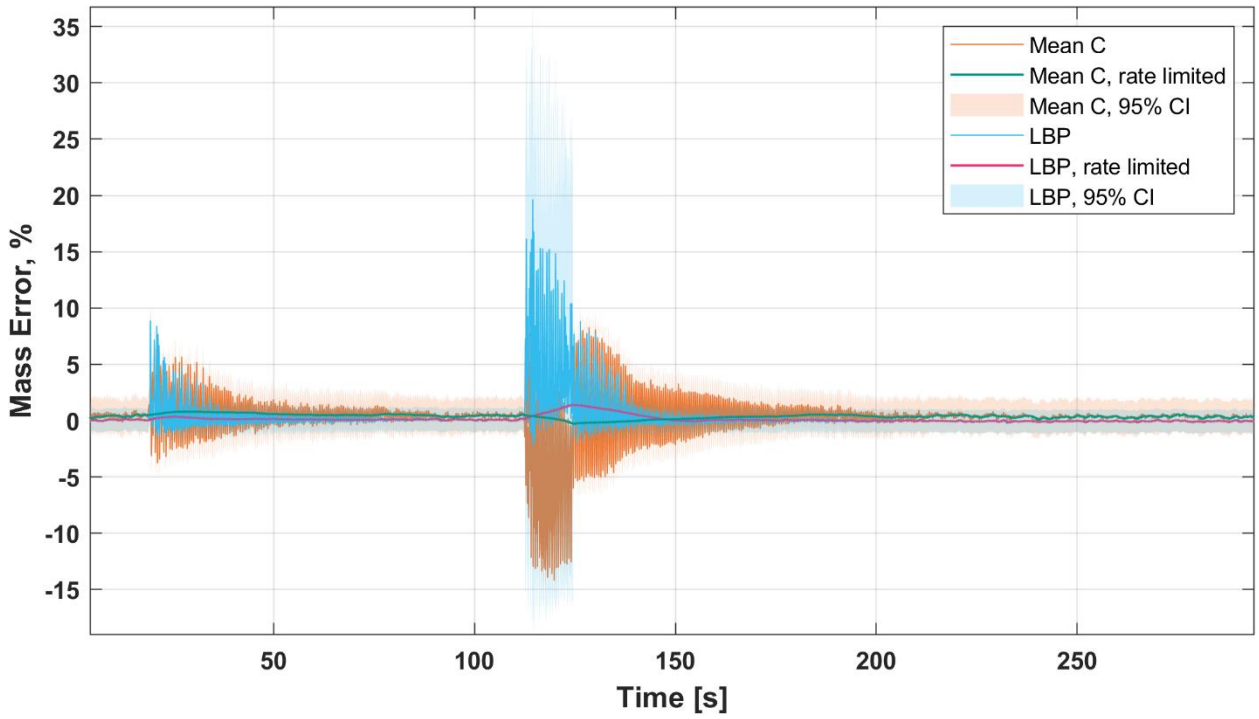
Mean C
Mean C, rate limited
Mean C, 95% CI
LBP
LBP, rate limited
LBP, 95% CI
Mass Error, %
35
30
25
20
15
10
5
0
-5
-10
-15
50
100
150
200
250
Time [s]

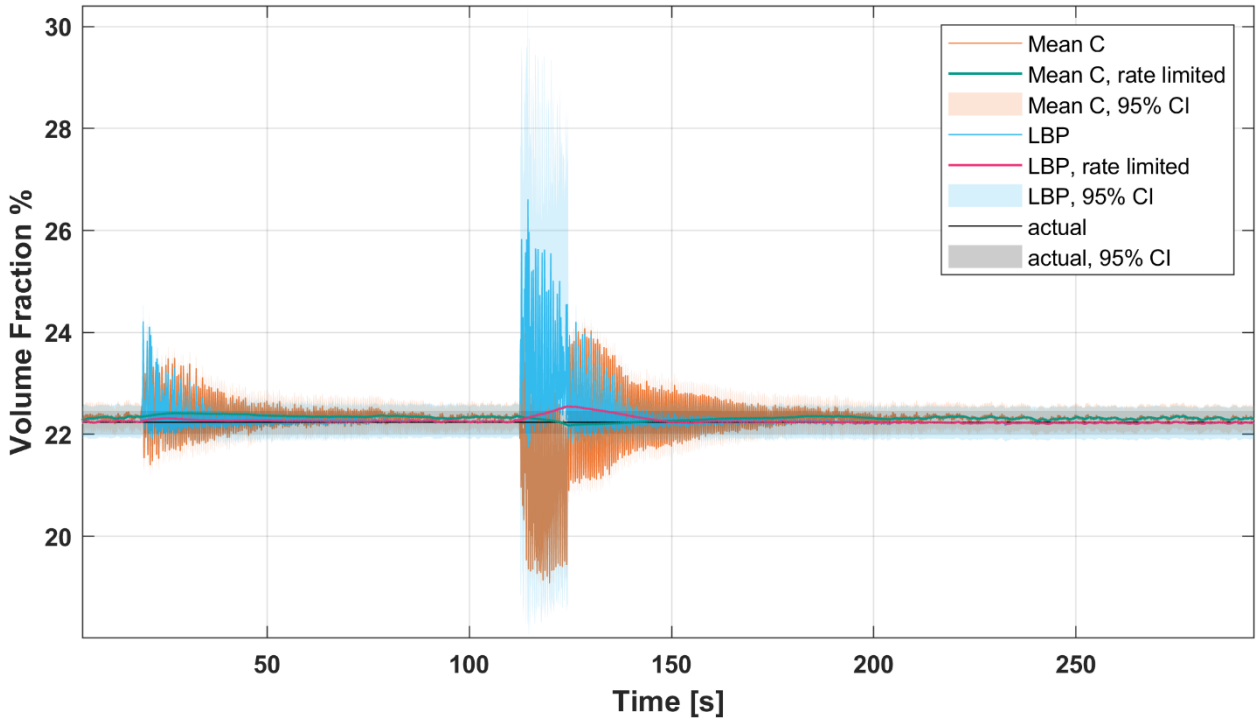
Mean C
Mean C, rate limited
Mean C, 95% CI
LBP
LBP, rate limited
LBP, 95% CI
actual
actual, 95% CI
Volume Fraction %
30
28
26
24
22
20
50
100
150
200
250
Time [s]

30% NVF (mass and mass error plots shown in body text)

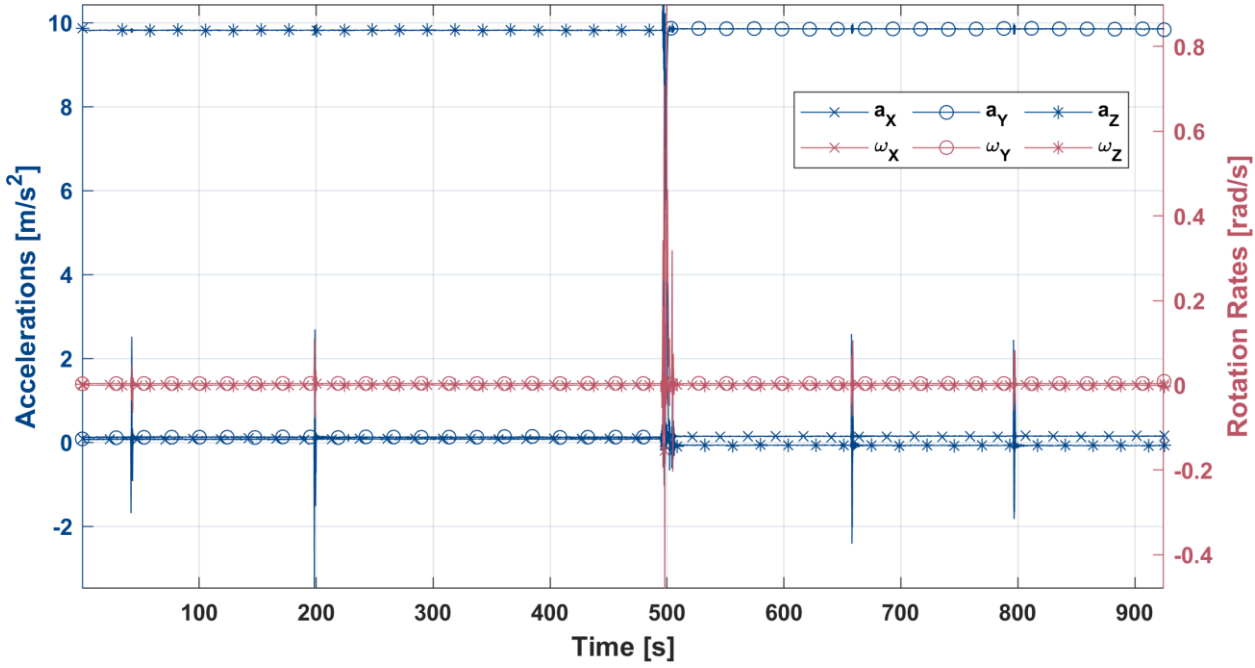

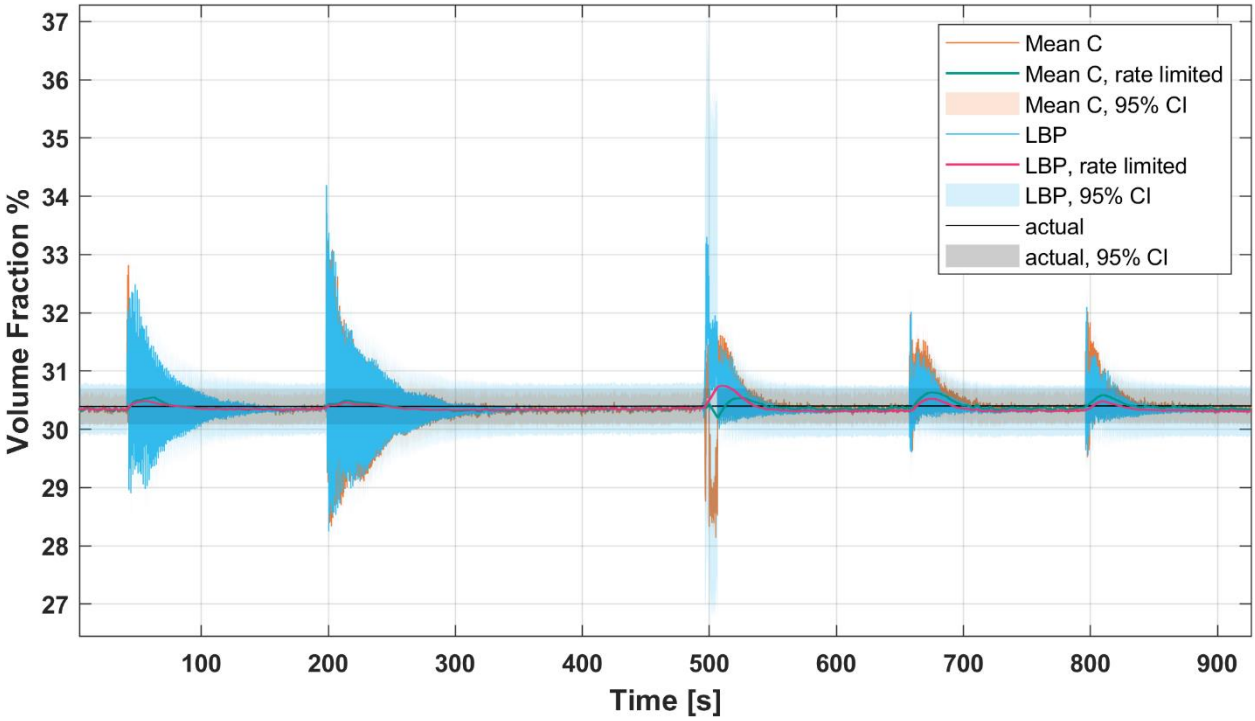

40% NVF

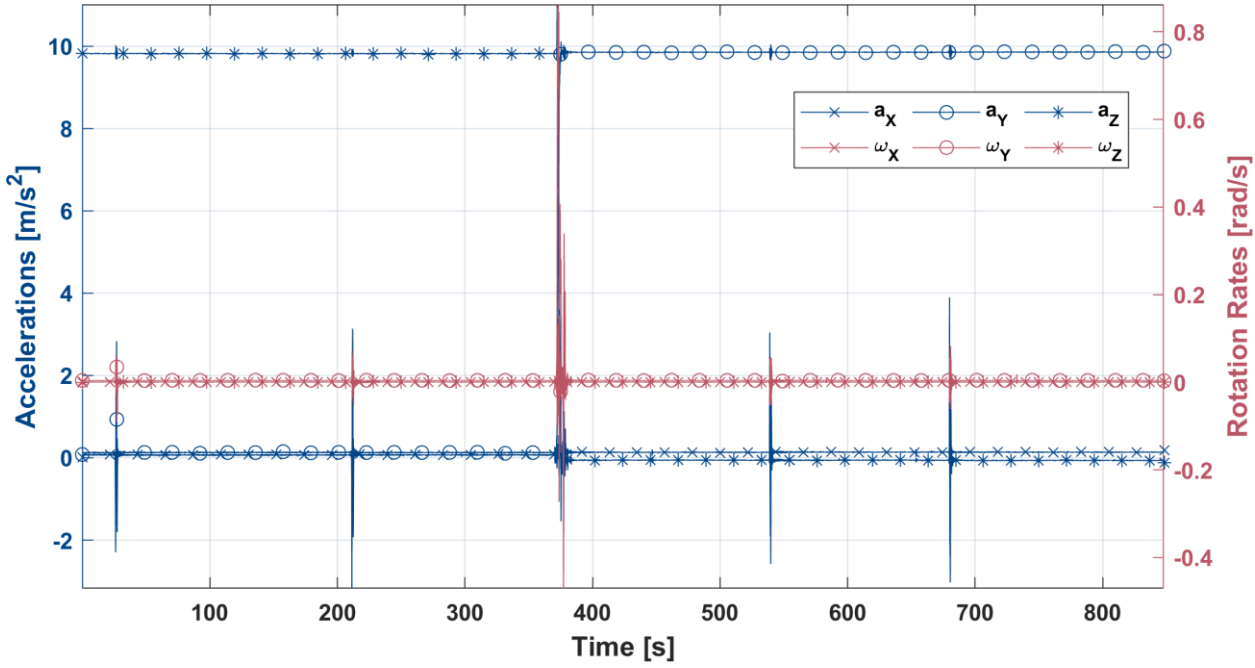
Accelerations [m/s^2]
Rotation Rates [rad/s]
Time [s]
a_X a_Y a_Z
ω_X ω_Y ω_Z

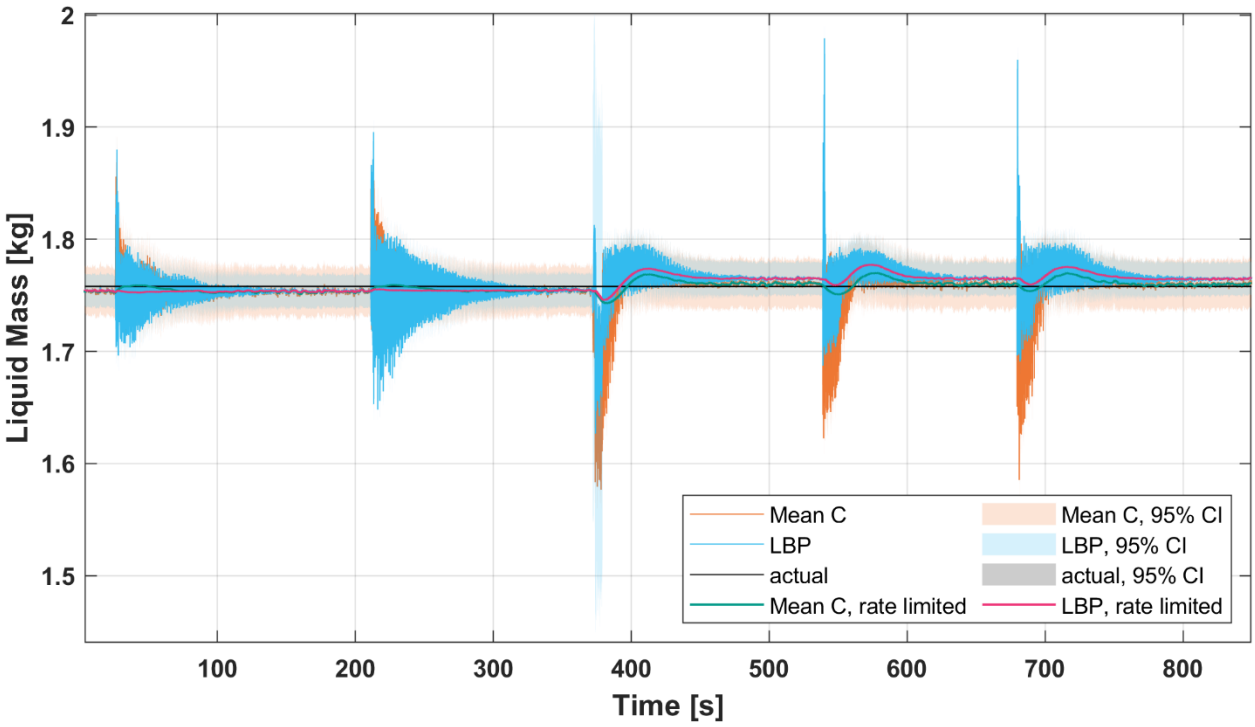
Liquid Mass [kg]
Time [s]
Mean C
LBP
actual
Mean C, rate limited
Mean C, 95% CI
LBP, 95% CI
actual, 95% CI
LBP, rate limited

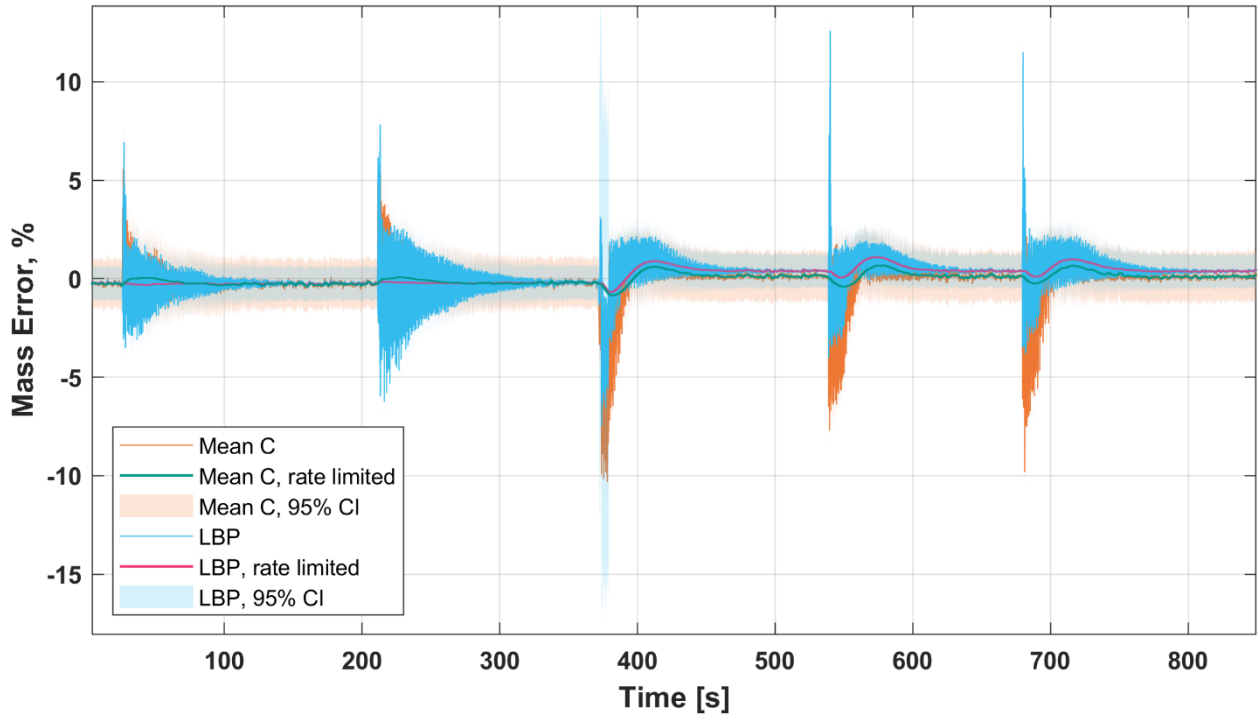
Mass Error, %
10
5
0
-5
-10
-15
100
200
300
400
500
600
700
800
Time [s]
Mean C
Mean C, rate limited
Mean C, 95% CI
LBP
LBP, rate limited
LBP, 95% CI

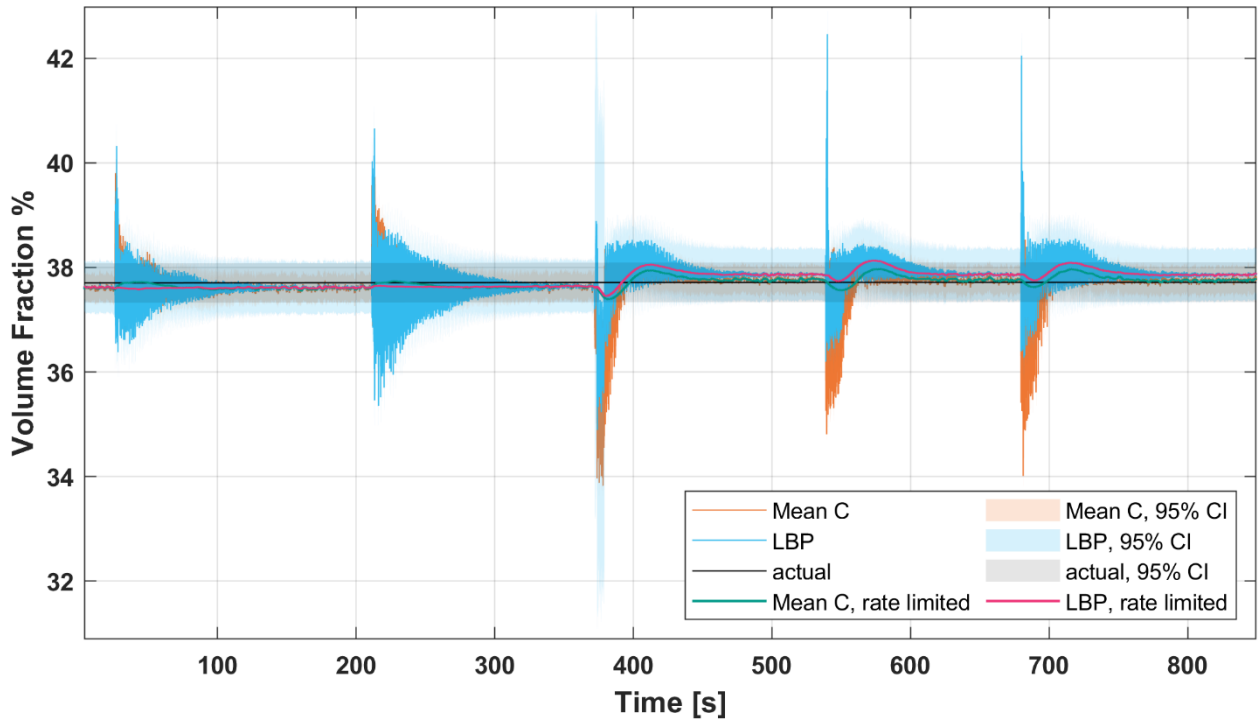
Volume Fraction %
42
40
38
36
34
32
100
200
300
400
500
600
700
800
Time [s]
Mean C
LBP
actual
Mean C, rate limited
Mean C, 95% CI
LBP, 95% CI
actual, 95% CI
LBP, rate limited

50% NVF (IMU, mass, and mass error plots are in body text)

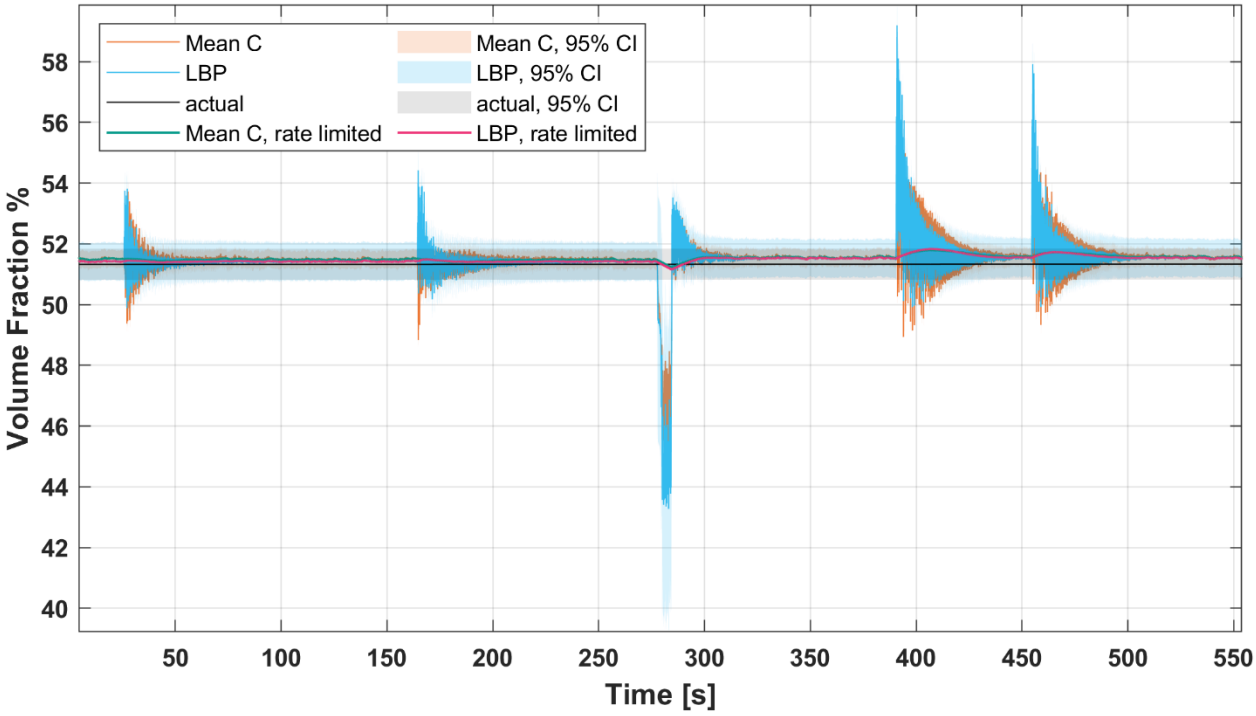

60% NVF

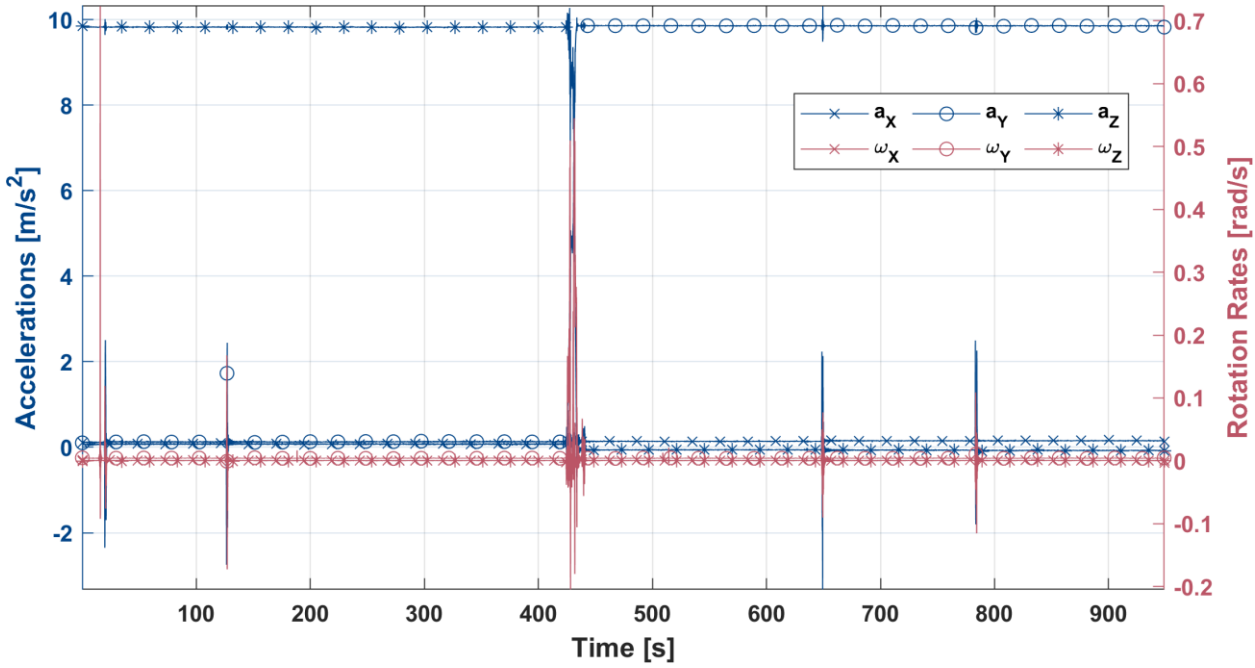

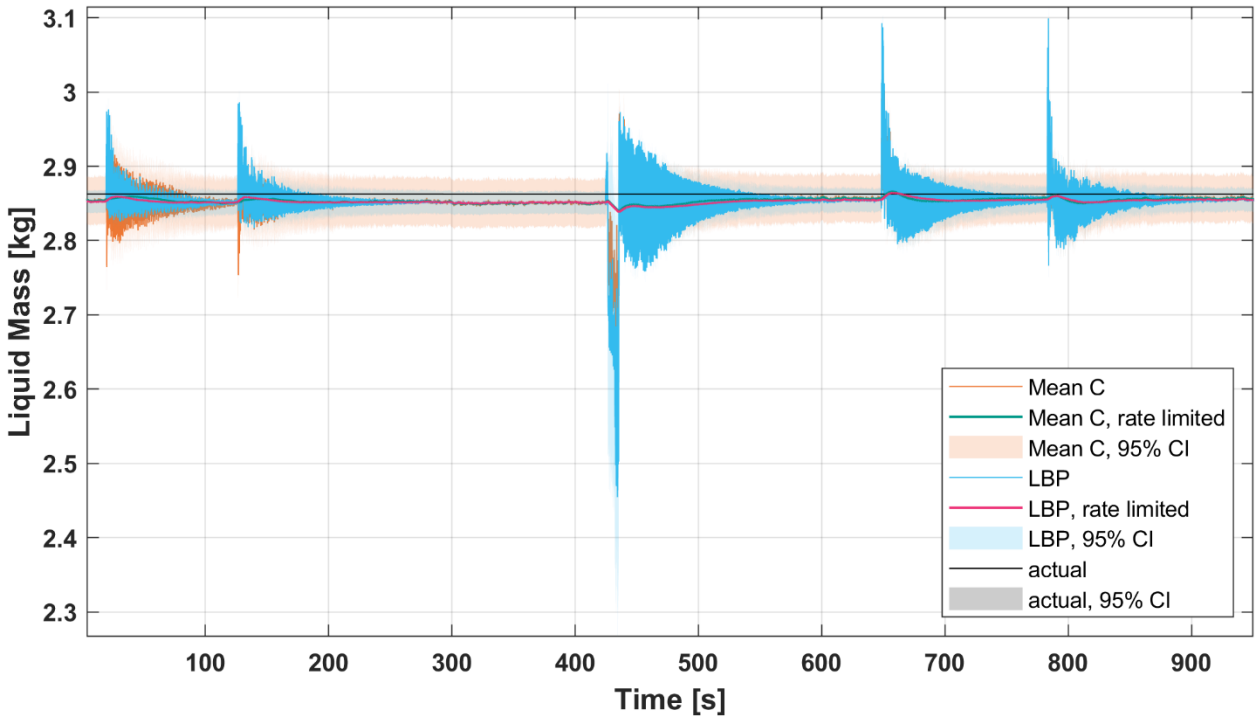
Liquid Mass [kg]
3.1
3
2.9
2.8
2.7
2.6
2.5
2.4
2.3
100
200
300
400
500
600
700
800
900
Time [s]
Mean C
Mean C, rate limited
Mean C, 95% CI
LBP
LBP, rate limited
LBP, 95% CI
actual
actual, 95% CI

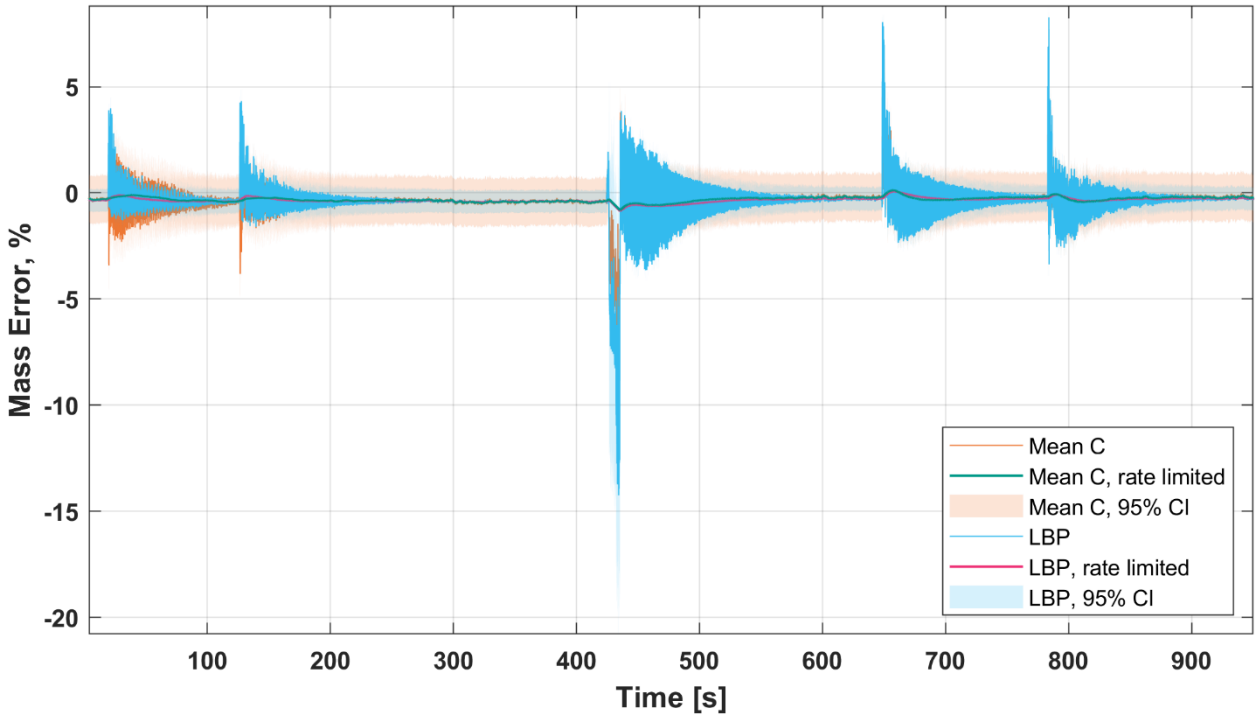
Mass Error, %
5
0
-5
-10
-15
-20
100
200
300
400
500
600
700
800
900
Time [s]
Mean C
Mean C, rate limited
Mean C, 95% CI
LBP
LBP, rate limited
LBP, 95% CI

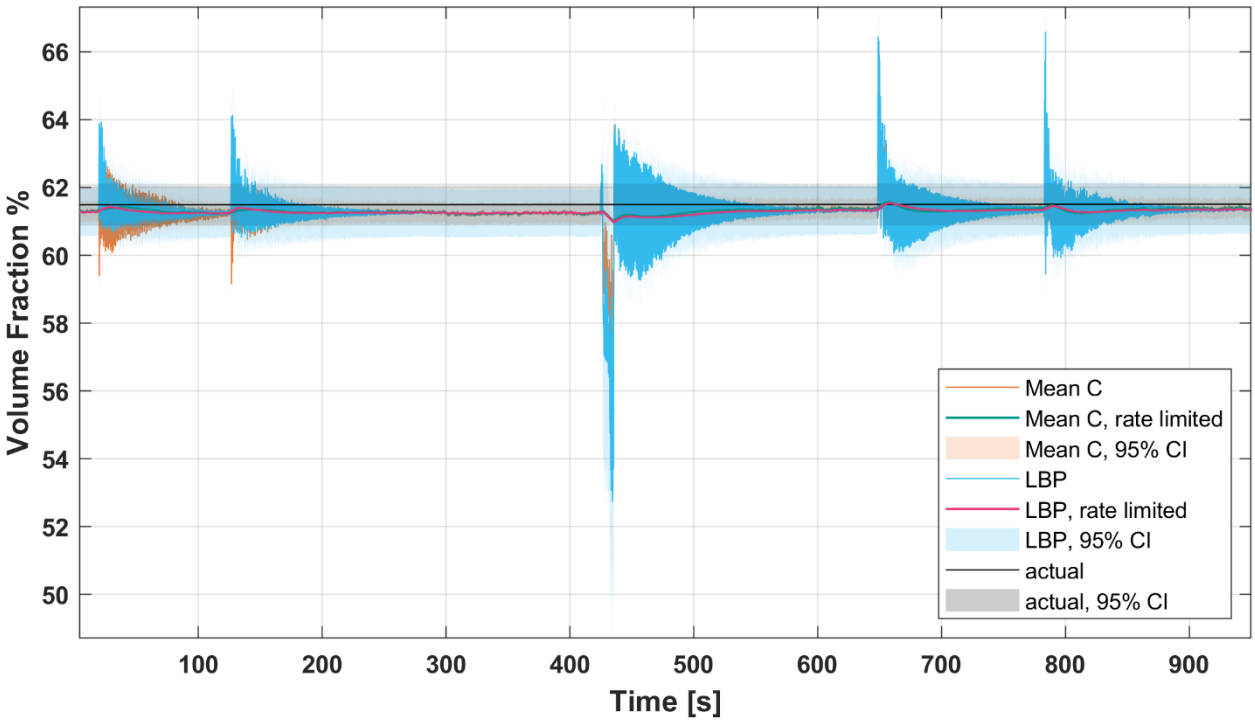
Volume Fraction %
66
64
62
60
58
56
54
52
50
100
200
300
400
500
600
700
800
900
Time [s]
Mean C
Mean C, rate limited
Mean C, 95% CI
LBP
LBP, rate limited
LBP, 95% CI
actual
actual, 95% CI

70% NVF (mass and mass error plots shown in body text)

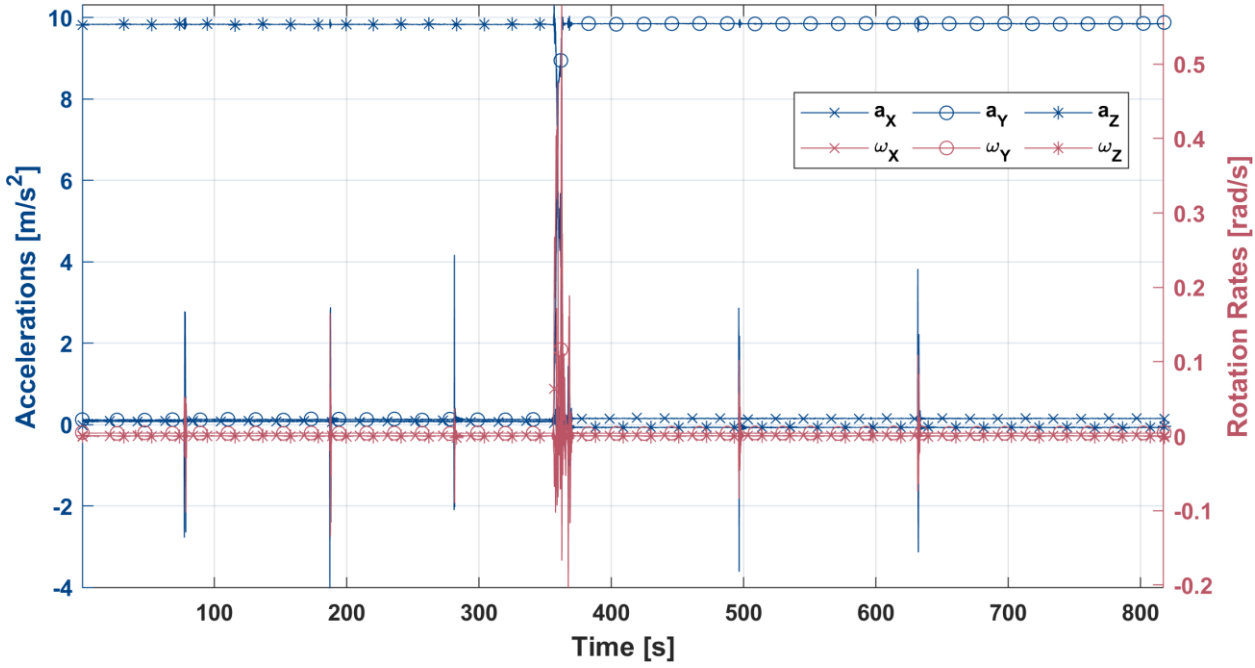

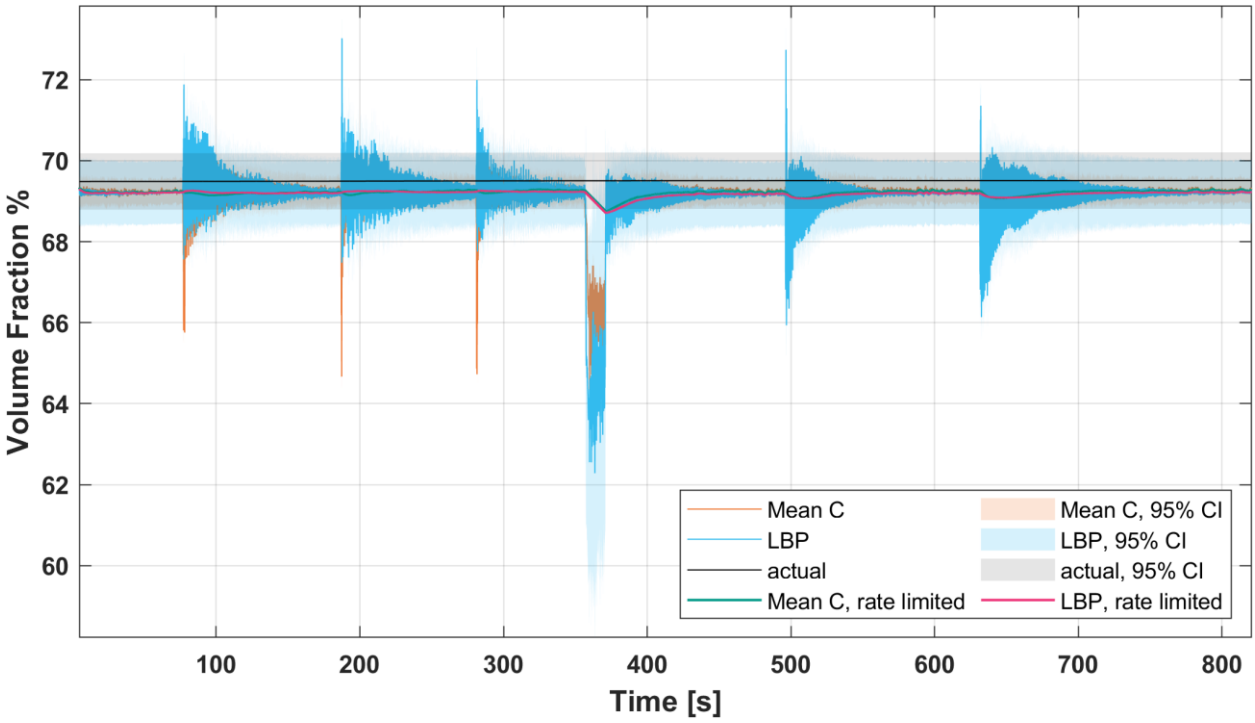

80% NVF

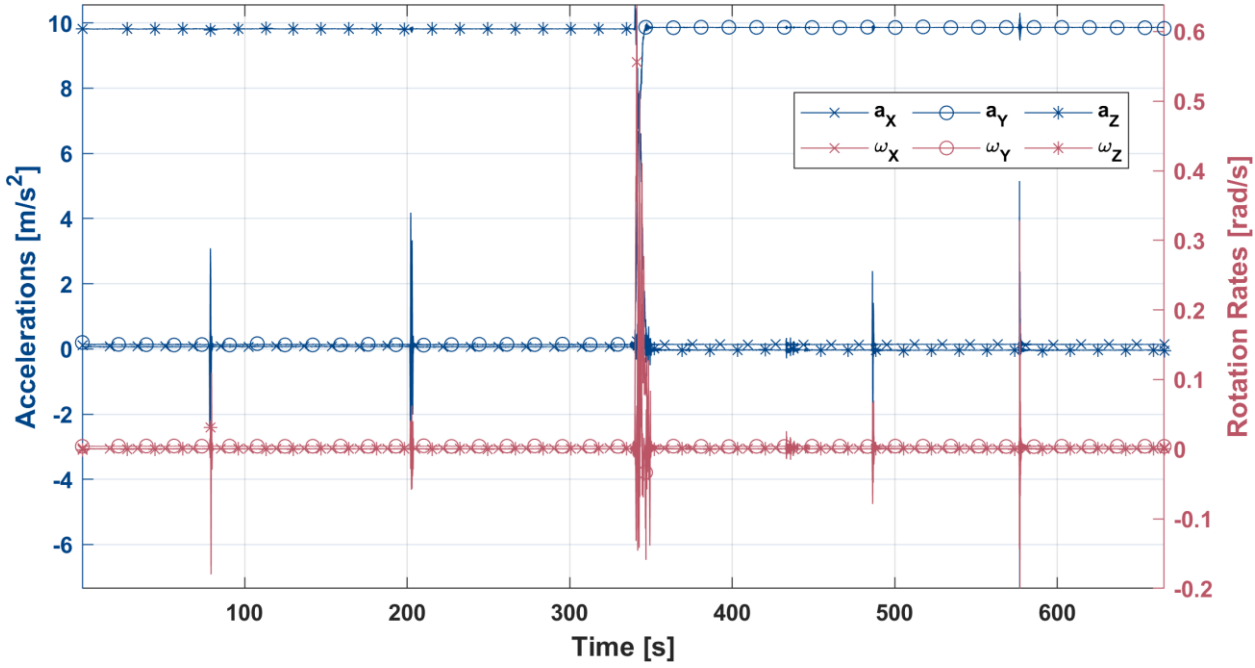
Accelerations [m/s^2]
Rotation Rates [rad/s]
Time [s]
a_X
a_Y
a_Z
ω_X
ω_Y
ω_Z

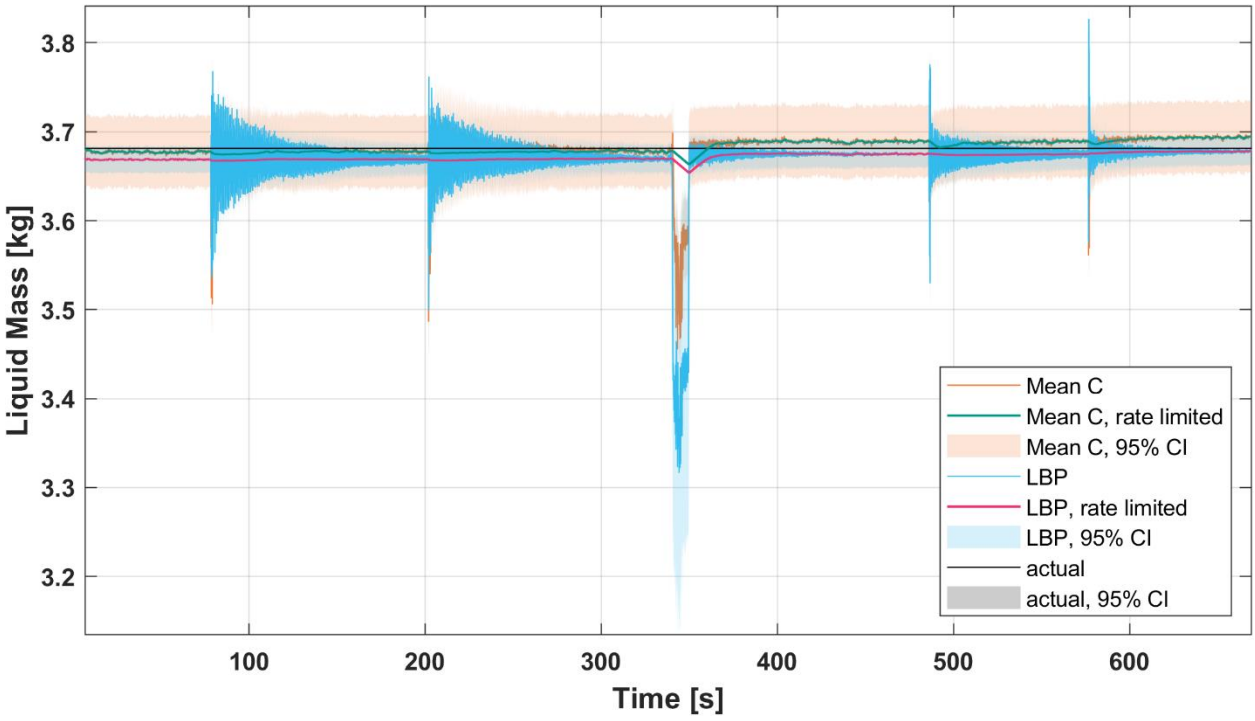
Liquid Mass [kg]
Time [s]
Mean C
Mean C, rate limited
Mean C, 95% CI
LBP
LBP, rate limited
LBP, 95% CI
actual
actual, 95% CI

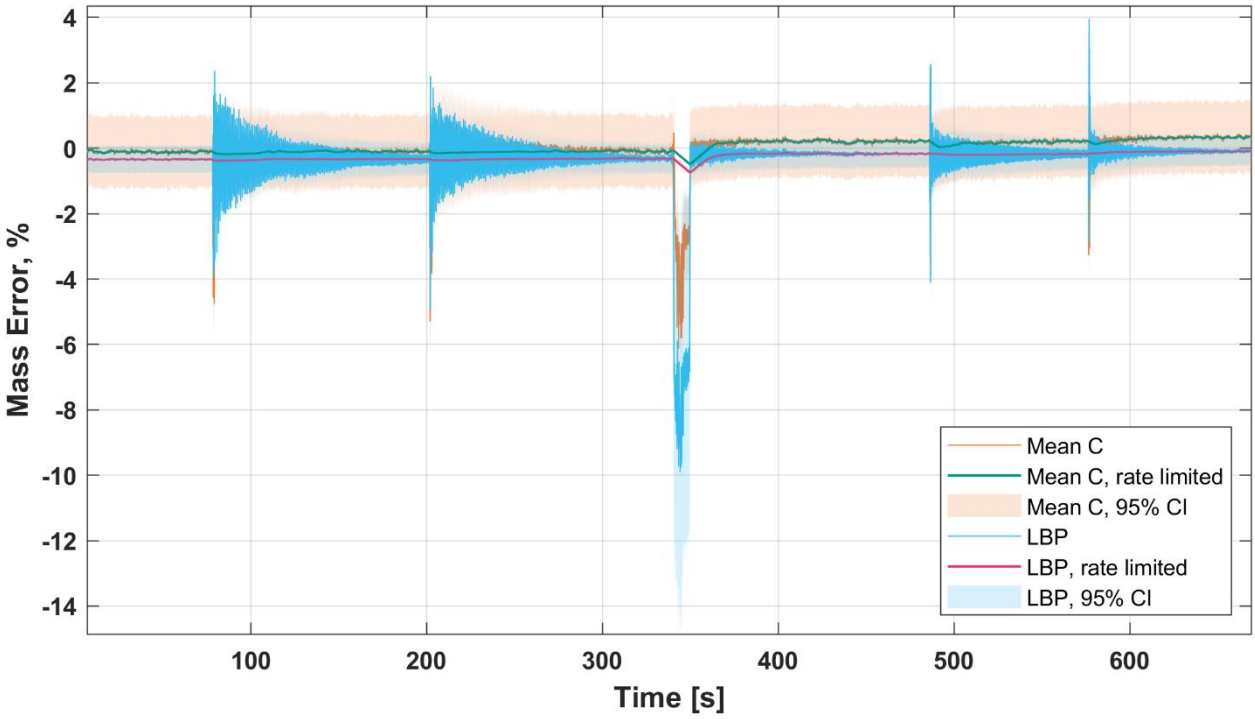
Mass Error, %
4
2
0
-2
-4
-6
-8
-10
-12
-14
100
200
300
400
500
600
Time [s]
Mean C
Mean C, rate limited
Mean C, 95% CI
LBP
LBP, rate limited
LBP, 95% CI

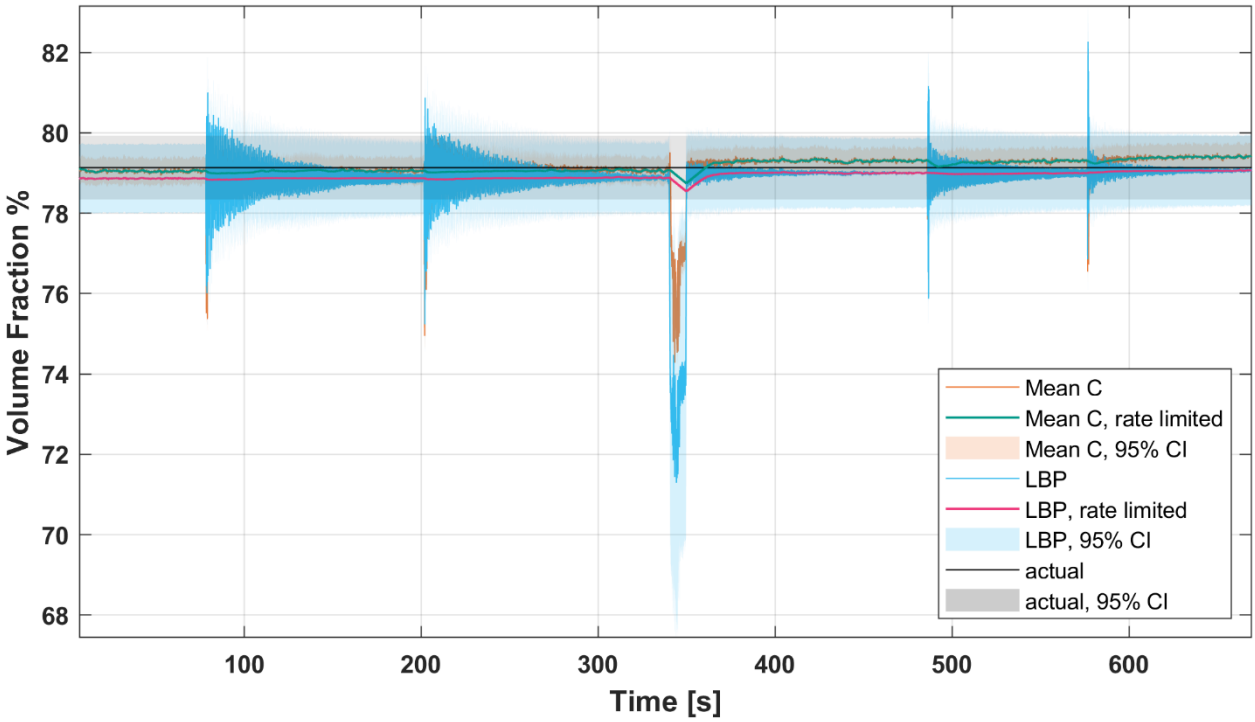
Volume Fraction %
82
80
78
76
74
72
70
68
100
200
300
400
500
600
Time [s]
Mean C
Mean C, rate limited
Mean C, 95% CI
LBP
LBP, rate limited
LBP, 95% CI
actual
actual, 95% CI

90% NVF

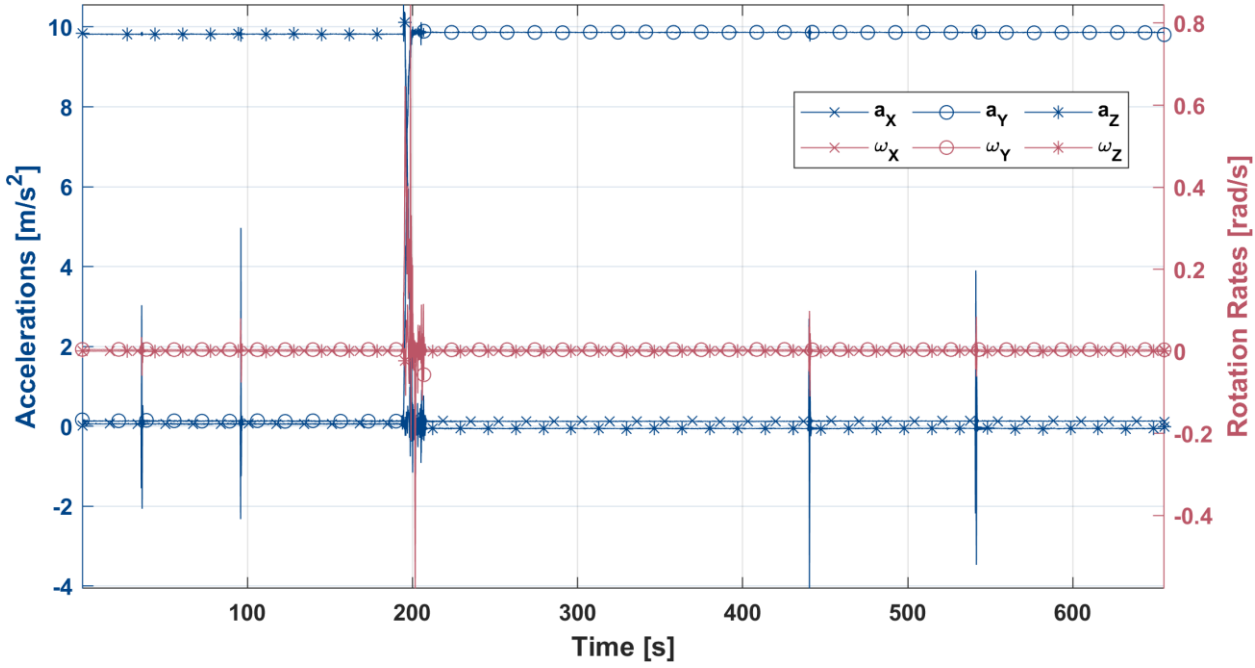
Accelerations [m/s^2]
Rotation Rates [rad/s]
Time [s]
a_X a_Y a_Z
ω_X ω_Y ω_Z

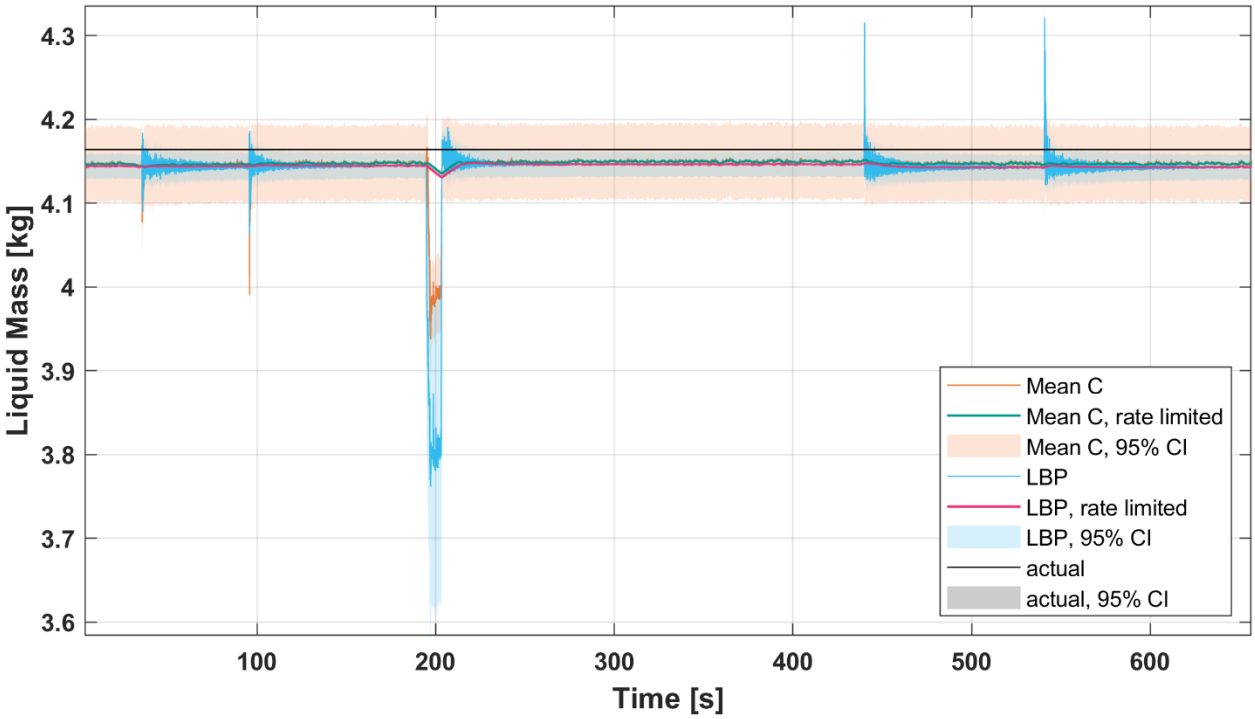
Liquid Mass [kg]
Time [s]
Mean C
Mean C, rate limited
Mean C, 95% CI
LBP
LBP, rate limited
LBP, 95% CI
actual
actual, 95% CI

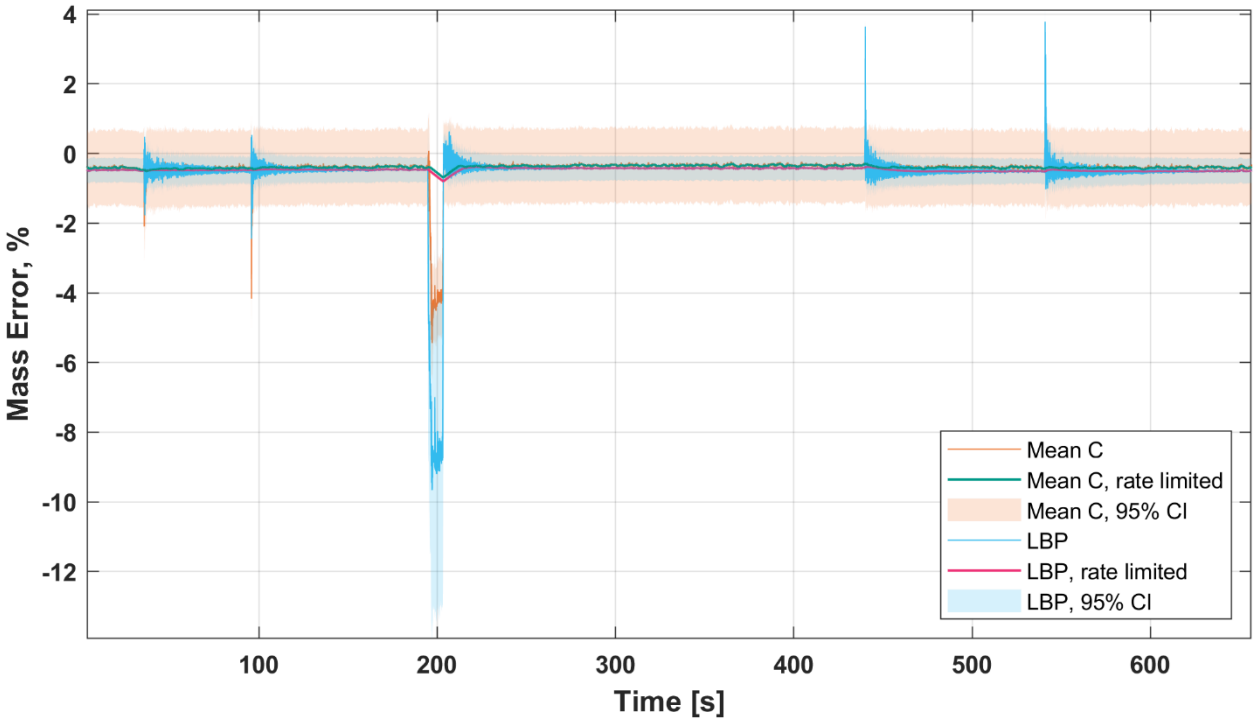
Mass Error, %
4
2
0
-2
-4
-6
-8
-10
-12
100
200
300
400
500
600
Time [s]
Mean C
Mean C, rate limited
Mean C, 95% CI
LBP
LBP, rate limited
LBP, 95% CI

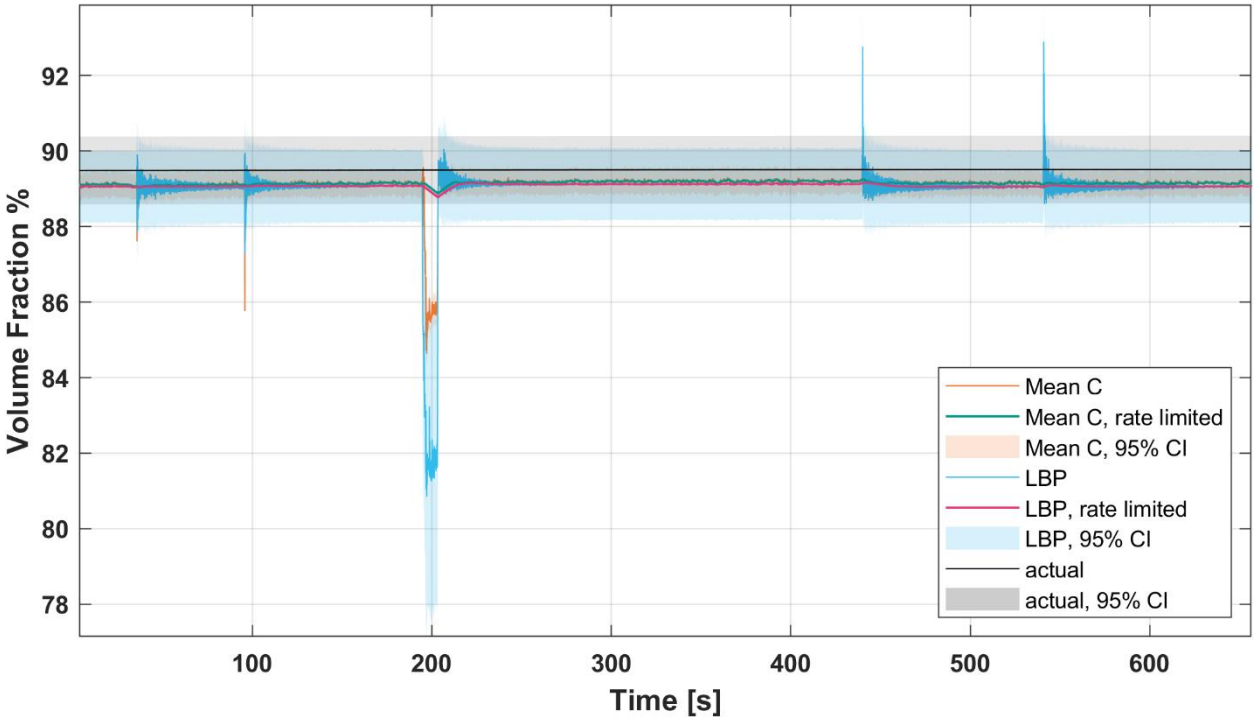
Volume Fraction %
92
90
88
86
84
82
80
78
100
200
300
400
500
600
Time [s]
Mean C
Mean C, rate limited
Mean C, 95% CI
LBP
LBP, rate limited
LBP, 95% CI
actual
actual, 95% CI

Appendix B Additional Flight Test Plots

5% NVF

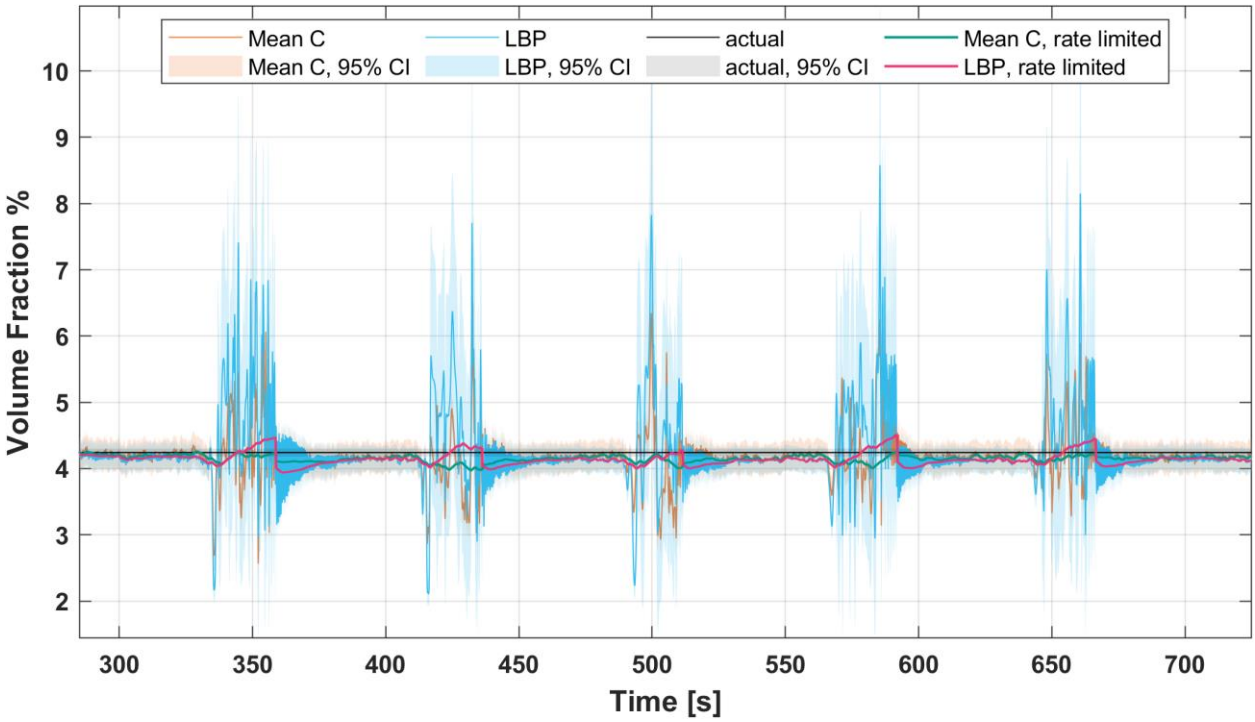

20% NVF

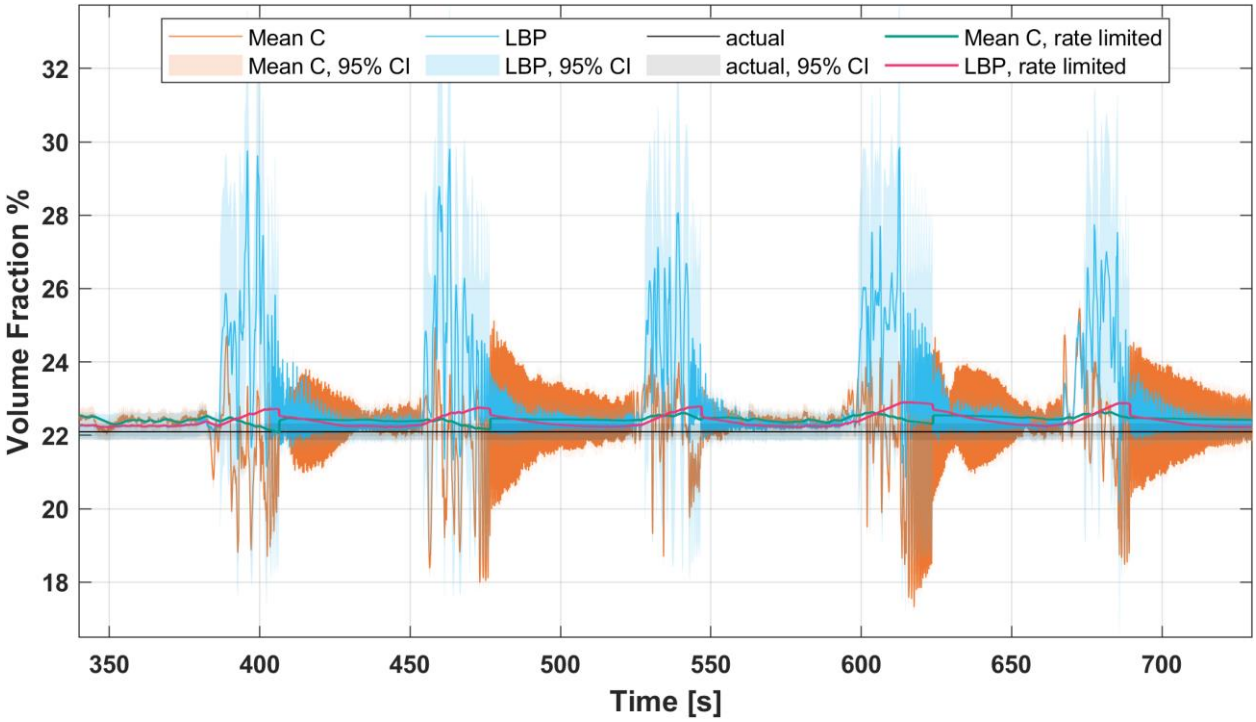

50% NVF

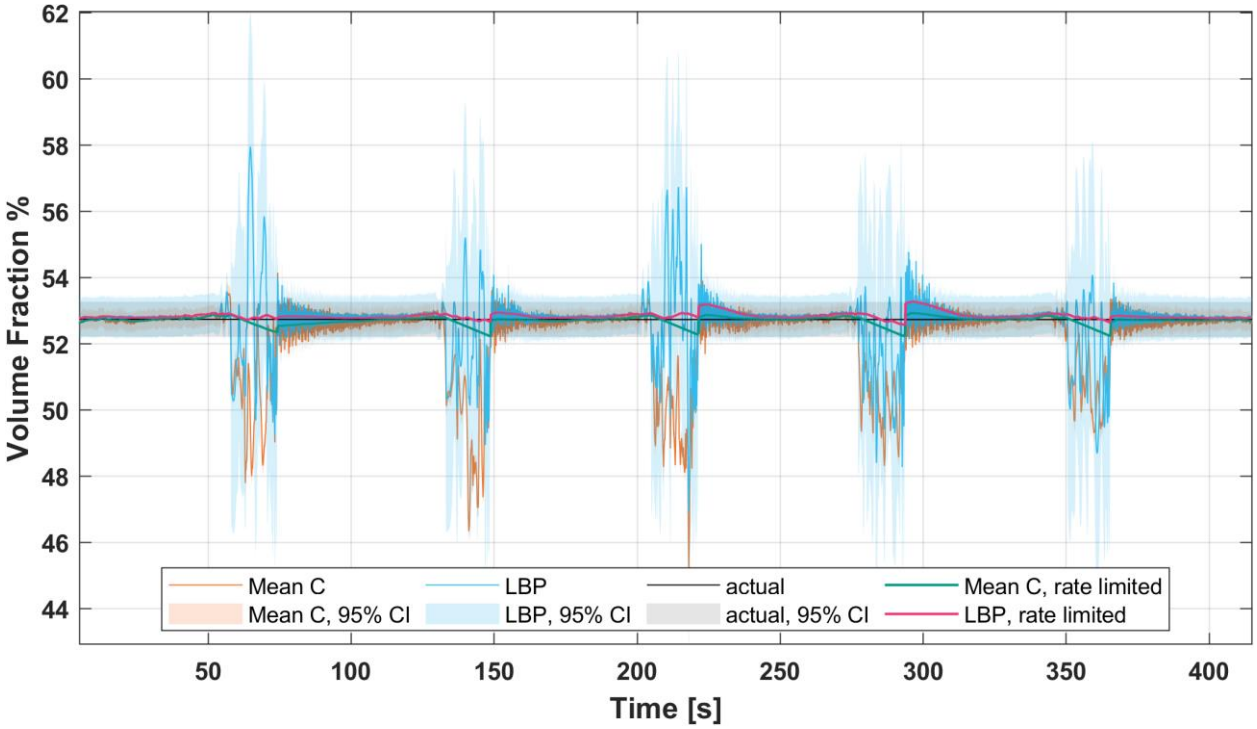
Volume Fraction %
Time [s]
Mean C
Mean C, 95% CI
LBP
LBP, 95% CI
actual
actual, 95% CI
Mean C, rate limited
LBP, rate limited

80% NVF

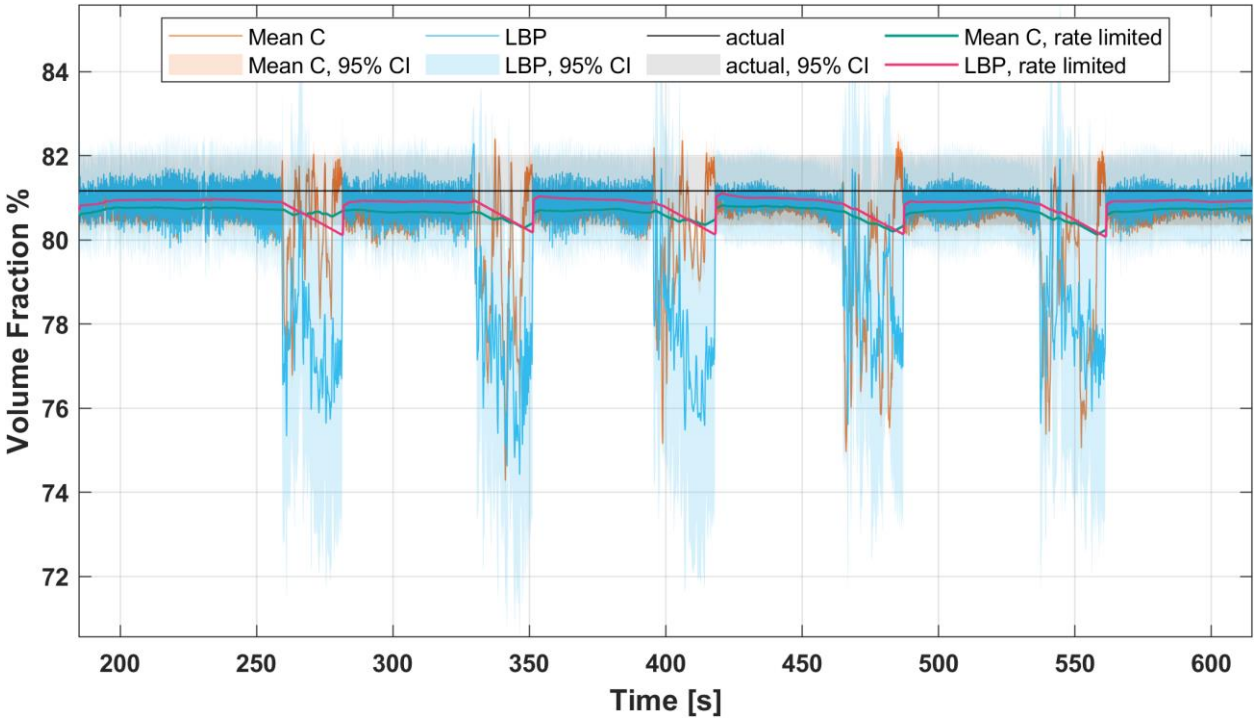
Volume Fraction %
Time [s]
Mean C
Mean C, 95% CI
LBP
LBP, 95% CI
actual
actual, 95% CI
Mean C, rate limited
LBP, rate limited